Electronic Thesis and Dissertation Repository

9-22-2015 12:00 AM

Charging Level and Deposition of Droplets in Electrostatic Painting

Husam Osman, *The University of Western Ontario*

Supervisor: Dr. Kazimierz Adamiak, *The University of Western Ontario*
Joint Supervisor: Dr. G.S. Peter Castle, *The University of Western Ontario*
A thesis submitted in partial fulfillment of the requirements for the Doctor of Philosophy degree in Electrical and Computer Engineering
© Husam Osman 2015

Recommended Citation

CHARGING LEVEL AND DEPOSITION OF DROPLETS IN ELECTROSTATIC
PAINTING

(Thesis format: Integrated-Article)

by

Husam <u>Osman</u>

Graduate Program in Electrical and Computer Engineering

A thesis submitted in partial fulfillment
of the requirements for the degree of
Doctor of Philosophy

The School of Graduate and Postdoctoral Studies
Western University
London, Ontario, Canada

© Husam Osman 2015

Abstract

The process of electrostatic painting has become a very important method of coating in a wide range of industrial applications including those used in the automobile industry. The general principle of spray coating is to deposit liquid droplets or solid powder particles on coated targets having various shapes. The electrostatic coating process consists of three main stages: droplet formation and charging, transportation and deposition. The complication of this process is caused by various factors, such as the physical properties of the material to be used, the appropriate electrical and mechanical conditions and the target surface to be coated, which affects significantly the deposition uniformity and the finish quality, especially when it contains some sharp edges and recessed areas.

In this thesis, a numerical investigation of the charging level on a spherical droplet formed out of a cylindrical ligament in an external uniform electric field is presented. The droplet charge on a single ligament was predicted for different droplet sizes, ligament lengths, ligament diameters and electrode widths. The effect of these model parameters on the charge levels was found to be significant. A mathematical approximation for the charge magnitude as a function of the droplet radius to some exponent and ligament length is also formulated. The value of the radius exponent decreases dramatically with increasing the ligament length. Also, the estimated values of the droplet charge were compared for linear and circular arrays of ligaments, which show a great influence of the geometry of the sprayer on the charge levels. A very good agreement between the experimental and numerical results in the case of a circular array of ligaments, including a specified space charge, was obtained. All numerical simulations were performed using COMSOL, a Finite Element commercial software.

A further study is carried out to investigate the deposition thickness profile on a stationary and moving flat target by incorporating a numerical simulation of the industrial electrostatic coating process via ANSYS, a CFD commercial software. A modified injection pattern was suggested to achieve a closer agreement with the experimental data. The injection pattern includes 15 bands of different particle sizes (i.e. polydispersed particles) and charge to mass ratios. A combination of different injection angles and fractions of mass flow rates was suggested in each size band. A very good agreement between the experimental and numerical deposition patterns was obtained in both cases of a stationary and moving target.

Also, the deposition thickness profile was calculated on a target surface with a small perturbation at the center using ANSYS numerical model. Different model parameters of a perturbed surface, such as the size of the indentation or the protrusion and the radius of the corner were investigated in this study. The numerical results reveal a very low particle concentration inside the indentation, which is caused by the Faraday cage effect and it is strongly affected by the depth of the indentation, while the edge effect, which shows the high concentration of deposited particles at the corner, increases with decreasing the radius of curvature. The predicted deposition patterns were very consistent with the calculated values of the electric field for different surface perturbations.

Keywords

Co-Authorship Statement

This thesis has been written by Husam Osman under supervision of Dr. Kazimierz Adamiak and Dr. G.S. Peter Castle. Parts of the material presented in this thesis have been accepted for publication in several peer-reviewed journals and refereed conference proceedings as listed below. The research in each publication has been conducted by the principal author and guided/supported by or in collaboration with the underlined authors, who are the research supervisors or members of the advisory committee.

Chapter 4 presented a numerical investigation of the effect of the model parameters on the droplet charge levels, such as the ligament length and width, the spacing between adjacent ligaments, the number of previously formed droplets and the droplet shape. The droplet charge for a static and dynamic model was calculated by COMSOL commercial software. Husam Osman was the principal author of this chapter. Some revisions and recommendations were made by the supervisors Dr. Kazimierz Adamiak and Dr. G.S. Peter Castle. The material in Chapter 4 has been accepted for publication in:

H. Osman, O. Ghazian, K. Adamiak, G.S.P. Castle, H.-T. Fan and J. Simmer, "The charging level of a ligament-droplet system atomized in a uniform electric field," Proc. IEEE/IAS Annual Meeting, Vancouver, BC, pp.1-7, Oct. 2014 (under review to be published in IEEE Trans. Ind. Appl.)

Chapter 5 presented a 3D numerical model to study the effect of the linear and circular array of ligaments on the droplet charge levels. The symmetric boundary conditions were applied for simplicity and the space charge was specified in the region between the atomizer and the target. The effect of the electrode width and length was also reported. Husam Osman was the principal author of this chapter. Some revisions and recommendations were made by the supervisors Dr. Kazimierz Adamiak and Dr. G.S. Peter Castle. The material in Chapter 5 has been accepted for publication in:

H. Osman, G.S.P. Castle, K. Adamiak, H.-T. Fan and J. Simmer, "Estimation of droplet charge forming out of an electrified ligament in the presence of a uniform electric field," IOP Conference on Electrostatics 2015, Southampton, UK, p.46, April 2015.

In Chapter 6, a 3D numerical model was generated using ANSYS to calculate the particle deposition thickness and trajectories on a stationary target and target moving in one and two directions. Different comparisons between the numerical and experimental results were made and they show a good agreement. Husam Osman was the principal author of this chapter. Some revisions and recommendations were made by the supervisors Dr. Kazimierz Adamiak and Dr. G.S. Peter Castle. The material in Chapter 6 has been accepted for publication in:

H. Osman, K. Adamiak, G.S.P. Castle, H.-T. Fan and J. Simmer, "Comparison between the numerical and experimental deposition patterns for an electrostatic rotary bell sprayer," 2015 IMECE Conference, ASME, Houston, TX, USA, accepted for publication, 2015.

In Chapter 7, the electric field was calculated on three different target configurations: a flat target, a target with a protrusion and a target with an indentation. The coating buildup rate was also included in this chapter to study the effect of the model parameters, such as the size of the surface perturbation and the corner radii on the deposition uniformity and transfer efficiency. Husam Osman was the principal author of this chapter. Some revisions and recommendations were made by the supervisors Dr. Kazimierz Adamiak and Dr. G.S. Peter Castle. The material in Chapter 7 has been accepted for publication in:

H. Osman, G.S.P. Castle, K. Adamiak, "Numerical study of particle deposition in electrostatic painting of a perturbed surface," J. Electrostatics, accepted for publication, 2015.

Acknowledgments

First of all, I am extremely grateful to Allah for establishing me to complete this thesis.

I would like to express my sincere thanks to my advisors, Dr. Kazimierz Adamiak and Dr. G.S. Peter Castle, for their invaluable guidance and support during my graduate studies.

I also would like to thank Dr. Nikola Toljic and Osameh Ghazian for help with numerical modeling and Dr. Charles Fan and Mr. Joseph Simmer for their insightful comments and suggestions.

Also, I acknowledge with thanks the joint contributions of the Natural Sciences and Engineering Research Council (NSERC) of Canada and General Motors Company for the financial support and CMC Microsystems for providing an access to COMSOL software that facilitated this research.

Finally, I would like to greatly thank my parents, my wife, Haidy Metwally, and my daughter, Malak Osman, for unceasing encouragement and support.

Table of Contents

List of Tables

List of Figures

Nomenclature

A	empirical coefficient (μC/m^2)
C_i	concentration of particles in cell i
C_d	drag coefficient
C_c	Cunningham correction factor
D	particle diameter (m)
D_f	diffusion coefficient (m^2/s)
d	ligament spacing (m)
E	electric field (V/m)
E_0	external electric field (V/m)
F	external force (N)
F_E	electric force per unit mass (N/kg)
F_e	electrostatic force (N)
F_d	drag force (N)
F_g	gravitational force (N)
g	gravitational acceleration (m/s^2)
$\pm h$	height/depth of the perturbation (m)
I	identity vector matrix
J	current density (A/m^2)
k_0	constant (m^{2}C/kg)
k_1, k_2, k_3	constant coefficients
$L, \boldsymbol{l}$	ligament length (m)
$\dot{M}$	total mass flow rate (kg/s)
$\dot{m}_0$	flow rate factor (kg/s)
$\dot{M}_{35}$	mass flow for 35 μm particle diameter (kg/s)
$\dot{M}_P$	mass flow for a selected P μm particle diameter (kg/s)
m	particle mass (kg)
N	total number of super-particles
N_1	number of injection points
N_2	number of size bands

N_3	number of injection angles
n	radius exponent
P	static pressure (Pa)
$\dfrac{q}{m}$	charge-to-mass ratio (C/kg)
q	particle charge (C)
r_p	protrusion radius (m)
r_i	indentation radius (m)
r_c	corner radius (m)
R_1, R_2, R_3	virtual rings radii (m)
R	radius of electrode (m)
r_{lig}	ligament radius (m)
r	droplet radius (m)
Re	Reynolds number
S_m, S_{Φ_k}	source term
t	time (s)
T	Maxwell stress tensor (N/m^2)
u	fluid velocity (m/s)
u_p, v	particle velocity (m/s)
u'	turbulent velocity component (m/s)
u_{avg}	average velocity (m/s)
u_x, u_y, u_z	fluid velocity components (m/s)
Vf_{in}	volume fraction of droplet
Vf_{ex}	volume fraction of air
V	applied potential (V)
α	re-initialization parameter
γ	surface tension (N/m)
δ_{ij}	Kronecker delta function
δ	Dirac delta function
Γ_k	diffusion coefficient
ε	electric permittivity (F/m)

ε_r	relative permittivity
ε_0	permittivity of free space (8.85×10^{-12} F/m)
ϵ_{ls}	interface thickness parameter
η	dynamic viscosity (Pa.s)
θ	injection angle (degree)
λ	molecular mean free path (m)
μ	particle mobility (m^2/V.s)
μ_i	ion mobility (m^2/V.s)
ρ_f	fluid density (kg/m^3)
ρ_P, ρ	space charge density of charged particles (C/m^3)
ρ_0	particle density (kg/m^3)
ρ_i	space charge density of ions (C/m^3)
σ_r	relative conductivity
$\bar{\bar{\tau}}$	stress tensor (Pa)
Φ_k	arbitrary scalar function
ϕ	scalar electric potential (V)
$\emptyset$	level set function

Chapter 1

Introduction and Objectives

1.1 Introduction

There is often a need to coat the surface of objects for certain purposes. For example, metals are coated to protect them from rust and crops are sprayed to protect them from pests and diseases. The transfer efficiency of paint and finish quality of the target are the ultimate goal in all industrial applications, which can be improved by applying the electrostatic spraying system. This process has become a very important method to employ in a wide range of industrial applications, such as food spraying, automobile manufacturing, printing, medicine and pharmaceutical sciences. The basic principle of electrostatic spray coating is to deposit charged liquid droplets or solid powder particles onto a specified grounded target. The shape of the target surface will directly affect the deposition thickness and the transfer efficiency, especially if it contains some sharp edges and recessed areas. Two major problems in electrostatic liquid painting will occur in this situation: the Faraday cage effect and the edge effect, and they will be discussed in detail in this thesis. The history of development of electrostatic painting and coating process is very interesting and its succinct review was made by Castle [1].

The electrostatic liquid painting process consists of three main stages: 1) atomization and charging, 2) transportation and 3) deposition. The atomization is a process to disintegrate liquid paint into a very fine spray of droplets by electrical or mechanical means, or a combination of both. There are various types of atomizers used in practical applications, such as pressure, rotary, air-assisted, air-blast, electrostatic and ultrasonic. Lefebvre [2] presented a very comprehensive discussion of this topic. As a result of this process, droplets with different size and mass distributions are formed. If the fluid is conducting and an electric field is present during the atomization, the droplets may become electrically charged and can have different charge distributions. Similarly in the case of solid particles, they may become separated and charged using a number of different methods. Both charged droplets and powder particles behave in a like manner once they dispersed. The resulting electrostatic forces can influence the trajectories of the charged droplets, so that

the thickness of the deposition onto a grounded target can be controlled and focused in ways that are not possible, if they are uncharged. Understanding of the charge mechanism is required for the accurate space charge prediction. Cross [3] discussed four mechanisms of electrostatic charging used in many industrial applications and known as corona, conduction, induction and tribo-charging. Each mechanism has its own advantages and disadvantages, and area of usage.

The transport of charged droplets takes place in the region between the atomizer and the target. Because the charged droplets experience simultaneous action of several forces, such as aerodynamic, electrostatic, gravitational and inertial forces, the transport process is very complex. The combined action of these forces determines the trajectories of the charged droplets. When the droplets are very small, the gravitational force is negligible, but the aerodynamic and the electric forces are dominant.

1.2   Objectives of research

The objectives of this research are to investigate through numerical modeling: the droplet charge to radius and ligament length dependency in the ligament-droplet system atomized in a uniform electric field, the particle deposition pattern on a stationary and moving target with verification by experimental data, and calculating the electric field distribution as well as the particle deposition and trajectories on perturbed surfaces. The main aspects of this research are:

1.2.1   Estimation of droplet charge level

The charging level or, more specifically, the charge-to-mass ratio on a liquid droplet is a critical parameter that needs to be determined in order to accurately predict the behavior of the droplet in the electrostatic coating process and is considered to be the most important parameter that affects the spraying characteristics. The effect of various factors on the droplet charge levels, such as the droplet radius, the ligament radius, the droplet shape, the presence of adjacent ligaments, the previously formed droplets, the space charge and the width of the electrode, need to be investigated. The study considers single ligaments and also presents a comparison between a linear and circular array of ligaments. In addition, a

preliminary dynamic model of the droplet formation is developed to verify the calculated droplet charge from a simplified stationary model.

The COMSOL commercial software [4] using Finite Element Method was used to estimate the charging level of spherical droplets, which are attached to electrified ligaments ejected from the atomizer's surface. Many cases with different boundary conditions were examined to study the effects of various model parameters on the droplet charge. For a more realistic computational model, the circular array of ligaments at the surface of the sprayer was simulated in order to predict droplet charge in this situation. In this study, experimental results were used for validating those predicted by the numerical simulations.

1.2.2   Numerical modeling of electrostatic coating process

In this research, the electrostatic coating process has been analyzed numerically with the aid of Computational Fluid Dynamics (CFD) commercial software ANSYS [5]. This numerical tool proves its capability to solve and predict the dynamic motion of the particles under the influence of different kinds of forces including the electrical and mechanical forces. Due to the complexities in such a process, it is necessary to keep the computation time within an acceptable level, but preserving sufficient accuracy when large number of model parameters need to be analyzed for optimization.

The numerical modeling of the spraying process involves the liquid as the discrete phase in the form of droplets and the compressed air as the continuous phase. The surface of the atomizer's tip is connected to a high voltage to create a charging electrode, while the surface of the target of a specified shape is grounded. The particles were modeled as conducting spheres. Evaporation, breakup, collisions and coalescence of particles were neglected. The injection pattern was proposed to achieve a good agreement with experimental data. A comparison between the numerical and experimental results was also made for cases of a stationary and moving target.

1.2.3 Investigation of the deposition pattern on surface with perturbations

The electric field distribution of the flat surfaces and surfaces with perturbations has been analyzed in order to examine the capability to predict the coating thickness uniformity and the transfer efficiency by calculating the electric field. Different shapes on the perturbed area, the radii of the corner and the space charge were assumed to investigate their effects on the electric field distribution so that the places of high concentration of the electric field (edge effect) and shielding of the field (Faraday cage effect) can be identified. The numerical model has been generated using COMSOL to calculate the electric field in each case. The particle deposition and the particle trajectories were obtained for similar cases using ANSYS, such that the target surface includes a protrusion or indentation at the center. The injections of mono- and poly-dispersed charged and uncharged particles were considered.

The results reveal that the electric field is non-uniform in the region of the perturbation and depends on the model parameters. Also, a very good correlation with the determination of the particle deposition patterns on different surface perturbations was realized.

1.3 Thesis organization

This thesis is organized in the following Chapters. The work presented in Chapters 4, 5, 6 and 7 have been accepted for publication.

Chapter 1 is the introductory chapter, which includes the motivation for writing this thesis and presenting the thesis organization.

Chapter 2 covers a thorough review of the scientific literature dealing with the atomization process and the most important mechanisms of charging the particles, as it is considered to be the first stage of the electrostatic coating process. There is also a summary of previously published work that is related to the investigation of the electrostatic painting of simple as well as complicated surfaces using different numerical and experimental techniques, which were exploited for the purpose of this research.

Chapter 3 presents a collaborative research with GM to study the deposition pattern and trajectories of paint droplets in the electrostatic coating process. Many cases were performed using ANSYS to simulate a modified injection pattern, which includes a set of injection angles and fractional mass flow rate at each injection point. The objective of the study of this chapter is to improve agreement between numerical simulation and experiment. Only an injection of charged monodispersed particles on a stationary target was included and a de-rating factor for solvent evaporation was assumed. In the first stage of this analysis, prior to particle injections, the contours of air velocity distribution were obtained across a series of perpendicular planes to the axis of the spray gun.

Chapter 4 discusses the mathematical approximation used to predict the droplet charge level, which was represented as a function of its radius to some exponent and ligament length. Also, the estimation of the charge magnitude in a ligament-droplet system was made for different cases to study the effect of the model parameters on the charge magnitude, such as the ligament length and width, the spacing between adjacent ligaments, the number of previously formed droplets and the droplet shape. COMSOL commercial software was employed to calculate the droplet charge for a static and dynamic model.

In Chapter 5, a 3D numerical model was generated for a linear array and circular of ligaments. In the linear array, the droplet charge was calculated for variations of the high voltage electrode width, where the model parameters, such as the ligament length and spacing are kept fixed. The numerical model was also modified to estimate the charge magnitude for the case of a circular array of ligaments by simulating the ligament-droplet system at the edge of the atomizer's tip. The symmetric boundary conditions were applied in this case for simplicity and the space charge was specified in the region between the atomizer and the target. The numerical results of the charge-to-mass ratio were very close to the theoretical predicted values. The computational domain and the meshing parameters were carefully selected and the effect of the electrode width on the droplet charge was reported.

In Chapter 6, a full 3D numerical model using ANSYS was generated to simulate the industrial electrostatic coating process. The injection pattern introduced in Chapter 3 was

modified by assuming three virtual injection rings at a distance from the atomizer's tip to create a shower of injection pattern. This can improve the deposition thickness at the central spray cone on a stationary grounded target plate. The injection of polydispersed particles was considered in this model and the moving mesh was also incorporated to predict the thickness profile on a target moving in one and two directions. The distribution of charge-to-mass ratio was assumed to be reciprocal to the particle diameters, as predicted theoretically, since experimental data was not available. It is assumed that all the droplets have the same surface charge density, i.e. charge-to-mass ratio is reciprocal to the diameter, and that the 35 μm droplet has a q/m of 1 mC/kg. The simulation results were justified by the experimental data.

In Chapter 7, the investigation on the electric field distribution and the deposition thickness was analyzed for a surface with perturbations in 2D axisymmetric domain. Different model parameters, such as the size of the perturbation, the radius of the corner and the space charge were examined. Three surface configurations were tested: a flat target, a target with a protrusion and a target with an indentation at the center. The coating buildup rate for particles of different sizes and charge-to-mass ratios were also included in this study to examine the correlation with the calculated values of the electric field.

In Chapter 8, the conclusions and summary of this thesis is presented. Also, this chapter contains recommendations for future work.

References

[1] G.S.P. Castle, "A century of development in applied electrostatic; nothing static here," IEEE Trans. Dielectr. Electr. Insul., vol.18, No.5, pp.1361-1365, 2011.

[2] A.H. Lefebvre, Atomization and Spray, New York: Hemisphere Publishing Co., 1989.

[3] J.A. Cross, Electrostatic: Principles, Problems, and Applications, Adam-Hilger: Bristol, UK, 1987.

[4] www.comsol.com

[5] ANSYS FLUENT User's guide, www.ansys.com

Chapter 2

Literature Review

2.1 Introduction

An overview of the scientific literature that deals with the atomization and the charging of particles is presented in this Chapter. This process is the first stage of the electrostatic coating process. In the atomization process, the liquid paint is dispersed into a very fine spray of droplets by either electrical or mechanical forces, or both. The practical electrostatic spray guns are available in many designs, including hydraulic (airless), pneumatic (compressed air) and centrifugal atomizers (rotating disks and bells). Michelson [1] and Bailey [2] in their books presented a very comprehensive review of the practical electrostatic spray guns in liquid painting. The recent evolution of high-speed rotary bell atomizers has received increasing industrial attention among other atomizers. They use mechanical methods to atomize the liquid into droplets and the electrostatic methods to charge the droplets. Both electrical and mechanical forces usually govern the movement of the particles between the atomizer and the target.

In the charging stage, the droplet or powder particles are charged by being exposed to strong electric field. Understanding of the charging mechanism is required for the accurate space charge prediction. Corona, tribo-charging, conduction and induction are four important changing mechanisms used in industrial electrostatic applications. Each charging mechanism has its own advantages, disadvantages and area of usage.

2.2 Atomization and particle formation

Various methods to atomize a liquid sheet into spray have been discussed by Lefebvre [3]. The development of the liquid sheet leads to disintegration into ligaments and then further surface disturbances produce droplets. The internal geometry of the atomizer and the physical properties of the gas and liquid are very important factors to determine the spray characteristics. Because of the complexity of this process, many empirical equations have been derived to explain the relation between various model parameters. Recently, the

Computational Fluid Dynamic (CFD) techniques have become a major tool for analyzing different types of atomizers.

For the first time the phenomenon of liquid jet disintegration was studied theoretically by Rayleigh [4], who investigated the instability of a non-viscous liquid jet at low velocity and small perturbations. He found that when the wavelength of the disturbance is greater than the jet circumference, droplets can be produced by the breakup process.

Rayleigh's analysis was extended by Weber [5] to include viscous liquids. He found that if the wavelength of the disturbance is less than a certain value, the surface tension tends to damp out the disturbance; otherwise it causes rapid jet disintegration. His theoretical predictions did not agree well with experimental data, as pointed out by Sterling and Sleicher [6], who improved Weber's theory with a partial success. Rayleigh in his analysis of the instability of a liquid jet did not examine the effect of electric charge on the jet. Schneider et al. [7] extended and generalized Rayleigh's work by including this effect.

Hines [8] studied theoretically and experimentally the charging and atomization of an individual fluid jet in an electrostatic field. He found a good agreement between the experimental and the theoretical values of the droplet size as a function of surface tension and charge-to-mass ratio. Both theoretical and experimental data presented in his work showed that the atomization rate increases as the electric field at the atomizing surface is increased. He also presented approximate formulas to relate various quantities, such as the droplet size and the charge-to-mass ratio to the fluid properties and the electric field intensity.

The breakup of a liquid sheet into ligaments and further disintegration into droplets are governed by two groups of forces: bulk forces (e.g. electric force, gravitational force, inertial force and drag force) and normal and tangential stresses at the liquid surface (e.g. electric stress due to the surface charge density and the local electric field, stress due to pressure difference on both sides of the liquid surface and stress due to dynamic viscosity of fluid). The physical properties of the liquid determine the properties of the droplets, but the surface tension is the most important factor responsible for the shape of liquid droplets. The properties of a liquid surface or interface between a liquid and gas or vapor are usually

related to the surface density of energy. As the attraction force between the liquid's molecules is greater than the one between molecules in the gas, the liquid has higher surface tension. The surface tension has a major effect on the atomization process. Tolman [9] showed that the surface tension depends on the droplet radius. The effect of other factors on the surface tension, such as ionic salts and active agents has been studied in [10-12].

2.3 Particle charging mechanisms

There are four basic particle charging mechanisms used in industrial electrostatic applications, as discussed by Cross [13]: corona, triboelectric, induction and conduction charging. Each charging mechanism has its own advantages and disadvantages, and area of usage. A brief overview of each mechanism is presented in the following sections.

2.3.1 Corona charging

Corona charging is a well-known mechanism responsible for charging liquid droplets [2] or powder particles [14] in many applications. It involves applying a high potential to a very sharp needle, sufficient to produce continuous gas discharge in the air. Positive, negative or alternating potentials may be used. An electrode at a negative potential attracts positive ions and repels electrons away by the high electric field. These electrons will be accelerated causing additional collisions, which produce an avalanche of electrons and positive ions, as depicted in Figure 2.1. This process continues until the new electrons are formed far enough away, such that they are unable to gain sufficient energy to ionize more neutral molecules. The positive ions will be directed towards the needle. Depending upon the gaseous environment, electrons can attach to neutral molecules to form a space cloud of negative ions. An electrode at a positive potential behaves in a similar manner as a source of positive ions. The ions created at the gun nozzle and are drifted through the gas gap with different velocities. The corona discharge region can be subdivided into two regions: ionizing region, which contains the charge carriers of both polarities, and drift region that is characterized by the presence of only one polarity charge carriers. The great advantage of corona charged guns is that they offer a dependable source of ions and strong electrostatic field resulting in effective charging and higher deposition. However, the redundant ions generate a self-limiting effect and the strong concentration of field lines on

sharp edges lead to the Faraday cage effect and edge effect, which are prominent on coating complex geometrical surfaces and are discussed in Chapter 7. A very comprehensive literature review to understand the basic physical processes in corona discharge was presented in [15].
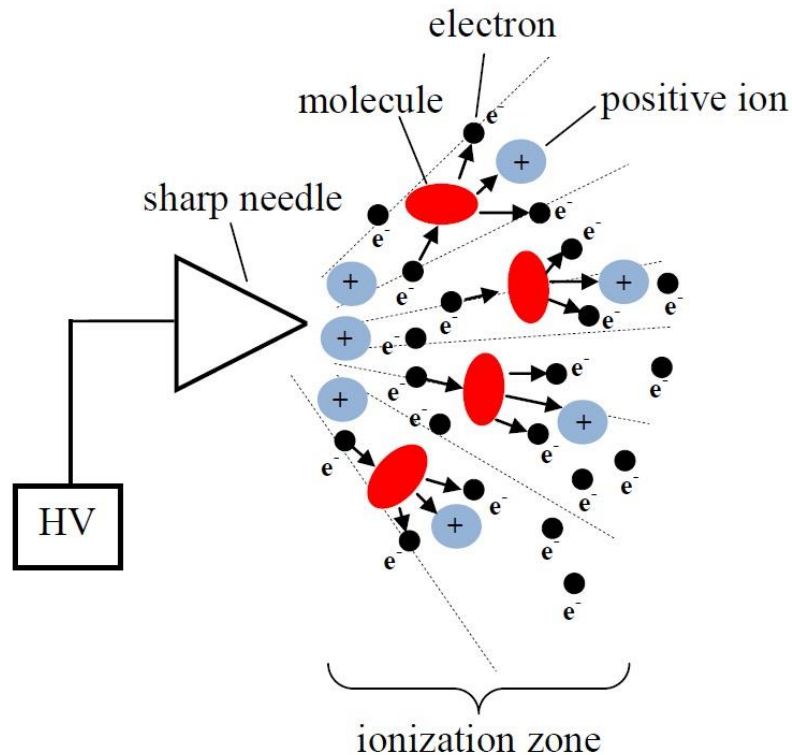
Figure 2.1: Negative corona discharge

2.3.2   Triboelectric charging

Triboelectric charging is another mechanism used for particle charging, mainly for powders, and it is based on the particles rubbing with the material inside the spray gun for sufficient time, without the use of a high voltage source. For example, when two different solid materials contact each other, the electrical charges are transferred at the point of contact, which magnitude is dependent on the work function of the two materials in contact. The material with higher work function gains electrons and charges negatively, while the material with lower work function loses electrons and charges positively. The charge flow terminates when the work functions of both materials are equalized. Also, the amount of

charge transferred depends on the area and the number of contacts. The environmental conditions, such as the ambient temperature and the relative humidity may also affect the charge flow rate [16].

Mazumder et al. [17] measured the electric charge for different powder particle sizes, which were tribo-electrically charged. Their experimental data showed that the charge magnitude increases linearly with the surface area of the particle and they also found that 20%-60% of the particles were charged with opposite polarity. Thomas et al. [18] developed a device allowing the measurement of tribo-charging powder particles during the conveying through a metallic pipe and also during the transport through an insulating pipe.

While the electric field in a corona charging system is generated by the external potential difference in combination with the space charge of ions and charged particles, the electric field in tribo-charging system is produced only by the space charge of the tribo-charged particles. Thus, the electric field is weaker and may be insufficient for transporting the particles toward the grounded target. The air flow, which entrains the particle in the space between the tribo-gun and the target, plays an important role. Due to the reduced electric field, the edge effect, Faraday cage effect and back ionization become less important and the corners can be coated more uniformly, which is discussed in the next section. Moyle and Hughes [19] presented a very good comparison between the corona and the triboelectric charging system in powder coating.

2.3.3   Induction and conduction charging

Induction charging refers to a process in which a voltage is applied to an electrode, which is placed near a grounded atomized liquid. The electric charge flows from the ground to the liquid material surface due to the induced electric field and reside on the surface after droplet separation. On the other side, the conduction charging requires a direct connection between the applied voltage and the atomized liquid. In this situation, the electric charge flows directly from the voltage supply to the surface of the material. When the liquid is dispersed into droplets, the charge is trapped on the droplets. Generally, induction and conduction charging mechanisms are considered to be similar, as shown in Figure 2.2, and

are widely used in various liquid spraying processes for conductive or semi-conductive liquid material, such as industrial painting and food spraying.

(a) Induction charging   (b) Conduction charging
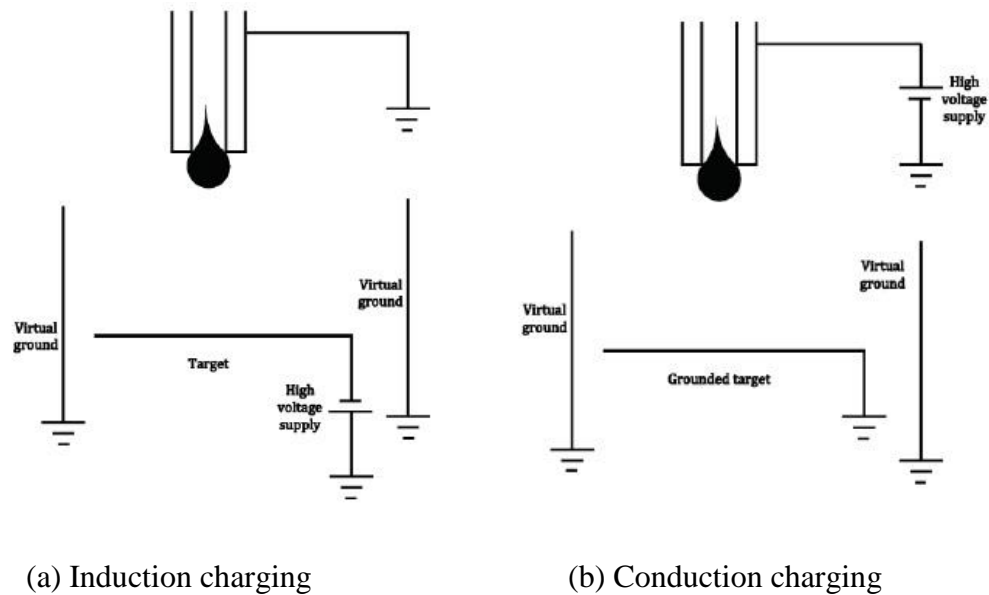
Figure 2.2: Induction and conduction liquid charging in two-electrode system

For an ideal two-electrode induction and conduction charging arrangements, as shown in Figure 2.2, the nozzle serves as one electrode and the target as the other electrode, but they are isolated from adjacent "virtual" grounds. In this case, the electric field distribution is the same in both mechanisms except for a polarity difference. However, for a three-electrode arrangement, which is commonly used in practice, the nozzle serves as one electrode, a second electrode is mounted close to the nozzle, and the target serves as the third grounded electrode, as shown in Figure 2.3. In this case, the charging mechanism, electric field distribution, energy conversion, and space charge for conduction are different than that for induction charging.

Zhao et al. [20] made a very good comparison between the two charging mechanisms. They found that the conduction charging produces a larger target current, smaller electrode current and larger drift current, but in the induction charging the target current depends only on the space charge field, which causes larger electrode current and surface discharge at lower voltage. A limitation of conduction and induction charging is that they can not be used to charge insulating materials and are limited to relatively well conducting coatings.

<div align="center">(a) Induction charging   (b) Conduction charging</div>
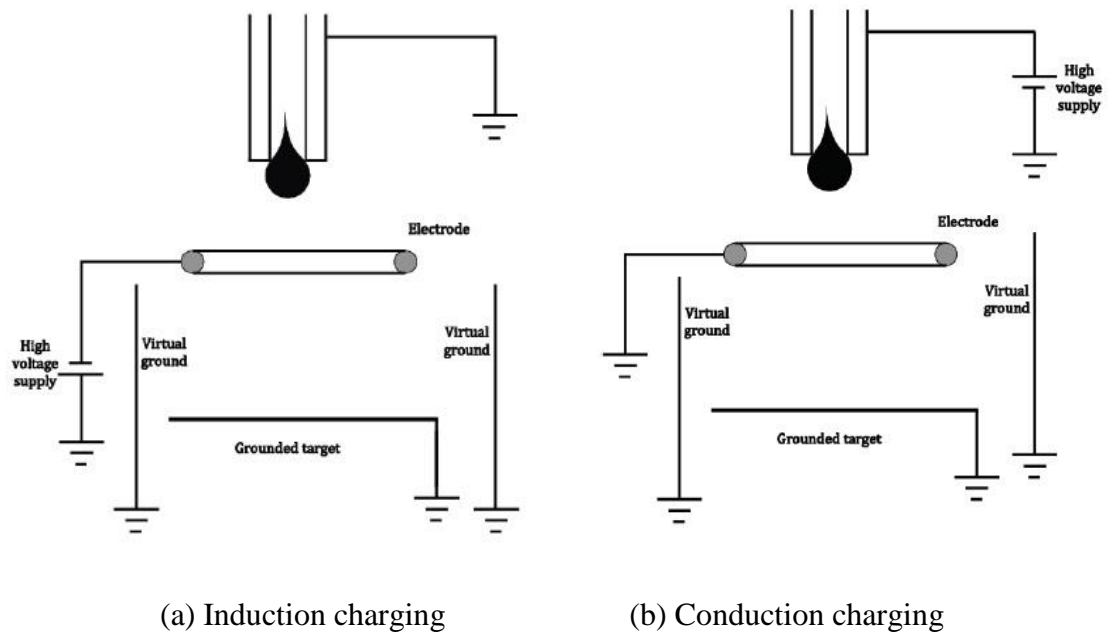
<div align="center">Figure 2.3: Induction and conduction liquid charging in three-electrode system</div>

<div align="center">[20]</div>

2.4 Numerical modeling of electrostatic coating process

The fast-growing computational techniques facilitate the capability to predict the droplet charge level, their trajectories and estimate the deposition pattern in the electrostatic painting system. Ellwood et al. [21] and Böttner et al. [22] performed CFD numerical simulations of a 2D axisymmetric stationary spray gun. Their simulations included the coupling of the flow field with the electrostatic field, and the effect of the paint particles on the continuous phase assuming a laminar model. They showed that the space charge has a great impact on the particle trajectories and, therefore, it highly influences the results. Also, they found that the coupling of the particles with the continuous phase is very important only in the region near the injection locations, where the particle concentration is high. Ye et al. [23] analyzed a complex spray gun using a corona charging mechanism to predict the deposition thickness on a stationary target plate. The particle size and charge distributions in their study were based on actual measurements. They used the static spray pattern from a commercial CFD FLUENT software to predict the dynamic deposition thickness by artificially moving the spray pattern along a straight line and integrating the

mass in this direction. The calculated results in both cases were compared with the experimental ones and a significant effect of the space charge on the particle deposition pattern was found.

Another perspective was shown by Colbert et al. [24,25], where they presented parametric studies of the effect of the individual variables involved in the electrostatic spray system on the overall spray pattern and transfer efficiency. Their results showed a ring pattern with no deposition at the center of a flat target and increased accumulation on the edge. Also, Im et al. [26] performed a numerical simulation of the spray transfer process in an electrostatic rotary bell applicator using CFD method. They found that the spray shape is very sensitive to changing the charge-to-mass ratio and electric force, which strongly affects the numerical transfer efficiency. Also, they found that although the transfer efficiency is decreased with increasing the shaping airflow rate, the spray pattern is more uniform on the target surface.

Many researchers tried to validate their numerical simulations by experimental measurements and they attained a reasonable agreement. A comparison between the experimental and numerical results of the deposition thickness produced by high speed rotary bell atomizer has been attempted by Domnick et al. [27] for simple target geometry. They considered a direct charging mechanism, where high voltage was applied directly to the rotating bell and the effect of the corona was neglected. They also used a rotary bell atomizer with six external corona needles which were arranged symmetrically around the atomizer body to predict the deposition thickness and transfer efficiency on a curved object [28]. They chose the target geometry as a rear part of a car body. When they compared their numerical results of the deposition pattern with the experimental ones, they found a good agreement, but the simulated coating thickness at the positions very close to the edges was overestimated due to the edge effect.

Adamiak [29,30] performed a 2D simulation of tribo-charged powder particle trajectories. He assumed a cylindrical tribo gun at some distance from a vertical infinite ground plane. He assumed mono- and poly-dispersed powder particles for injection and found that modeling a triboelectric system is much more difficult than a corona system because in the

corona system the space charge field is dominant by ions and the field due to the charged particles can be ignored, but in the triboelectric system space charge density depends only on particles. Toljic et al. [31,32] described a full 3D numerical model using FLUENT to predict the coating thickness for a moving target surface. They assumed a conduction charging in their model and the target took the shape of a car door. Their results showed some improvements in the deposition uniformity compared with the case of a stationary target. The transfer efficiency was also higher for the cases of charged particles as compared with the case of neutral particles. They also examined the effect of different model parameters on the deposition pattern, such as the shaping air mass flow rate, the applied voltage, the particle mass flow rate and the charge-to-mass ratio. Their results revealed that the deposition profile is strongly affected by the shaping air mass flow rate.

2.5   Electrostatic coating of complex shaped objects

Three major problems may occur, when the coating target includes some sharp edges and recessed areas. These are the Faraday cage effect, the edge effect and the back ionization. The existing knowledge of numerical modeling of the electrostatic coating process is utilized to investigate their effects on the deposition pattern uniformity and the transfer efficiency of paint. An overview of these phenomena is presented first in this section and a comprehensive work is presented in Chapter 7 to investigate the effect of the Faraday cage effect and the edge effect on the particle deposition pattern.

2.5.1   Faraday cage effect

The Faraday cage effect is a result of the fact that the electric field lines are shielded and are restricted from penetrating into indentations. When a target has some recessed areas on its surface, the electric field concentrates at corners and sharp edges, but it is very limited and is not uniformly distributed along the surface in the recessed areas. This leads to the possibility that some areas will be less coated. Because the field does not penetrate the recessed area, the charged particles are attracted to the highest field region, as shown in Figure 2.4. The electric field in close vicinity to the target surface is composed of fields created by the sprayer charging electrode and the space charge [13]. The combination of these two fields facilitates paint particles to be deposited on the target surface.

Figure 2.4 illustrates that neither the field created by the sprayer electrode, nor the field of space charge between the sprayer and the target surface can penetrate inside the recessed area. Therefore, the only source of assistance is the field created by the space charge of paint particles delivered by the air stream inside the recess. If the channel of indentation is very narrow, back ionization is rapidly developed on its edges and reduces the charged particles to pass between the edges of the channel. However, the cumulative space charge of the charged particles delivered inside the channel will not be sufficient to create a strong enough electric force to overcome the air turbulence.
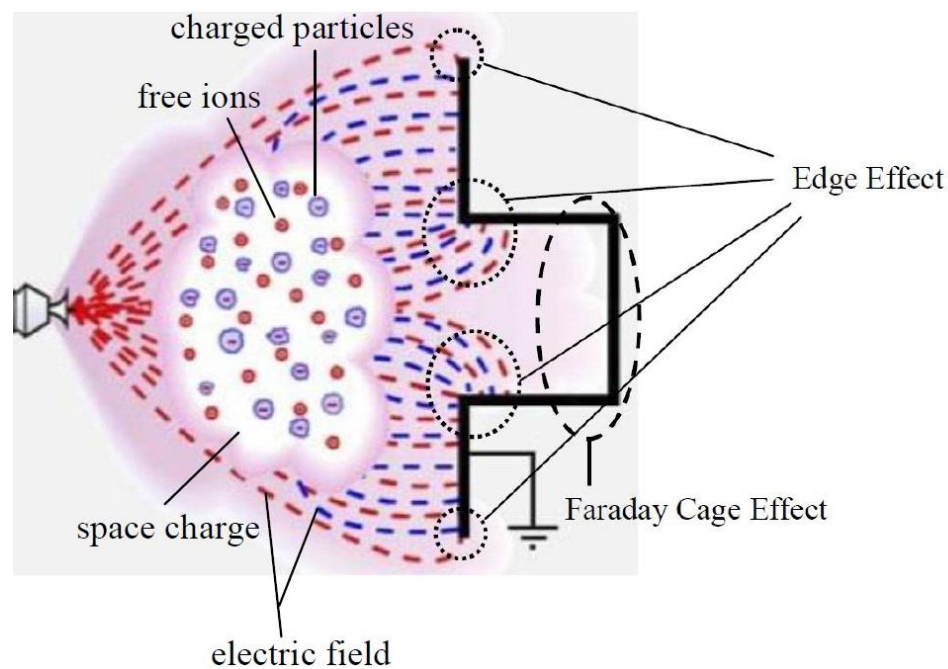
Figure 2.4: Faraday cage effect and edge effect

In powder coating, Adamiak [29,30] investigated the particle trajectories and deposition in the tribo-charging powder coating system assuming different target configurations. He found that for large particle diameters and small charge-to-mass ratio, more particles penetrated and were deposited inside the cavity, whereas smaller particles were attracted to the corners, as the charge-to-mass ratio increased. Biris et al. [33] developed a novel charger to charge two kinds of powder particles bipolarly such that the net charge-to-mass ratio is close to zero. They concluded that to overcome the Faraday cage penetration problem and to have a uniform deposition thickness, the charge-to-mass ratio must be

reduced. Also, Biris et al. [34] studied the Faraday cage effect on the uniformity and the corrosion resistance of the powder coating using corona spray gun.

2.5.2   Edge effect

If most of the electric field concentrates on the corners and edges, the particle deposition thickness will be greatly enhanced in these areas, which results in uneven distribution of paint, as shown in Figure 2.4. In the paint industry this is known as window-paning and there are two negative effects will accompany this process. First, fewer particles have a chance to go inside the recessed area since the charged particles are strongly pushed by the electric field towards the edges. Second, in the case of corona discharge free ions will be generated and follow the field lines towards the edges, quickly saturate the existing coating layer with extra layers.

In liquid painting, Toljic et al. [32] succeeded in creating a full 3D numerical model to investigate the deposition thickness on a moving target, which took the shape of a car door. They noticed the edge effect as a very high deposition thickness occurs around the door handle. Domnick et al. [28] also discussed the static and dynamic deposition thickness profile on a rear part of a car body and their results revealed a very high thickness levels near the edges.

2.5.3   Back ionization†

This effect occurs in powder coating. When charged powder coating is applied to the target surface, the electric field strength inside the layer of powder coating increases. Every new powder particle deposited increases the cumulative charge of the powder layer and the mirror charge induced on the target surface. As additional charged powder is added, the strength of the electric field inside the powder coating layer becomes sufficient to ionize air trapped between powder particles. Back ionization greatly reduces the transfer efficiency and deteriorates the finish quality. This phenomenon is also highly dependent on the type of spray gun used as reviewed by Bailey [35]. Free ions are the major cause of

---

† The major concern of this thesis is about the electrostatic liquid painting and so back ionization is not included in the presented research.

back ionization in corona applications. The investigation on the back ionization and suggested solutions to reduce this effect has been presented by many researchers and most of them concluded that decreasing the corona current will reduce the number of free ions in the space between the target and the atomizer. Adamiak et al. [36] investigated the problem of quick corrosion of car wheel edges and confirmed that pin holes in the powder coating resulting from back corona discharge and they suggested that the charge-to-mass ratio of the powder must be reduced. No single solution to all challenges would work in every type of application. However, these three phenomena may be interrelated in a given application, but they also occur separately in different geometries. Table 2.1 summarizes some characteristics of the three phenomena.

Table 2.1: Some characteristics of the three phenomena

Phenomenon	Material	Occurrence	Suggested solution
Faraday cage effect	liquid or powder	complex surfaces	turn down the electrode voltage (i.e. reduction of the electric field)
Edge effect	liquid or powder	flat and complex surfaces	turn down the electrode voltage (i.e. reduction of the electric field)
Back ionization	powder	flat and complex surfaces	reduce the total number of ions by replacement the corona charging system with the triboelectric system

References

[1] D. Michelson, Electrostatic Atomization, Adam-Hilger: Bristol, UK, 1990.

[2] A.G. Bailey, Electrostatic Spraying of Liquids, New York: John Wiley and Sons Inc., 1988.

[3] A.H. Lefebvre, Atomization and Spray, New York: Hemisphere Publishing Co., 1989.

[4] L. Rayleigh, "On the instability of jets," Proc. London Math. Soc., vol.10, pp.4-13, 1878.

[5] C. Weber, "Disintegration of liquid jets," Z. Angew, Math. Mech., vol. 11, No. 2, pp.136-159, 1931.

[6] M. Sterling, C.A. Sleicher, "The instability of capillary jets," J. Fluid Mech., vol.68, pp.477-495, 1975.

[7] J.M. Schneider, N.R. Lindblad, C.D. Hendricks, Jr., J.M. Crowley, "Stability of an electrified liquid jet," J. Appl. Phys., vol.38, No.6, pp.2599-2605, 1967.

[8] R.L. Hines, "Electrostatic atomization and spray painting," J. Appl. Phys., vol.37, No.7, pp.2730-2736, 1966.

[9] R.C. Tolman, "The effect of droplet size on surface tension," J. Chem. Phys., vol.17, No.3, pp.333-337, 1949.

[10] J.T. Davies and E.K. Rideal, Interfacial Phenomena, New York: Academic Pres, 1961.

[11] J.T. Davies and R.W. Makepeace, "Measurement of surface ages of water jets," Am. Inst. Chem. Eng. J., vol.24, pp.524-530, 1978.

[12] R. Van den Bogaert and P. Joos, "Dynamic surface tensions of sodium myristate solutions," J. Phys. Chem., vol.83, pp.2244-2248, 1979.

[13] J.A. Cross, Electrostatic: Principles, Problems, and Applications, Adam-Hilger: Bristol, UK, 1987.

[14] J.F. Hughes, Electrostatic Powder Coating, John Wiley & Sons, 1984.

[15] L.B. Loeb, Electrical Coronas, Their Basic Physical Mechanisms, University of California press, Berkeley, CA, 1965.

[16] W. Kleber, "Electrostatic powder gun design," J. Electrostatics, vol.30, pp.393-402, 1993.

[17] M.K. Mazumder, S. Banerjee, R.E. Ware, C. Mu, N. Kaya,C.C. Huang, "Characterization of tribocharging properties of powder paint," IEEE Trans. Ind. Appl., vol. 30, No.2, pp.365-369, 1994.

[18] A. Thomas, K. Saleh, P. Guigon, C. Czechowski, "Tribocharging behaviour of automotive powder coatings," J. Phys.: Conf. Ser., vol.142, No.1, 2008.

[19] B.D. Moyle and J.F. Hughes, "Powder coating-corona versus tribo charging," J. Electrostatics, vol.16, pp.277-286, 1985.

[20] S. Zhao, G.S.P. Castle, K. Adamiak, "Comparison of conduction and induction charging in liquid spraying," J. Electrostatics, vol.63, pp.871-876, 2005.

[21] K.R.J. Ellwood, J. Braslaw, "A finite-element model for an electrostatic bell sprayer," J. Electrostatics, vol.45, pp.1-23, 1998.

[22] C.-U. Bottner, M. Sommerfeld, "Numerical calculation of electrostatic powder painting using the Euler/Lagrange approach," Powder Technol.,vol.125, pp.206-216, 2002.

[23] Q. Ye, T. Steigleder, A. Scheibe, J. Domnick, "Numerical simulation of the electrostatic powder coating process with a corona spray gun," J. Electrostatics, vol.54, pp.189-205, 2002.

[24] S.A. Colbert, R.A. Caircross, "A computer simulation for predicting electrostatic spray coating patterns," Powder Technol., vol.151, pp.77-86, 2005.

[25] S.A. Colbert, R.A. Caircross, "A discrete droplet transport model for predicting spray coating patterns of an electrostatic rotary atomizer," J. Electrostatics, vol.64, pp.234-246, 2006.

[26] K.-S. Im, M.-C. Lai, S.-T.J. Yu, R.R. Matheson, Jr., "Simulation of spray transfer processes in electrostatic rotary bell sprayer," J. Fluids Eng., vol.126, pp.449-456, 2004.

[27] J. Domnick, A. Scheibe, Q. Ye, "The simulation of the electrostatic spray painting process with high-speed rotary bell atomizers, Part I: Direct charging," Part.Part.Syst.Charact., vol.22, pp.141-150, 2005.

[28] J. Domnick, A. Scheibe, Q. Ye, "The simulation of the electrostatic spray painting process with high-speed rotary bell atomizers, Part II: External charging," Part.Part.Syst.Charact., vol.23, pp.408-416, 2006.

[29] K. Adamiak, "Numerical investigation of powder trajectories and deposition in tribocharge powder coating," IEEE Trans. Ind. Appl., vol.37, pp.1603-1609, 2001.

[30] K. Adamiak, "Numerical modeling of tribo-charge powder coating systems," J. Electrostatics, vol.40&41, pp.395-400, 1997.

[31] N. Toljic, K. Adamiak, G.S.P. Castle, H.H. Kuo and C.T. Fan, "3D numerical model of the electrostatic coating process with moving objects using a moving mesh," J. Electrostatics, vol.70, pp.499-504, 2012.

[32] N. Toljic, K. Adamiak, G.S.P. Castle, H.H. Kuo and C.T. Fan, "A full 3D numerical model of the industrial electrostatic coating process for moving targets," J. Electrostatics, vol.71, pp.299-304, 2013.

[33] A.S. Biris, S. De, C.U. Yurteri, M.K. Mazumder and R.A. Sims, "Parametric study of the Faraday cage effect of chaged particles and its implications in the powder coating process," Proc. of the 37th IEEE/IAS Annual Meeting, Pittsburg, PA, vol.2, pp.995-1000, 2002.

[34] A.S. Biris, S. De, C.U. Yurteri, M.K. Mazumder and R.A. Sims, "Surface defects and corrosion in electrostatically deposited powder films," Proc. of the 37th IEEE/IAS Annual Meeting, Pittsburg, PA, vol.4, pp.2460-2465, 2002.

[35] A.G. Bailey, "The science and technology of electrostatic powder spraying, transport and coating,"J. Electrostatics, vol.45, pp.85-120, 1998.

[36] K. Adamiak, G.S.P. Castle, I.I. Inculet, and E. Pierz, "Numerical simulation of the electric field distribution in tribo-powder coating of conducting cylindrical objects," IEEE Trans. Ind. Appl., vol.30, pp.215-221, 1994.

Chapter 3

Numerical Simulation of an Industrial Electrostatic Coating Process

3.1 Introduction

This chapter summarizes the collaborative research project with General Motors Company to study the deposition thickness and particle trajectories in the electrostatic coating process in the automobile industry. The objective of this project was to produce a reliable numerical model of the electrostatic coating process and to attain a satisfactory agreement between the numerical and experimental results for the same input parameters. This project was divided into two parts. The aim of the first part was to create a simple numerical model in 2D, which was later expanded into 3D, using a CFD commercial software ANSYS-FLUENT [1]. The numerical model was examined for variations of different parameters, such as the mesh density, shaping air velocity, particle size and charge-to-mass ratio. To validate the model, a comparison between the numerical and experimental results of the particle deposition pattern was made. It was found that several critical parameters can affect the painting process: the atomizer geometry, paint properties, target shape, atomizer-to-target distance, mass flow rate of particles and assisting air speed, electric potential, number of injected particles, particle size and charge-to-mass ratio.

The second part, which is discussed in this Chapter and Chapter 6, was to develop the previous 3D model to handle different configurations with a stationary target and a target having relatively complex motion patterns. Also, the work presented in Chapter 7 utilized this model with further modification. The incorporation of the moving mesh capability was included in this study and the injection of the spray pattern was modified to achieve more realistic deposition pattern. All relevant mechanical and electrical phenomena were also included, such as the shaping air effects, the motion of injected particles and the coated target, the space charge and the electrohydrodynamic flow effects. Although several physical and operational variables are believed to have significant effects on the electrostatic liquid painting process, the high degree of interactions between them makes it difficult to consider one issue at a time.

The theory behind the numerical modeling, the description of the computational domain, the coupling between the discrete and continuous phase and the simulation results are summarized here.

3.2   Mathematical model

The mathematical framework of the continuous phase, discrete phase and the electric field are discussed in the following sections.

3.2.1   Continuous phase

The continuous phase refers to the air flow. ANSYS solves the conservation equations for both mass and momentum. Additional transport equations are also solved when the gas phase is turbulent. The equation for conservation of mass can be described as

$$\frac{\partial \rho_f}{\partial t} + \nabla \cdot \left(\rho_f \mathbf{u} \right) = S_m \tag{3.1}$$

where ρ_f is the fluid density, t is the time, $\mathbf{u}$ is the gas velocity and S_m is the mass added to the continuous phase from the dispersed second phase. For the three dimensional geometries, the continuity equation can be written as

$$\frac{\partial \rho_f}{\partial t} + \frac{\partial (\rho_f u_x)}{\partial x} + \frac{\partial (\rho_f u_y)}{\partial y} + \frac{\partial (\rho_f u_z)}{\partial z} = S_m \tag{3.2}$$

where u_x, u_y and u_z are the velocity components in each direction.

Conservation of momentum in a non-accelerating reference frame is given by

$$\frac{\partial (\rho_f \mathbf{u})}{\partial t} + \nabla \cdot \left(\rho_f \mathbf{u}\mathbf{u} \right) = -\nabla P + \nabla \cdot \bar{\bar{\tau}} + \rho \boldsymbol{g} + \boldsymbol{F} \tag{3.3}$$

where P is the static pressure, $\bar{\bar{\tau}}$ is the stress tensor, $\rho \boldsymbol{g}$ is the gravitational force and $\boldsymbol{F}$ is the external body force. Flow turbulence effects are computed using the Realizable k-ε model, which means that the model satisfies certain mathematical constraints on the Reynolds stresses, consistent with the physics of turbulence flow.

Whether a flow is laminar or turbulent, depends upon the relative friction (i.e. effective viscosity) and inertia. In laminar flows, the ratio of inertia to viscous forces (Reynolds number) is low such that disturbances are damped out by the fluid viscosity and the fluid particles follow the streamlines exactly, whereas turbulent flow will always occur for sufficiently high ratio regardless of the geometry of the flow under consideration. The equations governing a turbulent flow are precisely the same as for laminar flow; however, the solution is clearly much more complicated in this regime. The approaches to solving the flow equations for a turbulent flow field can be divided into two classes. Direct Numerical Simulations (DNS) use the speed of modern computers to numerically integrate the Navier-Stokes equations, resolving all of the spatial and temporal fluctuations [1]. In essence, the solution procedure is the same as for laminar flow, except that the numerical technique must contend with resolving all of the fluctuations in the velocity and pressure. DNS remains limited to very simple geometries and is extremely expensive to run. The alternative to DNS, found in most CDF packages, is to solve the Reynolds Averaged Navier-Stokes equations (RANS), which govern the mean velocity and pressure. Because these quantities vary smoothly in space and time, they are much easier to solve, however, they require additional assumptions to close the set of equations and care must be taken in applying them as these assumptions can be introduce significant error into the calculations.

3.2.2   Discrete phase

The discrete phase refers to the flow of the paint droplets. The droplets are charged with the same polarity as the spray gun and are pushed by the electrostatic force toward the grounded target. In addition to the electrostatic force, a strong airflow coaxial with the spray gun, known as the "shaping air", helps to transport the droplets to the target surface. The interaction of these forces determines the path that the droplets will follow and ultimately the location of their deposition. ANSYS predicts the trajectory of the discrete phase by integrating the force balance on the particle, which is described in a Lagrangian reference frame. The force balance based on Newton's law equates the particle inertia with the forces acting on the particle, including the gravitational, electrostatic and drag forces

$$m\frac{\partial \mathbf{u_p}}{\partial t} = \frac{\eta \pi r\, Re\, C_d}{4C_c}\left(\mathbf{u} - \mathbf{u_p}\right) + q\boldsymbol{E} + m\boldsymbol{g} \tag{3.4}$$

where $\mathbf{u_p}$ is the particle velocity, m is the particle mass, η is the dynamic viscosity, $\boldsymbol{E}$ is the electric field, and Re is the Reynolds number for the particle which is defined as

$$Re = \frac{\rho_0(\mathbf{u}-\mathbf{u_p})D}{\eta} \tag{3.5}$$

where D is the particle diameter and ρ_0 is the particle density. The parameter C_d is the non-Stokesian drag coefficient and can be calculated as

$$C_d = k_1 + \frac{k_2}{Re} + \frac{k_3}{Re^2} \tag{3.6}$$

where k_1, k_2 and k_3 are constants that apply to smooth spherical particles over several ranges of Re, which have been given in [2]. For example, at very small Reynolds number ($Re \approx 0.1$), the flow is known as Stokes flow and under these conditions $C_d = \frac{24}{Re}$. At very high Reynolds number ($Re \approx 10^3$), the value of C_d becomes approximately constant at about 0.4, but in the intermediate range of Re, which is the range of practical interest, C_d varies with Re in a complicated manner. The Cunningham correction factor to Stokes drag law, C_c depends on the droplet diameter and the mea free path of the molecules and is expressed as [3]

$$C_c = 1 + \frac{2\lambda}{D}\left(1.257 + 0.4e^{-\frac{0.55D}{\lambda}}\right) \tag{3.7}$$

where λ is the molecular mean free path. For $D > 100$ μm, C_c is very close to unity and when $D \approx 15$ μm, C_c is close to 2.

The trajectories of the particles are very complex. Dispersion of particles due to turbulent fluctuations in the flow can be modeled using either one of two different approaches: the discrete random walk and the cloud tracking method. The discrete random walk has been used in the numerical simulations of this study. In this method, each injection is tracked repeatedly in order to generate a statistically meaningful sample. The mass flow rate and exchange source terms for each injection are divided equally among the multiple stochastic tracks. Turbulent eddies of many sizes are superimposed onto the mean flow and create fluctuations in the velocity, which is decomposed into mean and turbulent components

$$\mathbf{u}(t) = \mathbf{u}_{\text{avg}} + \mathbf{u}'(t) \tag{3.8}$$

where $\mathbf{u}_{\text{avg}}$ is the average velocity that can be evaluated through the integration over the time interval from t_0 to $t_0 + T$ as

$$\mathbf{u}_{\text{avg}} = \frac{1}{T}\int_{t_0}^{t_0+T}\mathbf{u}(t)dt \tag{3.9}$$

then from Eq.(3.8), the turbulent component can be estimated as

$$\mathbf{u}'(t) = \mathbf{u}(t) - \mathbf{u}_{\text{avg}} \tag{3.10}$$

If the flow is steady and laminar, then $\mathbf{u}_{\text{avg}} = \mathbf{u}(t)$ for all time. Because the turbulent motion associated with eddies is approximately random, it can be characterized using statistical concepts.

3.2.3   Electric field

The calculation of the electrostatic forces, which strongly affect the motion of the injected particles, requires solving the electric field generated by the voltage applied to the bell cup and the space charge formed by the charged particles, which is governed by Poisson's equation

$$\nabla^2\phi = -\frac{\rho}{\varepsilon} \tag{3.11}$$

where ϕ is the electric potential, ρ is the total space charge density and ε is the permittivity of the medium. Then, the electric field can be determined by taking the gradient of the electric potential

$$\boldsymbol{E} = -\nabla\phi \tag{3.12}$$

The electric force per unit mass, $\boldsymbol{F}$, on the particle can be expressed as

$$\boldsymbol{F_E} = \frac{q}{m}\boldsymbol{E} \tag{3.13}$$

where q is the charge and m is the mass of an individual particle. As long as the boundary conditions are defined, the Poisson's equation can be solved by using the User Defined Scalar transport equations (UDS) in ANSYS [1]. The drifting charged particles create an electric current density given by

$$J = \rho\mu E + \rho v - D_f \nabla\rho \qquad (3.14)$$

where μ is the particle mobility, v is the total velocity of particles and D_f is the diffusion coefficient. Under the steady state condition, the charge conservation law must be satisfied

$$\nabla \cdot J = 0 \qquad (3.15)$$

3.3   Description of the numerical model

A full 3D numerical model was created using ANSYS, which includes all the relevant mechanical and electrical phenomena. The mechanical phenomena include the shaping air, the motion of polydispersed particles and the motion of the coating target, while the electrical phenomena include the particle space charge, corona discharge and the electrohydrodynamic flow effects. The discrete phase is superimposed on the continuous phase. Coupling between both phases is included via source terms of mass and momentum. The main elements of this model are the gun, the atomized particles, and the target to be coated. The gun model is a cylinder of 46 cm length and 10 cm diameter. The liquid paint used in this model is supplied to the gun's cup, which is typically has a radius of 30 mm, as shown in Figure 3.1a. In practical application, this cup rotates at high speed of 5000 to 45000 rpm, resulting in creation of ligaments that are pushed towards the edge of the cup and droplets eventually ejected in the radial direction. The particles are injected from individual points uniformly distributed along the edge of the atomizer.

All the particles that are injected from the same injection point and that have the same radius, initial velocity, density and flow rate constitute one so-called "super-particle". These particles are not existed in real life, but they are assumed from the numerical analysis point of view. ANSYS traces every super-particle from the injection point until it either hits the target or escapes the computational domain and all the particles within one super-particle are assumed to have the same trajectory. It is clear that the total number of super-

particles is extremely important since the mass deposited is equal to the mass of an individual particle times the number of particles in the super-particle.
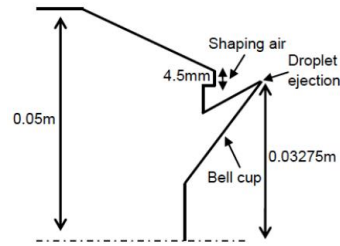
(a) Gun model
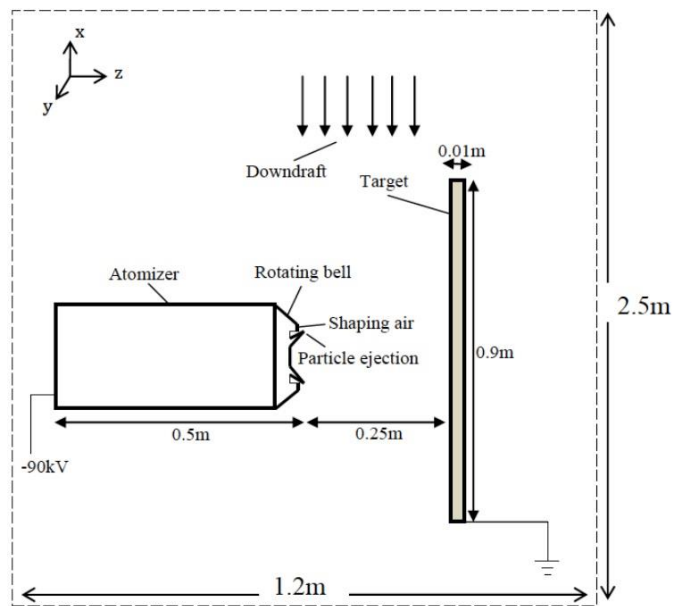
(b) Computational domain

Figure 3.1: Geometry of the electrostatic painting numerical model

The computational domain consists of a cubic cell of 2.5 m in width, 2.5 m in height and 1.2 m in length, as shown in Figure 3.1b. Some factors, such as the shaping air mass flow rate, the gun voltage, the size and shape of the target, the distance between the gun and the target, the size and velocity of the injected particles, have to be considered in the model since they have an important effect on the solution. These factors can be varied amongst many different cases.

The shaping air around the cup is supplied through an annulus of small holes inside and flows out of a ring shaped slit of 4.5 mm in width. The shaping air assists in creation of the droplets and their separation from the gun, and it focuses the particle trajectories. Downdraft air is introduced to control the environmental conditions, but its effect was sometimes neglected in the numerical model. A voltage source of 90 kV is applied to the rotating cup, which provides conduction charging for the injected droplets. Also, the target geometry is a square plate of 90 cm side and thickness of 1 cm. It is positioned so that its center lies directly to the atomizer centerline (Figure 3.1b).

3.4   Discretization of the numerical model

The geometry of the computational domain was created using the ICEM package [1] and meshed in an unstructured manner. The total number of cells used for meshing is around 600,000 cells, where all the volume cells are tetrahedral and all the surface cells or faces are triangular. The mesh is refined in the cone-shaped area between the gun and the target and it is sparser elsewhere. This produces a suitable compromise for the accuracy of modeling results in the region of interest and a relatively small size of the entire mesh. A cross-section of the mesh is shown in Figure 3.2b.

3.5   Simulation results

This section discusses the simulation results of some of the different cases studied, assuming that the target was stationary and the injection spray pattern consists of mono-size particles. The distribution of airflow in the turbulent model has been examined first and shown in Figure 3.3. It has been found that there is a lack of uniformity for the shaping air velocity distribution, when the results have been obtained across a series of planes perpendicular to the axis of the spray gun. The contours of the air velocity are more non-uniform in the space close to the shaping air inlet, whereas it seems to be more uniform at larger distances. Therefore, it is expected to have a non-uniform injection pattern once the particles leave the tip of the spray gun. In these simulations, the mass flow input was 700 slpm that is equivalent to 12.5 m/s maximum velocity magnitude.
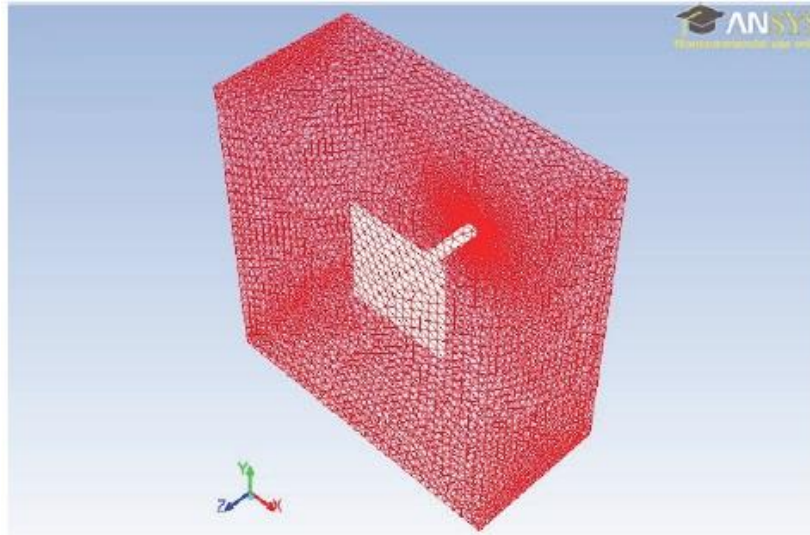
(a) Computational domain
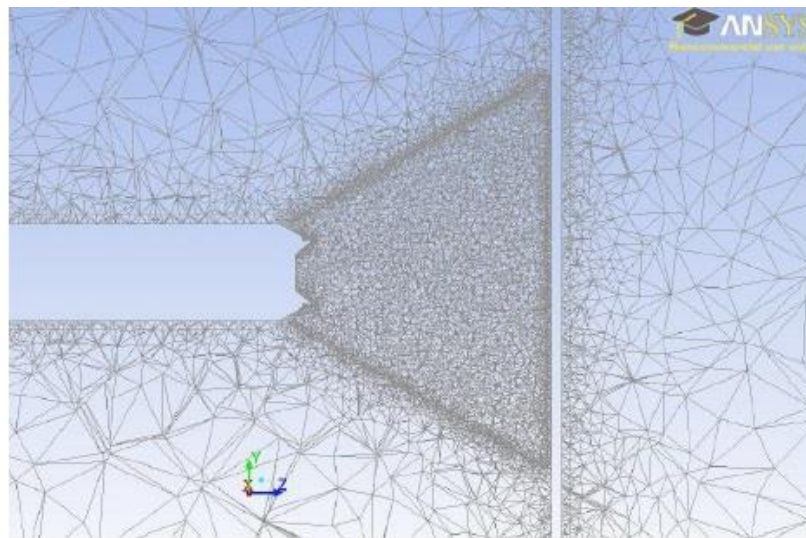
(b) Space between the gun and the target

Figure 3.2: Meshing of the numerical model
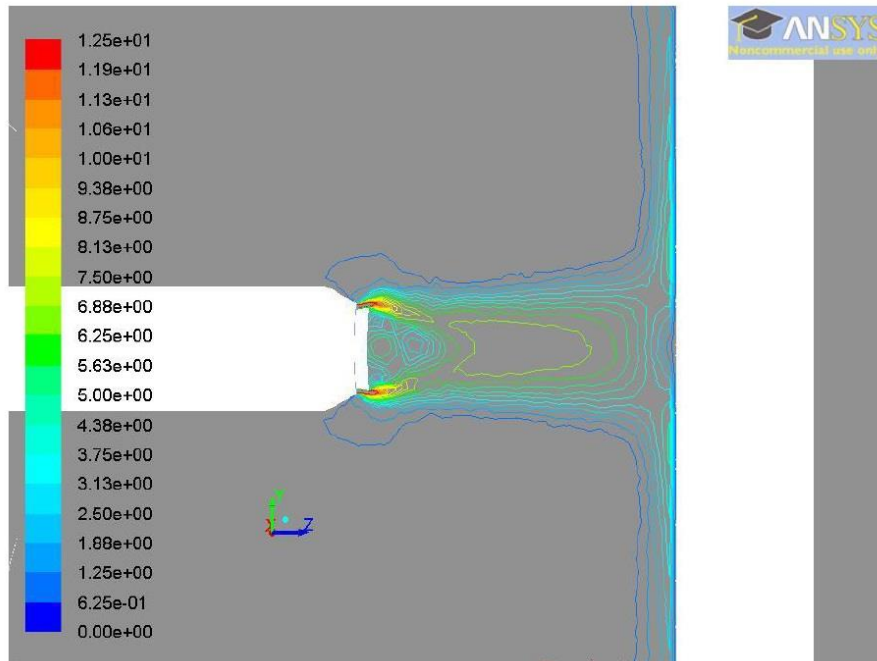
(a) Plane parallel to the axis of the spray gun
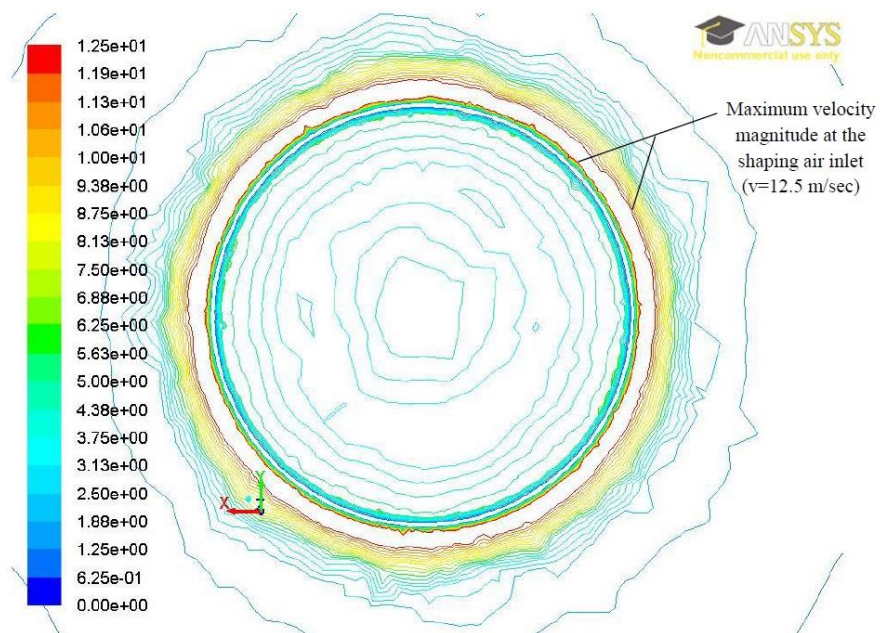
(b) Perpendicular plane at z=0
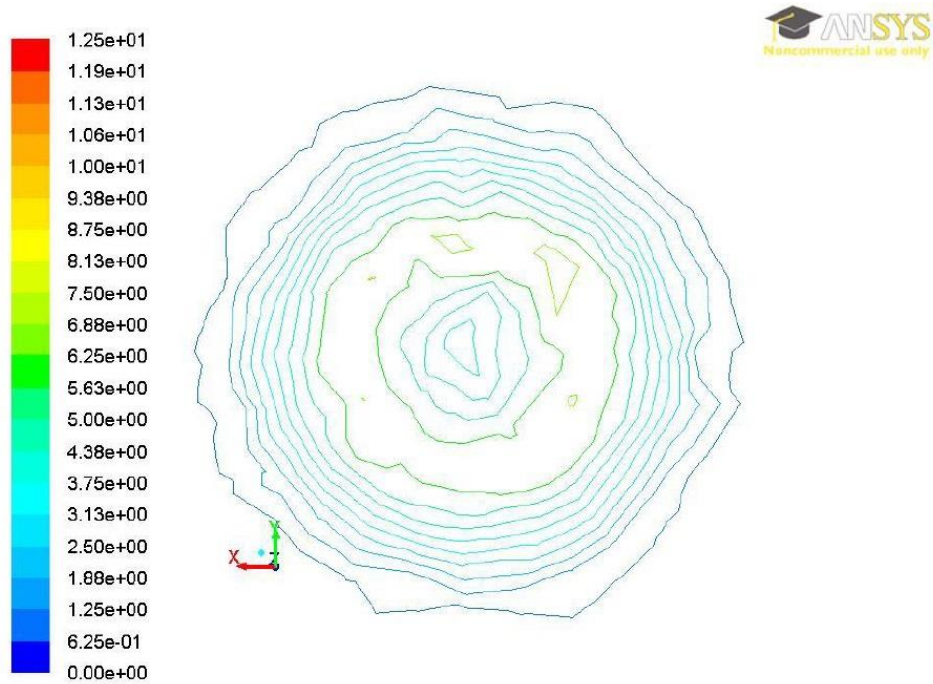
(c) Perpendicular plane at z=5 cm
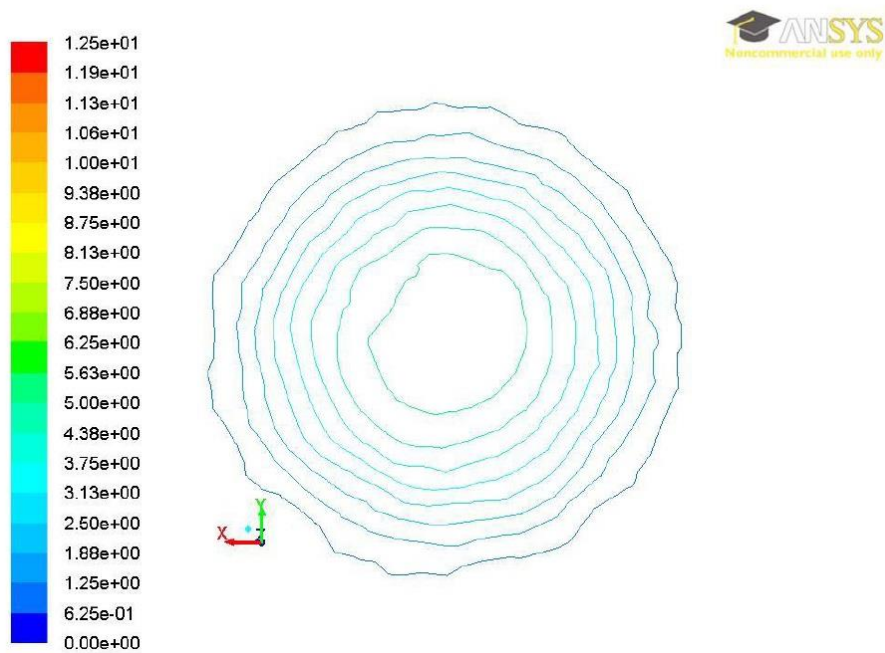
(d) Perpendicular plane at z=25 cm

Figure 3.3: Contours of air velocity magnitude

In most of the previous studies of this project [4,5] considerable work has been carried out to clarify the importance of the injection parameters (i.e. number of injection points, total number of super-particles, etc.),but there was a problem with having insufficient coverage at the central part inside the cone of the spray pattern. Their results of injecting polydiseprsed particles showed that the deposition thickness is a "ring-shaped" pattern, where the thickness decreases gradually from the ring to the edge of the target and also decreases sharply from the ring to the center of the target, and therefore, there was no deposition at the central part of the target surface.

The results of this previous numerical model were post-processed in order to take into account the de-rating factor to account the loss of mass due to solvent evaporation. Also, the surface spreading due to liquid flow on the surface was introduced through smoothing and filtering functions available in MATLAB, such that these functions utilize the moving window algorithm in order to calculate average values of $k \times k$ neighboring points in the 2D space of the raw input data. The numerical results showed a good match for the maximum values of thickness with the experimental results assuming $k=5$, but the experimental thickness values were higher at the central part of the target than the predicted numerical ones, as shown in Figure 3.4, which also contains the plots with 1D smoothing parameter k (1d) taking values 10, 20 and 40. In this case, the numerical results revealed that the deposition thickness at the center is improved and the peak thickness decreases, as the parameter k is increased.

Therefore, in order to determine the effect of surface perturbations on the coating thickness, it was important to modify this model to inject particles more uniformly. A series of injection angles θ was introduced, such that these angles can be determined by the spacing between the spray gun and the target, and the position at which the injected particles will hit the target (Figure 6.3 of Chapter 6).

The angles were also selected to cover the range of distance from the center of the target to 30 cm away and such that the velocity magnitude of all injected particles is kept constant in the direction of θ. Each injected particle was assigned a certain fraction of the total mass flow rate.
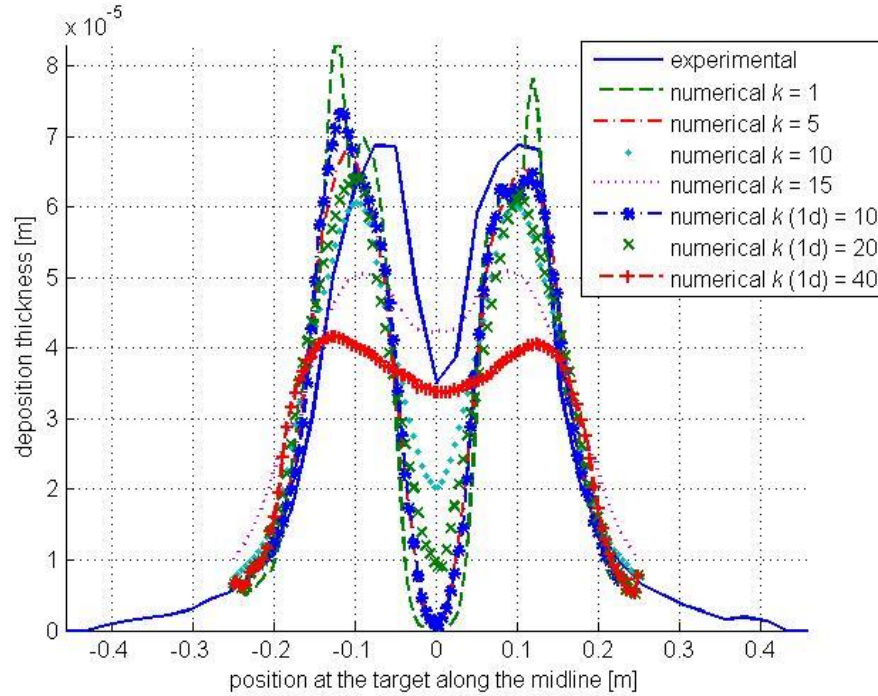
Figure 3.4: Comparison of the deposition thicknesses at the target along the midline with de-rating factor of 0.45 and coating time of 7 s [5]

The total number of injection angles plays a role in the total number of super-particles that has been traced in the model

$$N = N_1 \times N_2 \times N_3 \tag{3.16}$$

where N is the total number of injected super-particles, N_1 is the total number of injection points, N_2 is the number of size bands and N_3 is the total number of injection angles used in the spray model.

Many cases were simulated assuming different injection patterns. The injection pattern in each case includes fixed injection angles and corresponding fractions of the total mass flow rate. Study on these cases was conducted using the monodipersed charged particles of diameter 35 μm with velocity magnitude of 40 m/s in the direction of θ and charge-to-mass ratio equal -1 mC/kg. The numerical results in each case were compared with the experimental ones. Table 3.1 shows the injection pattern for five cases, assuming seven different injection angles.

Table 3.1: Injection pattern for five different cases

Injection angles	Mass flow (%)				
(degrees)	Case#1	Case#2	Case#3	Case#4	Case#5
-7.5	10%	9%	14%	5%	8%
0	10%	8%	15%	4%	7%
5	20%	10%	13%	3%	6%
10	25%	25%	25%	2%	5%
15	20%	20%	20%	5%	10%
25	10%	10%	10%	50%	50%
35	5%	18%	3%	31%	14%

The injection angles were fixed and the mass percentages were varied for all cases. For the first three cases the injections at angles of 10, 15 and 25 degrees were chosen to be unchanged, whereas the injection mass for the last two cases were varied such that the percentages decrease gradually from -7.5 to 10 degrees and increase for larger angles (more than 15 degrees). The numerical results show a higher deposition thickness at the central part of the target surface for increased mass fractions at small angles (-7.5, 0 and 5 degrees) of cases#1, 2, 3 and 5, whereas the deposition thickness at the center for case#4 is less due to the lower mass injection at these angles. Also, the increased mass injection of particles at larger angles increases the thickness at the edges and makes the deposition profile more uniform (cases#2 and 5), as shown in Figure 3.5. An increase of the mass fractions at small angles (cases#1 and 3) or larger angles (case#4) will affect the deposition at the center and also the uniformity of the deposition pattern. Therefore, the appropriate selection of the mass percentages of the spray injection pattern is very important to compromise between the deposition at the center and uniform paint thickness. The transfer efficiency (TE) is calculated as the ratio of the total number of deposited particles to the total number of injected particles from the spray gun. It was found that TE is 93%, 90%, 90%, 85% and 90% for cases 1, 2, 3, 4 and 5, respectively.

In order to increase the width of the distribution by injecting more mass, four more cases were performed in which new injection angles at 20, 30 and 45 degrees were added to the

previous pattern. Table 3.2 shows the injection pattern for these cases. To increase the injection at larger angles, an angle of 45 degrees was added to these four cases and two angles of 30 and 20 degrees were added to the last two cases. The injections at small angles were set to not exceed 5%, while the injections were increased at larger angles. The numerical results of cases#6 and 8 show a higher deposition thickness at the edges than cases# 7 and 9 due to the increased mass injection at larger angles, as shown in Figure 3.6. Also, the deposition pattern of case#8 is more symmetric than in case#6. It was noticed the distance between the peaks slightly decreases in these cases due to the increased width of the deposited particle distribution. For cases 6, 7, 8 and 9 the transfer efficiency is 95%, 90%, 85% and 90%, respectively. The contours of accumulation rate for some cases are illustrated in Figure 3.7.
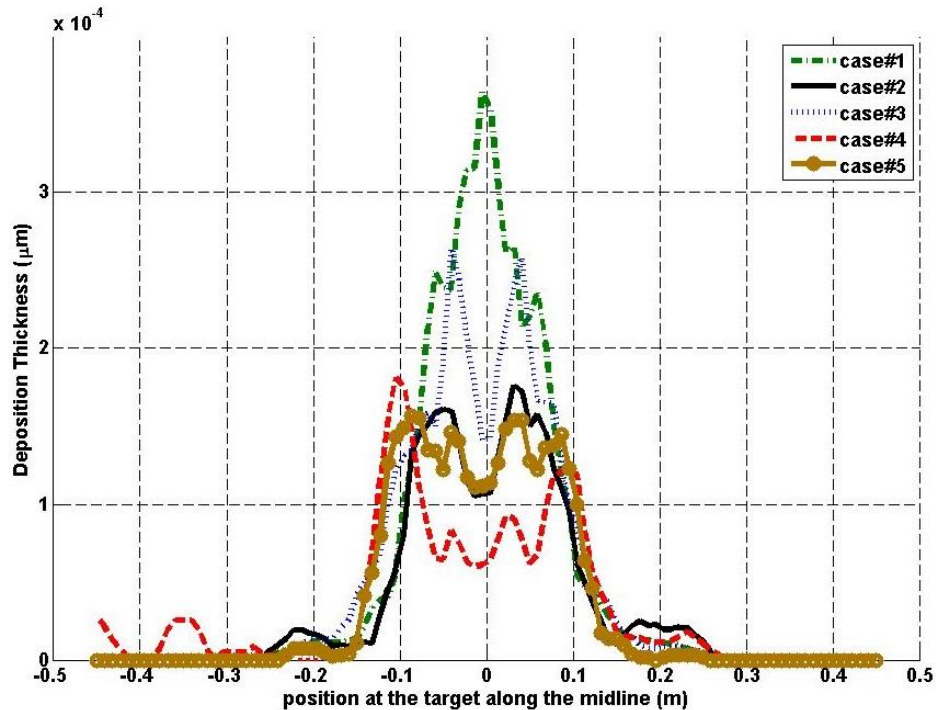
Figure 3.5: Comparison between the numerical results of the particle deposition thickness for different cases with de-rating factor of 0.35 and coating time of 7 s

Table 3.2: Injection pattern for more four different cases

Injection angles (degrees)	Mass flow (%)			
	Case#6	Case#7	Case#8	Case#9
-7.5	4%	3%	3%	4%
0	4%	2%	3%	4%
5	4%	4%	3%	4%
10	4%	9%	4%	4%
15	4%	10%	4%	4%
20	0%	0%	0%	10%
25	30%	30%	25%	15%
30	0%	0%	23%	15%
35	30%	25%	25%	25%
45	20%	17%	10%	15%
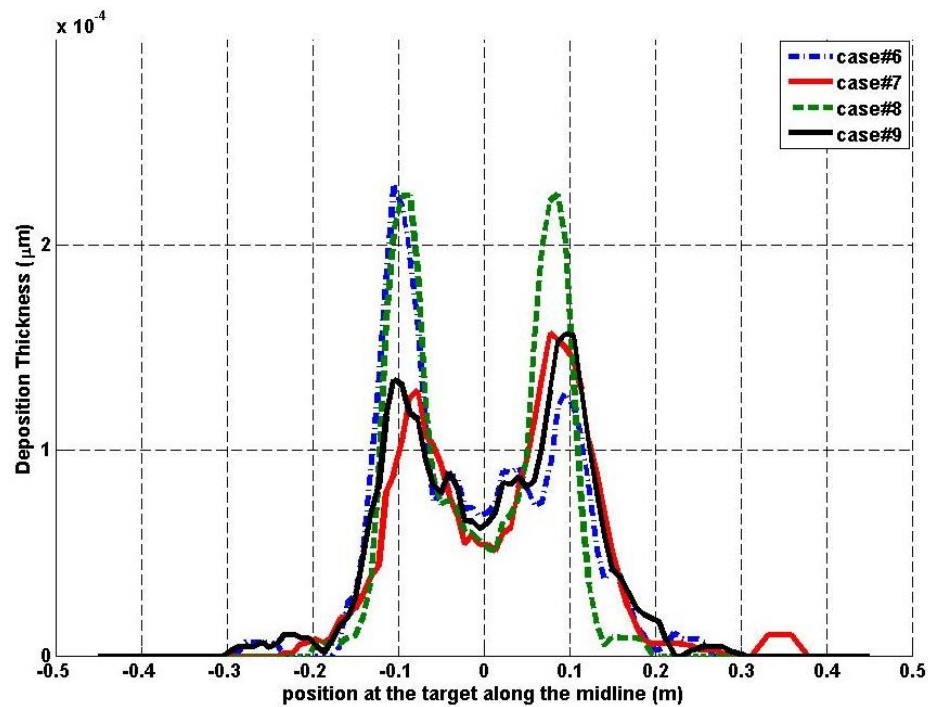
Figure 3.6: Comparison between the numerical results of the particle deposition thickness for additional cases with de-rating factor of 0.35 and coating time of 7 s
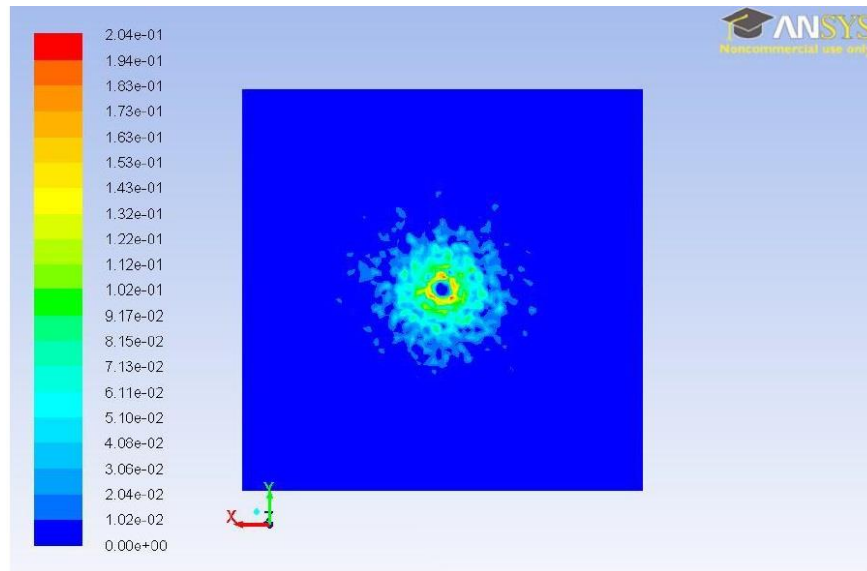
(a) Case#3
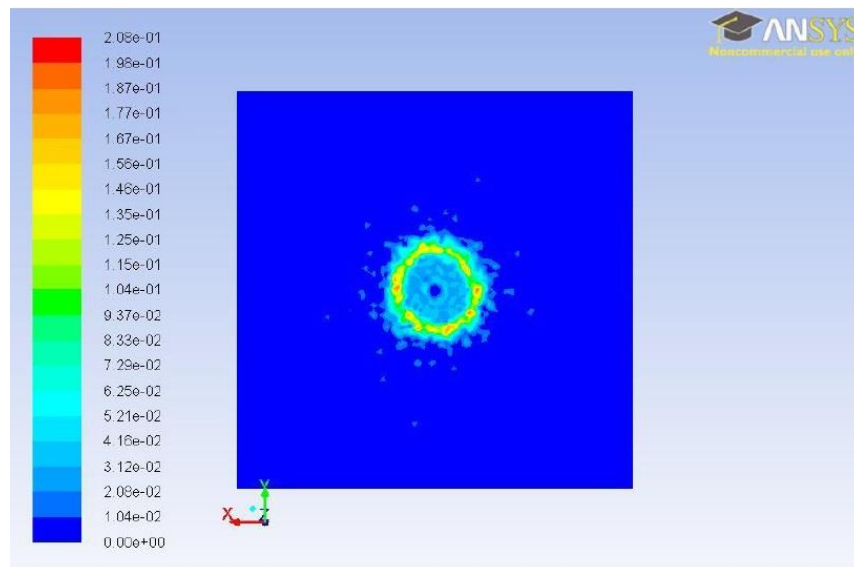
(b) Case#8

Figure 3.7: Contours of accumulation rate on the target (kg/m^{2}s)

3.6 Conclusions

A full 3D model was presented in this chapter to predict the particle deposition profile in the electrostatic coating process on a planar target. Many different cases were studied, where the spray injection pattern was modified for monodispersed particles by introducing

injection angles with selected fractions of the total mass flow rate at each injection point. The simulation results were obtained for each case and a comparison with the experimental results is needed to validate the accuracy of the numerical model. However, a full understanding of the injection angle and fractional mass flow rate on the particle injection is not yet complete. The accurate prediction of an optimum injection pattern to attain a good agreement with the experimental thickness profile is very complicated. The reason may be due to many factors. The impossibility of having a good numerical model to simulate the spray injection pattern and the effect of the turbulent flow characterized by chaotic changes are the most fundamental ones.

The concentration of the monodispersed particles seems to be high and localized at the edge of the circular ring pattern. Therefore, the cases of injecting polydispersed particles need to be examined, where the total number of injected super-particles is larger. The distribution of charge-to-mass ratios is assumed to be reciprocal to their diameters, as predicted theoretically, since experimental data is not available at present. It is assumed that all the droplets have the same surface charge density, i.e. charge-to-mass ratio is reciprocal to their diameter, and that the 35 μm droplet has a q/m of 1 mC/kg. Chapter 6 continues this investigation by modifying the injection pattern of the spray gun for the cases of polydispersed particles assuming a stationary target and a target moving in one and two directions. The techniques developed in Chapter 6 were used in the subsequent work described in Chapter 7 involving the coating of targets having surface perturbation.

References

[1] ANSYS FLUENT User's guide, www.ansys.com

[2] S.A. Morsi, A.J. Alexander, "An investigation of particle trajectories in two-phase flow systems," J. Fluid Mech., vol.55, No.2, pp.193-208, 1972.

[3] E. Cunningham, "On the velocity of steady fall of spherical particles through fluid medium," Proc. R. Soc. Lond. A., Math. Phys. Sci., vol.83A, pp.357-365, 1910.

[4] N. Toljic, G.S.P. Castle, K. Adamiak, C.T. Fan, J. Simmer, "Studies on the deposition profile uniformity for the full 3D numerical model of the electrostatic coating process," UWO internal report#8 to GM, August 29, 2012.

[5] N. Toljic, G.S.P. Castle, K. Adamiak, C.T. Fan, J. Simmer, "Comparison between the experimental and numerical results for the 3D model of the electrostatic coating process," UWO internal report#9 to GM, December 5, 2012.

Chapter 4

The Charge Level of a Ligament-Droplet system Atomized in a Uniform Electric Field[†]

4.1 Introduction

Electrospraying systems are widely used in many practical applications, such as electrostatic painting, crop spraying and pharmaceutical processing, as reviewed by Bailey [2]. These systems utilize an electric field to electrically charge the ejected droplets as they exit the spray nozzle and attract them to a grounded substrate. This may lead to an increase in the transfer efficiency to more than 80%. The charging level or, more specifically, the charge-to-mass ratio on a liquid droplet is a critical parameter that needs to be determined in order to accurately predict the behavior of the droplet in such applications and is considered to be the most important parameter that affects the spraying characteristics. The charge magnitude can be potentially affected by various factors such as the droplet radius, ligament radius, droplet shape, electric field intensity, space charge, the presence of adjacent ligaments and previously formed droplets. The process of disintegration of a liquid jet into a stream of discrete droplets in a uniform electric field has been studied theoretically and experimentally for many years. Macky [3] studied the behavior of water drops in a strong electric field. He observed that drops become elongated and unstable with increasing the electric field. Schneider et al. [4] presented a mathematical analysis to calculate the radius, velocity and spacing of droplets ejected from the end of an unstable electrified jet in terms of the jet radius, velocity and surface tension. Large collection of experimental measurements of both droplet size and charge generated after breakup has been performed by [5]. However, very little work has been done on exploring the charge to radius dependency over the surface of liquid droplets produced by the disintegration of a charged jet [6,7].

[†] This work has been accepted for publication [1].

The dynamic modeling of the liquid ligament to determine the droplet shape on disintegration has been investigated in several studies. Shiryaeva et al. [8] analyzed the stability of an electrified cylindrical jet using different values of dielectric permittivity. Lee et al. [9] made a study on the droplet ejection from an electrohydrodynamic (EHD) inkjet nozzle considering factors of the liquid conductivity and surface tension. Domnick at al. [10] succeeded to create a 3D numerical model to simulate the electrostatic spray painting system using a high speed rotary bell with external charging by means of Computational Fluid Dynamic (CFD).

Reznik et al. [11] discussed numerical and experimental results for the droplet evolution and jet formation in a strong electric field. They distinguished between three different jetting characteristics: subcritical electric field, supercritical electric field with contact angle less than 0.8π and greater than 0.8π in electrospinning of nanofibers. Bending instabilities of an electrospun fluid was analyzed and explained mathematically by [12] and [13]. Their results showed that the jet bent into a complex path and a lateral perturbation occurred in response to the repulsive forces between adjacent elements of charge carried by the jet.

Ambravaneswaran et al. [14] investigated the mechanical formation of drops of Newtonian liquids from a vertical capillary into air using a 2D axisymmetric system solving Navier–Stokes equations using the Finite Element Method. They also compared the accuracy of their results over a large range of parameters with previously reported data based on a 1D algorithm. Jaworek et al. [15] tested experimentally three different multi-nozzle hydrodynamic spray systems and they measured the size and charge distributions of the droplets for these systems. For all spray systems that tested, in the entire voltage range in which the precession mode is generated, the size of droplets was only slightly dependent on voltage. Hartman et al. [16] investigated the jet break-up mechanism with a high-resolution camera. They found that the jet break-up mechanism depends on the ratio of the electric normal stress over the surface tension stress. A threshold value of the stress ratio on the jet has been found above which the jet starts to whip. It was shown by Zhakin and Belov [17] that the behavior of charged jets is governed by the conduction of the liquid, viscosity, and surface tension. Also, the experimental data on the forms and electrical

characteristics of jets of water, ethanol, glycerol, and castor oil depending on the applied voltage have been reported.

4.2 Mathematical model

The first part of this study includes a stationary ligament-droplet system in a 2D axisymmetric domain. It was assumed that there is no space charge in the region between the high voltage and grounded electrodes. Therefore, the scalar electric potential in air is governed the second order PDE Laplace's equation

$$\nabla^2 \phi = 0 \tag{4.1}$$

where ϕ is the scalar electric potential.

The droplet fluid is assumed to be ideally conducting, so the droplet surface is equipotential at the voltage level identical to that supplied to the electrode. The electric field vector can be determined by calculating the gradient of the electric potential

$$\boldsymbol{E} = -\nabla\phi \tag{4.2}$$

Then, the magnitude of charge can be calculated by integrating the surface charge density over the droplet surface.

$$q = \iint \varepsilon_0 E_n \, dS \tag{4.3}$$

In order to understand the dynamics of droplet deformation in a strong electric field, it is necessary to solve the Navier-Stokes equations as well as track the interfaces between both fluids. The laminar two-phase flow system was coupled with the applied electric field and electric charges on the interface. Additional body forces were added to the Navier-Stokes equations for considering the surface tension ($\boldsymbol{F}_{st}$) and electric stress ($\boldsymbol{F}_{es}$). The hydrodynamic part of the problem is described by the Navier-Stokes equations and continuity equation

$$\rho_f \frac{\partial \mathbf{u}}{\partial t} + \rho_f (\mathbf{u} \cdot \nabla)\mathbf{u} = \nabla \cdot \left[-P\mathbf{I} + \eta(\nabla\mathbf{u} + (\nabla\mathbf{u})^{\mathrm{T}}) \right] + \boldsymbol{F}_{st} + \boldsymbol{F}_{es} \tag{4.4}$$

$$\nabla \cdot \mathbf{u} = 0 \tag{4.5}$$

where $\mathbf{u}$ is the fluid vector velocity, ρ_f is the fluid density, P is the pressure, $\mathbf{I}$ is the identity vector matrix and η is the dynamic viscosity. No slip-boundary conditions were applied to the electrodes and pressure outlet conditions were applied to other boundaries.

To describe the evolution of the droplet shape, the level set method was applied. In this method, the physical property changes smoothly from the value on one side of the interface to the value on the other side in the interfacial transitional zone. The method shows the evolution of the interface between the two fluids tracing an iso-potential curve of the level set function ($\emptyset$). In general, in the droplet ($\emptyset = 1$) and in ambient fluid ($\emptyset = 0$). The interface is represented by the 0.5 contour of the level set function ($\emptyset = 0.5$). The time evolution of the interface is modeled via transport of the level set function ($\emptyset$) due to the underlying physical velocity field.

$$\frac{\partial \emptyset}{\partial t} + \mathbf{u} \cdot \nabla \emptyset = \alpha \nabla \cdot \left(\epsilon_{ls} \nabla \emptyset - \emptyset (1 - \emptyset) \frac{\nabla \emptyset}{|\nabla \emptyset|} \right) \tag{4.6}$$

where ϵ_{ls} is the parameter controlling the interface thickness, which is in the same order as the mesh size, and α is the re-initialization parameter, where the maximum velocity magnitude in the model is a suitable value for it. The surface tension force is given by

$$\boldsymbol{F}_{st} = \nabla \cdot \left[\gamma \left(\mathbf{I} - \left(\frac{\nabla \emptyset}{|\nabla \emptyset|} \right) \left(\frac{\nabla \emptyset}{|\nabla \emptyset|} \right)^{\mathrm{T}} \right) \delta \right] \tag{4.7}$$

where γ is the surface tension coefficient and δ is the Dirac delta function, which is nonzero only at the interface and can be approximated by

$$\delta = 6|\emptyset(1 - \emptyset)||\nabla \emptyset| \tag{4.8}$$

The electric stress forces cause deformation and can be calculated from the electric field distribution, which depends on the position and shape of the droplet. Assuming that the fluid is incompressible and the effect of the magnetic field is neglected, the electric stress force can be determined by taking the divergence of the Maxwell stress tensor, which couples electrostatic and hydrodynamic phenomena such that

$$F_{es} = \nabla \cdot \mathbf{T} \tag{4.9}$$

$$T_{ij} = \varepsilon E_i E_j - \frac{1}{2}(\varepsilon E^2)\delta_{ij} \tag{4.10}$$

where δ_{ij} is the Kronecker delta function. The conductivity and permittivity are constant, but different, for each fluid. In order to have all physical properties in the interface, the two phase relative permittivity (ε_r) and conductivity (σ_r) can be define based on the volume fraction of the phases

$$\varepsilon_r = \varepsilon_{in}Vf_{in} + \varepsilon_{ex}Vf_{ex} \tag{4.11}$$

$$\sigma_r = \sigma_{in}Vf_{in} + \sigma_{ex}Vf_{ex} \tag{4.12}$$

where Vf_{in} and Vf_{ex} are the volume fractions of the droplet and the continuous phase, respectively. By using these equations, the physical properties change smoothly from the value on one side to the value on the other side.

4.3   Static model

To investigate the relation between the charge magnitude over a single droplet and the ligament length and width, a stationary base case has been created with a 2D axisymmetric model, which encompasses a high voltage electrode, grounded electrode, a ligament and an ejected droplet, which are assumed to be highly conductive. The droplet is assumed to be spherical in shape and it is directly connected to the ligament by a very small neck, as shown in Figure 4.1.

The mathematical model for this part involves Eqs.(4.1)-(4.3), as shown in Section 4.2. All numerical simulations were performed using the COMSOL, a Finite Element commercial software. A very fine mesh was implemented in the area near the ligament tip and much coarser elsewhere. A series of simulations were performed, where the radius of the droplet was varied as 7.5, 15, 30 and 45 μm and the ligament length in a range between 0 and 4 mm. The radius of the droplet was assumed to be equal to the radius of the ligament. Table 4.1 illustrates the values of the designed parameters for the numerical model.

Table 4.1: The designed parameters for the base case model

Model parameter	Numerical value
droplet radius	7.5, 15, 30 and 45 μm
ratio of droplet and ligament radii	1
applied voltage	90 kV
ligament length	0 - 4 mm
distance between electrodes	25 cm
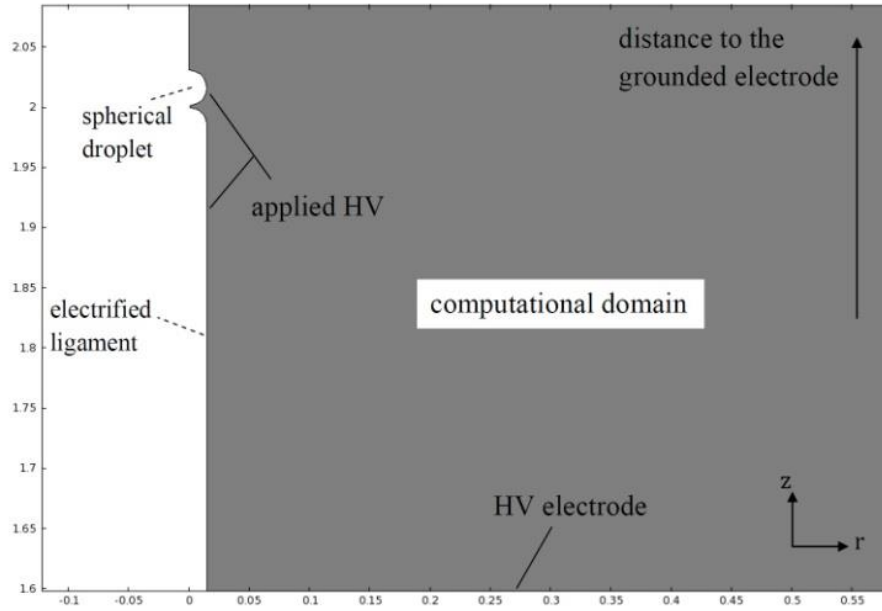
Figure 4.1: Close-up view of the droplet and ligament in 2D axisymmetric model

4.4 Discussion and results

4.4.1 Estimation of charging level and radius exponent

Félici [18] calculated the charge over a conductive spherical particle of radius (r), which is in direct contact with the surface of a high voltage electrode, i.e. the ligament length is zero. He predicted a mathematical formula in the form

$$q = 6.56\pi\varepsilon_0 E_0 r^2 \tag{4.13}$$

where ε_0 is the dielectric permittivity of free space, and E_0 is the external electric field. Obviously, since all the charge resides on the surface, the particle charge is directly

proportional to the square of its radius. This can be considered as the base case to compare the numerical model as the length of the ligament is increased. The simulation results have been obtained and plotted for the droplet charge versus the normalized ligament length, i.e. the ligament length divided by the droplet radius, as shown in Figure 4.2. These results demonstrate that the charging level increases monotonically as the ligament length increases. Also, an increase in the droplet radius at a fixed ligament length results in a larger droplet charge. In a general case, the magnitude of the droplet charge can be expressed in terms of the ligament length and the droplet radius as

$$q = A(L, r)r^2 \tag{4.14}$$

where A is an empirical coefficient denotes to the charge magnitude in C/m^2 and L is the ligament length. Based upon these results, a mathematical approximation was determined to predict the values of the charge magnitude coefficient A for different normalized ligament lengths as

$$A \cong 65 \times 10^{-6} \left[0.53 \left(\frac{L}{r} \right)^{0.9} + 1 \right] \tag{4.15}$$

It was confirmed that for $L=0$, where the droplet is in direct contact with the surface of the atomizer, the value of $A=65$ μC/m^2 and the radius exponent is equal 2, which is in a good agreement with Félici's predicted value. It was found that although the charge remains a surface phenomenon, the effective value of the radius exponent decreases dramatically and approaches 1.1, as the ligament length increases significantly and becomes much greater than the droplet radius. The charge magnitude was estimated numerically from Eqs.(4.14) and (4.15) for four different droplet sizes and compared with the simulation results, as shown in Figure 4.2. The approximation error was found to not exceed 5%.

4.4.2   The effect of the ligament radius

To examine the effects of the ligament radius (r_{lig}) on the level of charging, six different cases were investigated, as depicted in Figure 4.3, where the ratio of droplet and ligament radii was varied as 0.5, 0.8, 1, 1.5, 2 and 10 and the droplet radius was assumed to equal 15 μm. It was found that the level of droplet charge increases significantly as the ratio of

droplet and ligament radii increases, as shown in Figure 4.4.
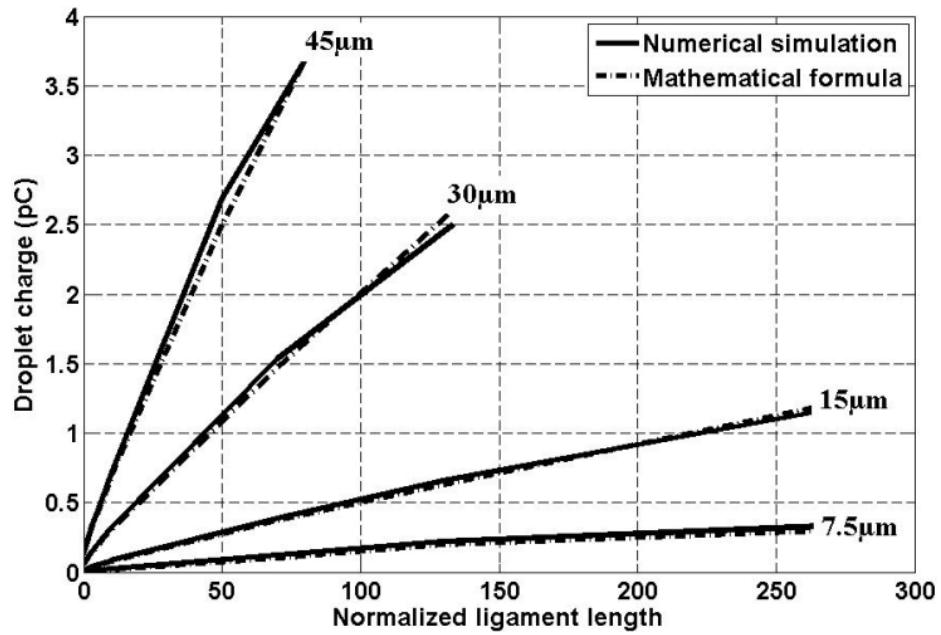
Figure 4.2: The droplet charge versus the normalized ligament length for four different droplet sizes; numerical results and mathematical formula
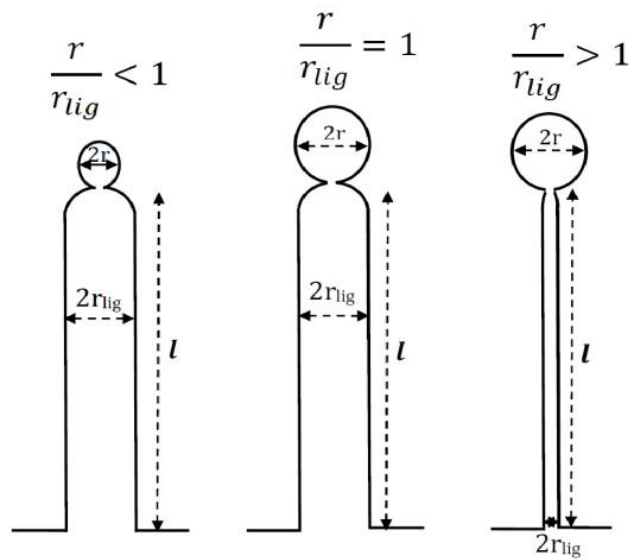
Figure 4.3: Configurations of droplet formation with different ligament radii
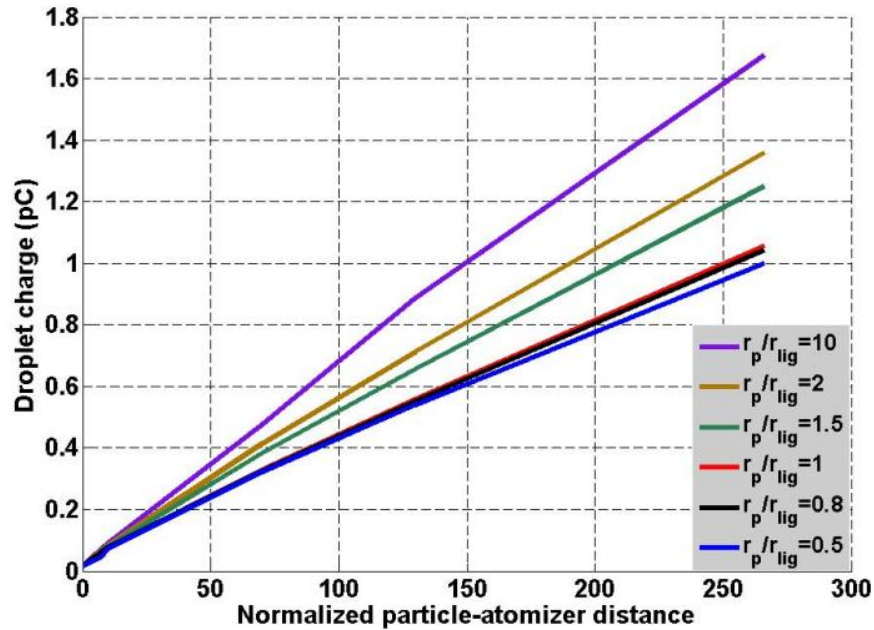
Figure 4.4: The effects of the ligament radius on the droplet charging level for r=15 μm

4.4.3 The proximity effect of adjacent ligaments

This section presents a study to examine the effect of two adjacent identical ligaments on the level of charging over the surface of a spherical droplet of radius equal to 15 μm. A 2D axisymmetric model is assumed initially, which physically means that a single ligament is surrounded by a cylindrical shell of liquid. Two cases have been simulated, in which the ligament length is equal to 0 and 4 mm. The numerical results in both cases can be divided into two distinct regions. The first region shows a rapid increase in the level of charging, as the spacing (d) increases, whereas the second one indicates that the magnitude of charge is practically saturated. Although the level of charging in the case of L=0 is lower than in the case of L=4 mm, the droplet attains a maximum charge more quickly. For a more realistic study, a 3D model has been generated to investigate the effect of a line array of adjacent ligaments on the droplet charging levels, where the computational domain has the shape of a rectangular layer, as shown in Figure 4.5. A very fine adaptive mesh was implemented in the area near the ligament tip using a total number of more than 200,000 tetrahedral elements of the side length between 5 μm and 50 μm, and much coarser elsewhere. The ligaments were connected to a high voltage electrode at the bottom, while

the grounded electrode was assumed at a distance of 25 cm from the bottom. Zero normal partial derivative is applied to the walls of the computational domain, which is equivalent to the symmetry boundary conditions along the strip thickness. This assumption creates a model, where a single ligament is accompanied on both sides by an infinite row of identical ligaments. The droplet and ligament radii are assumed to equal to 15 μm. The charge magnitudes over the droplet surface have been calculated for different values of the spacing (d) between adjacent ligaments and two values of the ligament lengths, $L=0$ and $L=4$ mm. In both cases it has been found that the charging level decreases as the spacing between the ligaments decreases, as shown in Figure 4.6.

Moreover, a series of numerical simulations have been performed for a very small spacing range such that $0.1<d<1$ mm. In the first group, the diameters of the spherical droplet and the cylindrical ligament are equal, whereas the droplet diameter is five times larger than the ligament diameter in the second one. It has been found that the charging level increases monotonically as the spacing between ligaments increases at fixed length. Also, the reduction of the ligament width will slightly increase the charging level, as shown in Figure 4.7. The simulated results also show a significant increase in the electric field intensity as the ligament length and width increases. Figure 4.8 displays one case of these results for the electric field distribution when the spacing $d=1$ mm.

$$\frac{\partial V}{\partial n} = 0 \qquad\qquad \frac{\partial V}{\partial n} = 0$$
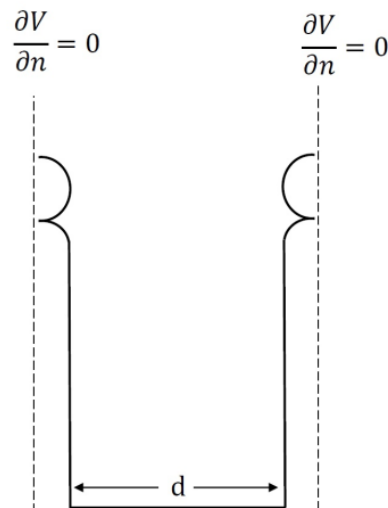
(a)
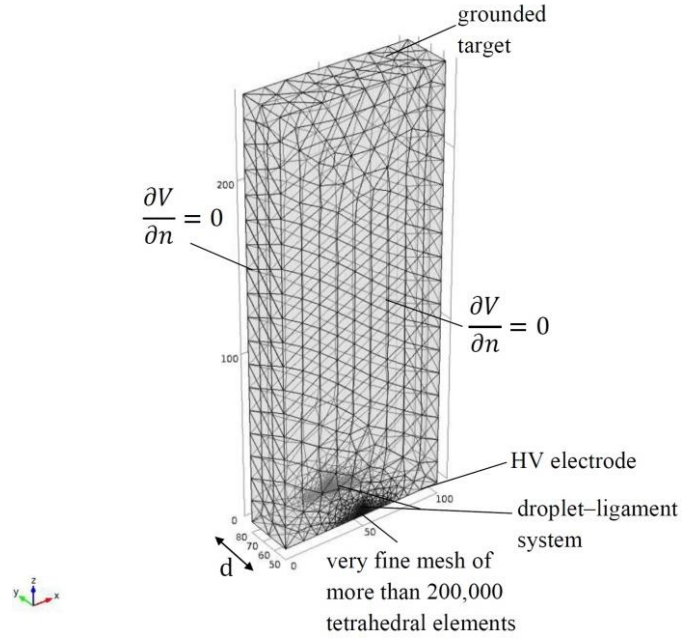
(b)

Figure 4.5: (a) The schematic representation of two adjacent ligaments from a row of identical ligaments (b) The mesh for 3D model of droplet charging with an infinite number of identical ligaments aligned in one row
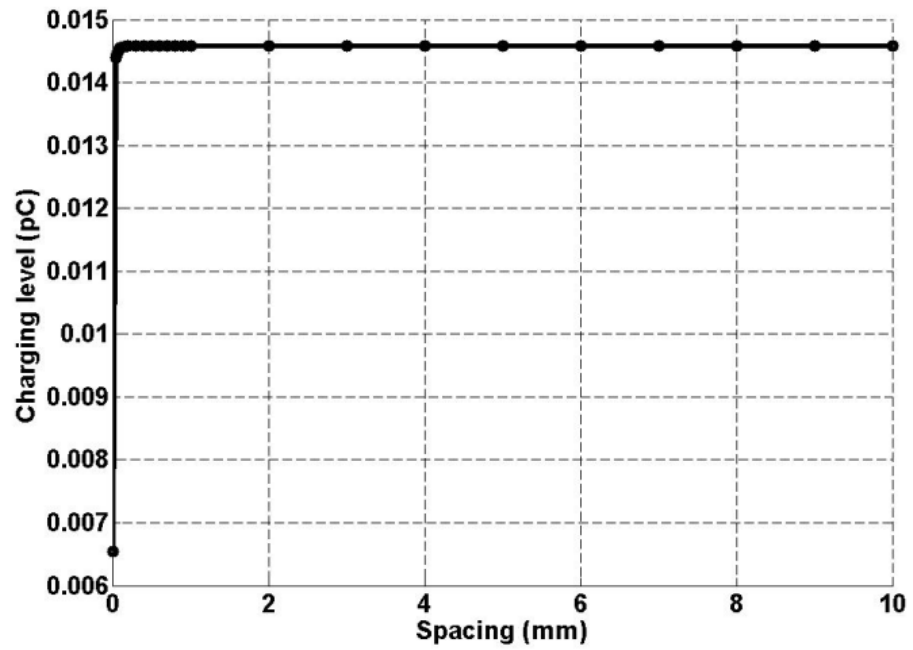
(a) *L*=0 mm
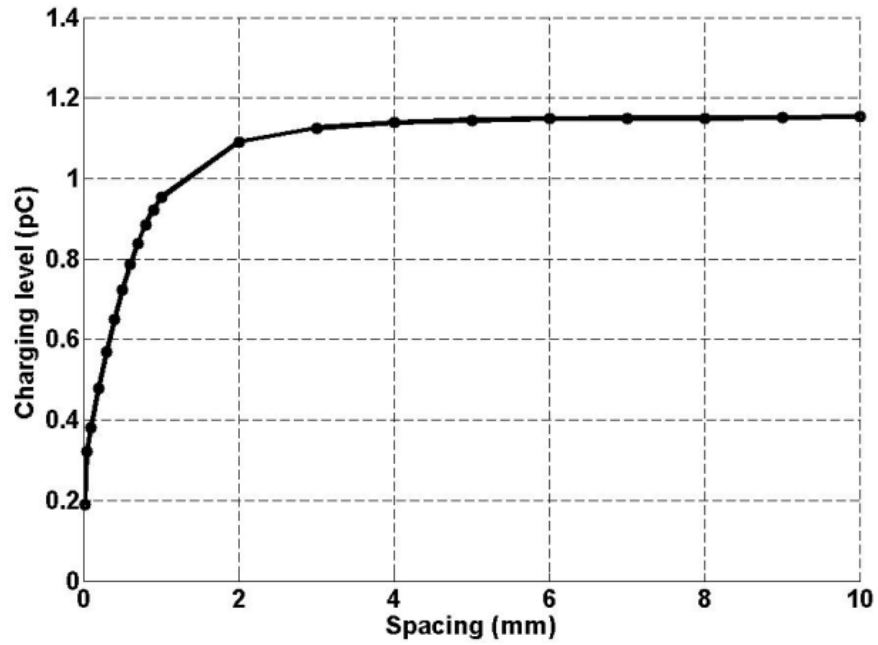
(b) *L*=4 mm

Figure 4.6: The effects of the spacing between adjacent ligaments on the droplet

charging level for *r*=15 μm
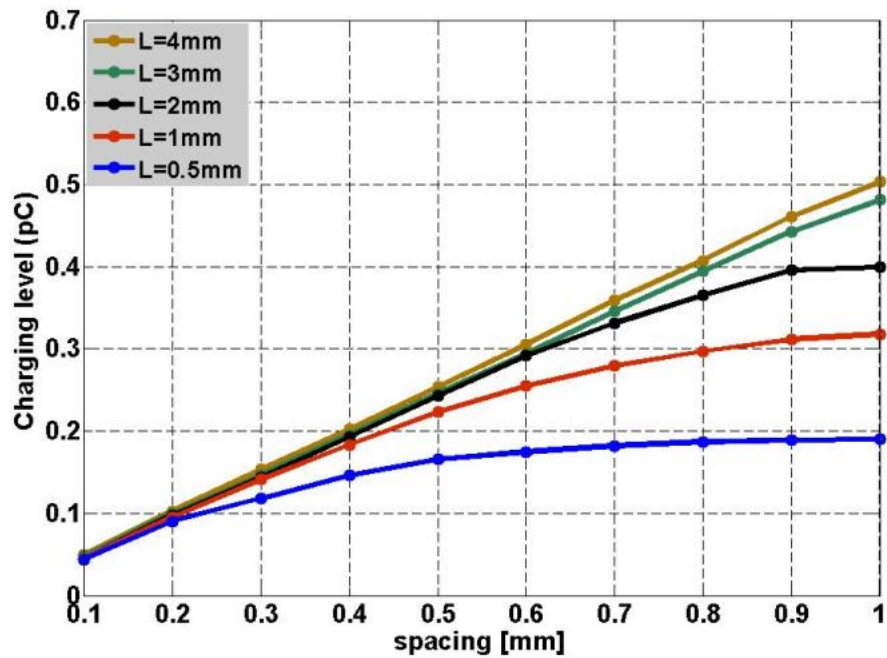
(a) r/r_{lig}=1
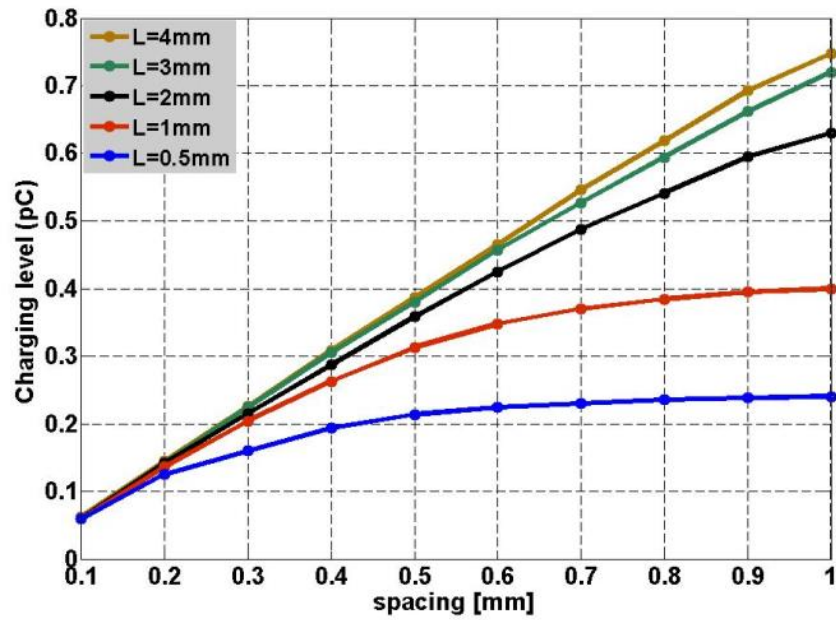
(b) r/r_{lig}=5

Figure 4.7: The droplet charging level for very small ligament spacing when r=15 μm
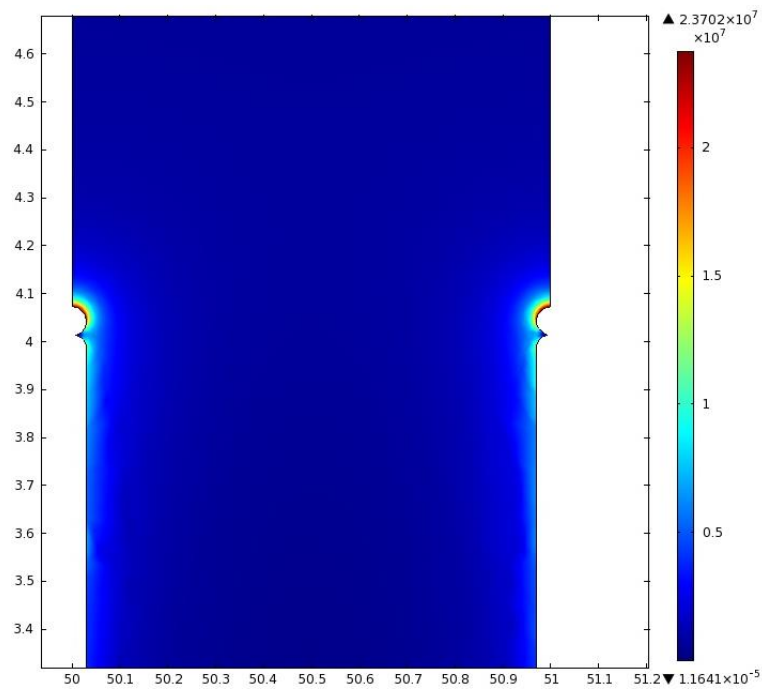
Figure 4.8: The electric field intensity in yz-plane of 3D model when

d=1 mm

4.4.4   The effect of previously formed droplets

The effect of a previously formed droplet on the charge of the next droplet has been studied numerically. The two droplets, namely, the primary and the secondary, are of the same size (r=15 μm), they are separated by a distance (d), and the ligament length is 4 mm. Figure 4.9 illustrates the models assumed for the first few droplets. The first droplet is charged to a level determined from a single-droplet model. It has been found that the presence of a secondary droplet increases the charge magnitude of the primary droplet and will eventually reach a saturation level, as the spacing (d) increases, as shown in Figure 4.10. Also, different cases have been analyzed, with additional formed droplets included. Here, it has been assumed that the spacing (d) between the adjacent droplets is fixed and equal to the diameter of the droplet ($2r$). It has been found that the electric field over the primary droplet decreases as the number of sequential droplets increases.
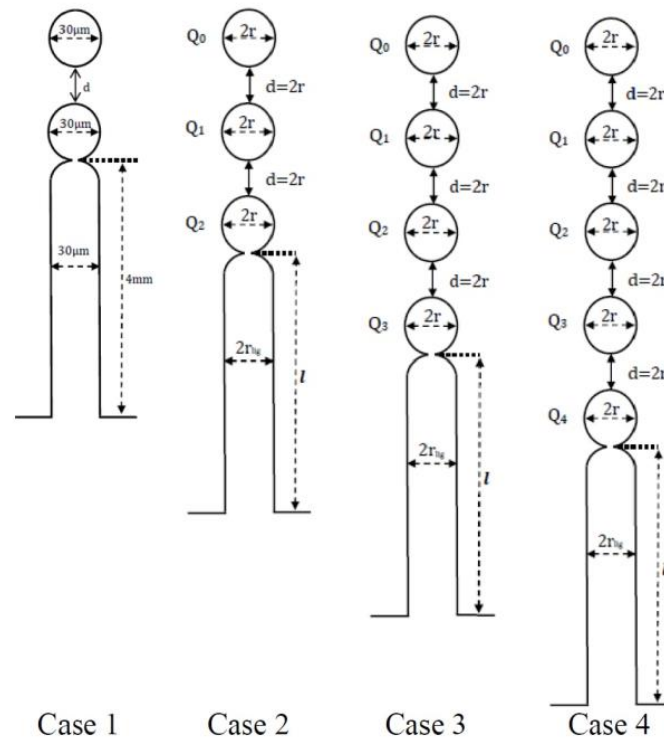
Figure 4.9: The model of the ligament break-up with multiple droplets

The distributions of the electric field for two different cases, when there are two and four ejected droplets, are shown in Figure 4.11. Table 4.2 illustrates the numerically estimated values for the total charge over the surface of the primary droplet in each case. It has been

found that by adding more droplets, the charge over the surface of the primary droplet decreases and eventually saturates at a value 30% lower than that of a single droplet.
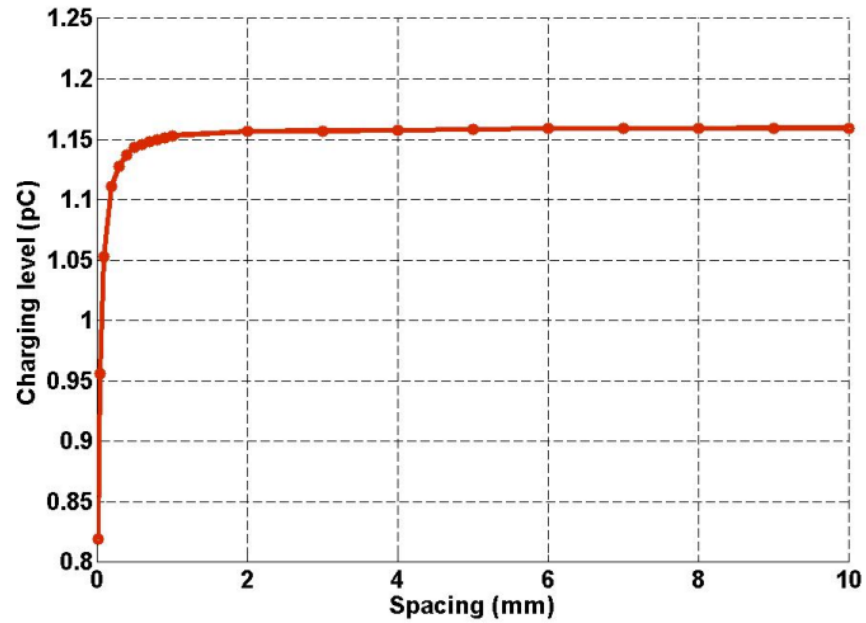
Figure 4.10: The relation between the droplet charging level and the spacing between two droplets
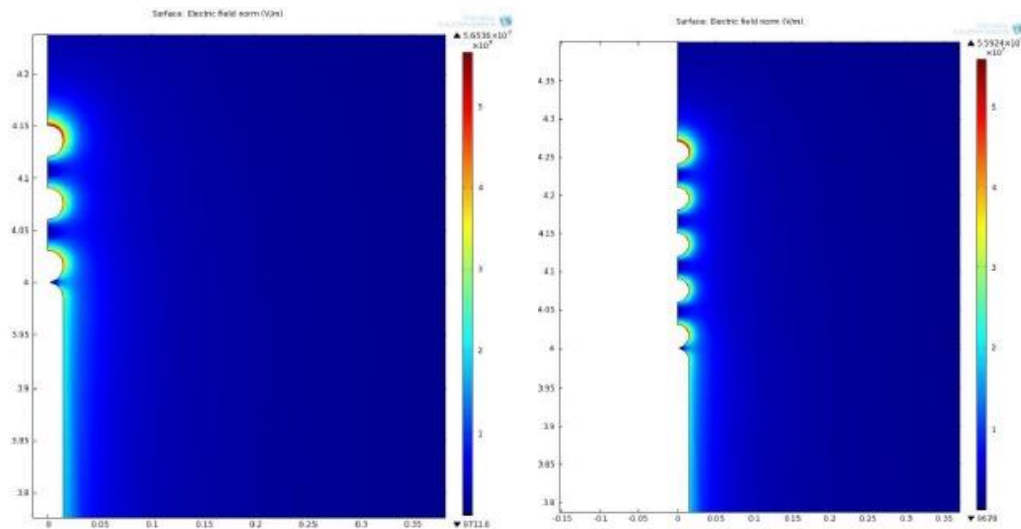
(a) Two droplets   (b) Four droplets

Figure 4.11: The distribution of the electric field

4.5 Dynamic formation of droplet

Up to this point the models have focused on the induction charging of sprayed droplets, with an assumed spherical shape and little attention has been paid to the process of droplet formation, which is assumed to be completely mechanical.

Table 4.2: Estimated charges for different number of ejected droplets

Total Charge (pC)					
	Q_0	Q_1	Q_2	Q_3	Q_4
Case 1	1.16	0.94	-	-	-
Case 2	1.16	0.94	0.88	-	-
Case 3	1.16	0.94	0.88	0.85	-
Case 4	1.16	0.94	0.88	0.85	0.83

In order to have more realistic droplet and ligament shapes the dynamics of atomization has also been investigated by simulating the motion and breakup of a ligament with a free surface and imposing the effects of surface tension. In a practical system, liquid paint flows along the inner surface of the rotating bell, which is maintained at a high voltage of 90 kV. It breaks up at the edge of the bell, forming a cloud of charged paint droplets. These droplets are driven to the substrate by the electric and aerodynamic forces. The interface separating the drop liquid and the ambient fluid is characterized by some surface tension. The surface tension was assumed to be constant. Although some authors have suggested that the surface tension is affected by the surface charge [19], no reliable data are available.

To model the dynamic evolution of the ligament, it is necessary to solve the Navier-Stokes equations, describing the fluid motion, as well as to track the interface between the fluid and ambient gas. The mathematical model for this part involves Eqs.(4.4)-(4.12), as shown in Section 4.2. This complex process can be readily set up and solved using the COMSOL commercial software, as shown in Figure 4.12. A level-set interface tracking method is adapted to represent the fluid domain and to track the evolution of its free boundaries. In this method, instead of zero thickness the interface is considered to have a finite thickness of the same order as the mesh size. The physical properties of both media change smoothly from the value on one side of the interface to the value on the other side in the interfacial transitional zone. The interaction between the electric field and the liquid jet coming out

of the capillary tube eventually leads to formation of small droplets. Depending on the flow rate and the strength of electric field, different spraying modes can occur.

Fluid was injected from the nozzle with a constant velocity and a jet was formed. Due to capillary instabilities, a droplet is eventually formed at the jet tip and its shape is determined by the competition between the surface tension and inertia forces. The jet is moving downward at a given initial speed. If the inlet velocity increases, it would be expected to have a longer ligament. The final shape of the droplet is a lateral ellipse, as shown in Figure 4.13.
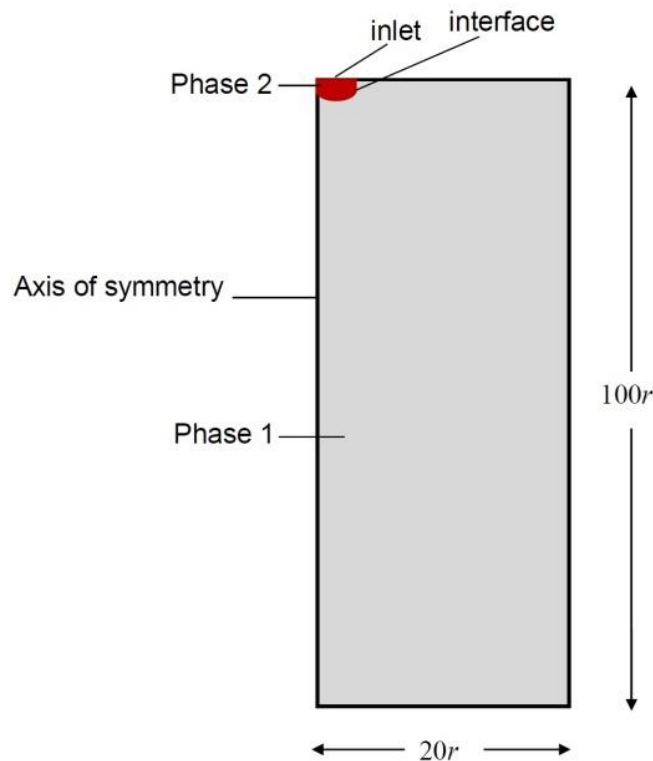
Figure 4.12: Schematic diagram of the dynamic model of droplet formation

At the moment of droplet separation the total electric charge accumulated on the droplet surface is calculated. The charge on the droplets can then be calculated by using integration of the normal component of the electrostatic displacement vector on the surface of the droplet. A comparison with the charging level of an assumed spherical droplet having the same effective volume is shown in Table 4.3. Three different dynamic cases were

investigated at different inlet velocities of 0.5, 0.75 and 1 m/s. It has been found that the predicted charging level of the spherical droplet is lower than the one of the actual shape in a range of 15-26%. As the charge is accumulated on the surface of the droplet, the estimated charge values for the actual droplet shape is slightly higher due to the fact that the lateral ellipse shape has a larger surface area than a sphere of the same total volume.
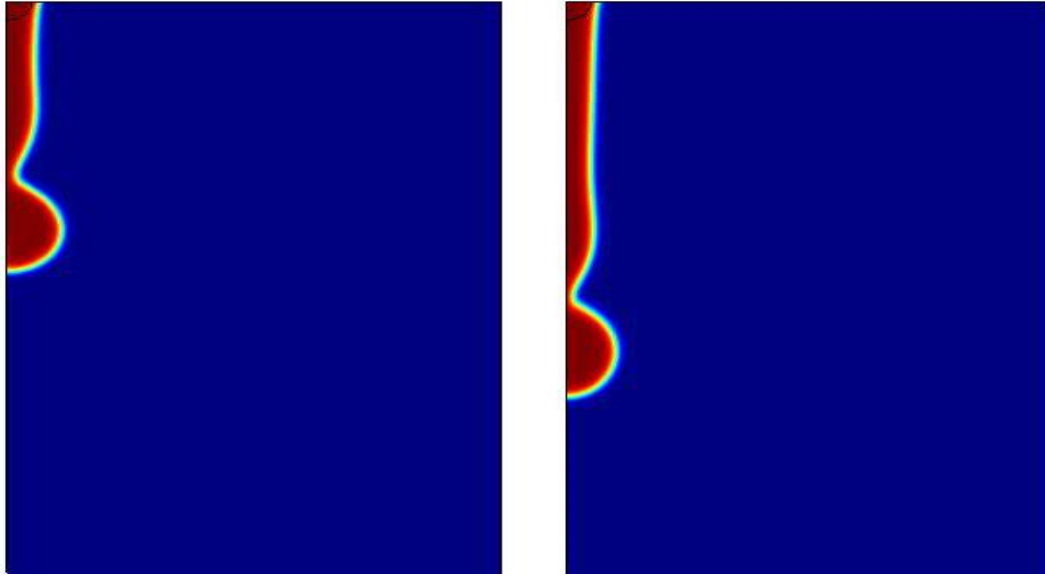
(a) U_0=0.5 m/s, η=0.06 Pa.s, γ=0.03 N/m   (b) U_0=0.75 m/s, η=0.06 Pa.s, γ=0.03 N/m

Figure 4.13: Evolution of the droplet shape at different inlet velocities

Table 4.3: The charging level of spherical and actual droplet

Ligament length L_{lig}	Ligament radius r_{lig}	Droplet radius r	Charging level	
			Spherical droplet	Actual droplet
260 μm	20 μm	40 μm	0.45 pC	0.55 pC[1]
320 μm	20 μm	46 μm	0.63 pC	0.85 pC[2]
600 μm	20 μm	50 μm	1.1 pC	1.3 pC[3]

[1] U_0=0.5 m/s, [2] U_0=0.75 m/s, [3] U_0=1 m/s

4.6   Conclusions

The investigation on the charging level over the surface of liquid droplet has been

performed for both static and dynamic models. In the static model, a numerical algorithm has been formulated for predicting the charge magnitude and the radius exponent as a function of the ligament length. The results provide some design parameters that allow the charge level to be predicted for different values of particle radius and ligament length. The effect of the ligament radius on the charging level has been found to be significant. The presence of adjacent ligaments will reduce the magnitude of the induced charge on the individual droplets. Also, the presence of sequentially formed droplets reduces the charging level of the primary droplet and the effect becomes stronger as the spacing between the droplets decreases. The dynamic modeling of droplet formation shows that the higher inlet velocity leads to a longer ligament length. The break-up simulation proved that the droplet shape prior to detachment is not purely spherical and that the static model underestimates the induced charge of the order of 15-26%.

References

[1] H. Osman, O. Ghazian, K. Adamiak, G.S.P. Castle, H.-T. Fan and J. Simmer, "The charging level of a ligament-droplet system atomized in a uniform electric field," Proc. IEEE/IAS Annual Meeting, Vancouver, BC, pp.1-7, Oct. 2014 (under review to be published in IEEE Trans. Ind. Appl.).

[2] A.G. Bailey, Electrostatic Spraying of Liquids, New York: John Wiley and Sons Inc., 1988.

[3] W.A. Macky, "Some investigation on the deformation and breaking of water drops in strong electric fields," Proc. R. Soc.Lond., vol.133, No.822, pp.565-587, 1931.

[4] J.M. Schneider, N.R. Lindblad, C.D. Hendricks, Jr., J.M. Crowley, "Stability of an electrified liquid jet," J. Appl. Phys., vol.38, No.6, pp.2599-2605, 1967.

[5] J.M. Lopez-Herrera, A.M. Ganan-Calvo, "A note on charged capillary jet breakup of conducting liquids: experimental validation of a viscous one-dimensional model," J. Fluid Mech., vol.501, pp.303-326, 2004.

[6] M.C.Y. Wong and J.S. Shrimpton, "Drop-charge correlations for polydisperse electrostatistically atomized liquid sprays," IEEE Trans. Dielectr. Electr. Insul., vol.11, No.2, pp.362-368, 2004.

[7] N. Toljic, G.S.P. Castle, K. Adamiak, "Charge to radius dependency for conductive particles charged by induction," J. Electrostatics, pp.57-63, 2010.

[8] S.O. Shiryaeva, A.I. Grigor'ev, "On stabilization of capillary instability of dielectric liquid jet by volume electric charge," Surface Engineering and Applied Electrochemistry, pp. 357–363, vol.45, No.5, 2009.

[9] S.-H. Lee, X.H. Nguyen, H.S. Ko, "Study on droplet formation with surface tension for electrohydrodynamic inkjet nozzle," J. Mechanical Science and Technology, pp.1403-1408, 26 (5), 2012.

[10] J. Domnick, A. Scheibe, Q. Ye, "The simulation of the electrostatic spray painting process with high-speed rotary bell atomizers, Part II: External charging," Part.Part.Syst.Charact., vol.23, pp.408-416, 2006.

[11] S.N. Reznik, A.L. Yarin, A. Theron, E. Zussman, "Transient and steady shapes of droplets attached to a surface in strong electric fields," J. Fluid Mech.,516, pp.349-377, 2004.

[12] D.H. Reneker, A.L. Yarin, H. Fong, S. Koombhongse, "Bending instability of electrically charged liquid jets of polymer solutions in electospinning," J. Appl. Phys., 87, pp.4531-4547, 2000.

[13] A.L. Yarin, S. Koombhongse, D.H. Reneker, "Bending instability in electrospinning of nanofibers," J. Appl. Phys., 89, pp.3018-3026, 2001.

[14] B. Ambravaneswaran, E.D. Wilkes, O.A. Basaran, "Drop formation from a capillary tube: comparison of one-dimensional and two-dimensional analyses and occurrence of satellite drops," J. Phys. Fluids, pp.2606-2621, vol.14, No.8, Aug. 2002.

[15] A. Jaworek, M. Lackowski, A. Krupa, T. Czech, "Electrostatic interaction of free EHD jets," J. Experiments in Fluids, pp.568-576, vol.40, No.4, Apr. 2006.

[16] R.P.A. Hartman, D. J. Brunner, D. M. A. Camelot, J. C. M. Marijnissen, B. Scarlett, "Jet break-up in electrohydrodynamic atomization in the cone-jet mode," J. Aerosol Sci., pp.65-95, vol.31, No.1, 2000.

[17] A.I. Zhakin, P.A. Belov, "Experimental study of the outflow of charged drops and jets," Surface Engineering and Applied Electrochemistry, pp.205-214, vol.49, No.3, 2013.

[18] N.J. Félici, "Forces et charges de petits objets en contact avec une électrode affectée d'un champ électrique," Revue générale de l'électricité, 75, pp.1145-1160, 1966.

[19] M.K. Mazumder, S. Banerjee, R.E. Ware, C. Mu, N. Kaya,C.C. Huang, "Characterization of tribocharging properties of powder paint," IEEE Trans. Ind. Appl., vol. 30, No.2, pp.365-369, 1994.

Chapter 5

Estimation of Droplet Charge Forming out of an Electrified Ligament in the Presence of a Uniform Electric Field[†]

5.1   Introduction

Much prior research has been completed to investigate the stability and disintegration of a liquid jet into a stream of discrete droplets in a uniform electric field [2-8], but relatively little work has been done on exploring the correlation between the droplet charge and droplet radius. Toljic et al. [9] investigated the charge to radius dependency for conductive particles atomized in an electric field between planar electrodes. The results showed that the ligament length has a strong effect on the particle charge to radius dependency. They found that the radius exponent is equal to two when the particle is in direct contact with a planar electrode, and decreases rapidly as the ligament length increases approaching a limit of 1.1.

Osman et al. [10] studied numerically the effect of the presence of previously formed droplets, the presence of adjacent ligaments as well as the ligament radius and length on the predicted droplet charging levels for ligaments formed from a planar high voltage electrode. The effect of the ligament radius on the charging level was found to be significant with larger charge resulting when the ligament radius is smaller than the droplet radius. This is important because in practice a narrow necking normally occurs prior to the droplet ejection. They also investigated the dynamic modeling of droplet formation at different inlet velocities. The results showed that the droplet shape prior to detachment is actually a prolate ellipsoid and that the spherical model underestimates the actual charge. Distortion of the droplet shape agrees with previous studies of droplet deformation in an external electric field [11].

[†] This work has been accepted for publication [1]. Extended work was carried out after paper acceptance and presented in the appendix.

In this chapter, a 2D axisymmetric numerical model was created using COMSOL, a Finite Element commercial software, to calculate the droplet charge formed from the end of a variable length ligament. Two cases have been compared: a ligament connected to a planar high voltage electrode and an isolated ligament supplied with a high voltage. In practice, the ligaments in paint sprayers are formed off the lip of a rotating cup, where the edge thickness is much larger (up to 10 times) than the ligament radius. This situation was simulated by expanding the model into a 3D linear array of ligaments forming from an electrode of variable width. With this, the droplet charge could be determined both for the single ligaments and for cases of an array of adjacent electrified ligaments.

5.2   Numerical model

The 2D axisymmetric stationary model consisted of a grounded electrode located 25 cm from the high voltage electrode, a cylindrical conductive liquid ligament of variable length and ejected spherical droplets with different radii. Two boundary conditions were considered. First, the ligament was assumed to be electrified through contact with a high voltage planar electrode. Then, the planar electrode was removed and the voltage applied directly to the ligament (Figure 5.1). The model was then extended to 3D (Figure 5.2) to enable the investigation of the effect of a linear array of adjacent ligaments on the droplet charge levels by applying the symmetry boundary conditions along the walls of the computational domain. In this latter model, the width of the lower electrode was also varied.
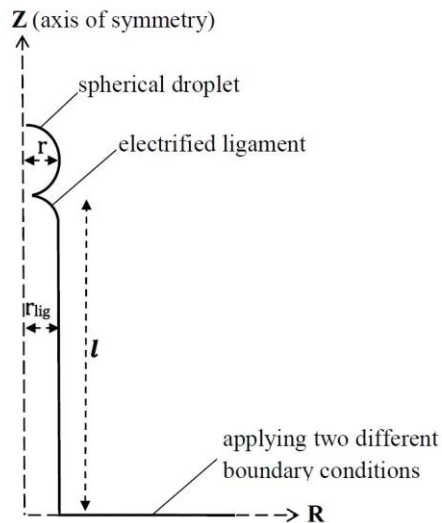
Figure 5.1: 2D model for a single ligament with two BCs: a) applied high voltage (90 kV) and b) dV/dn=0 for mirror plane
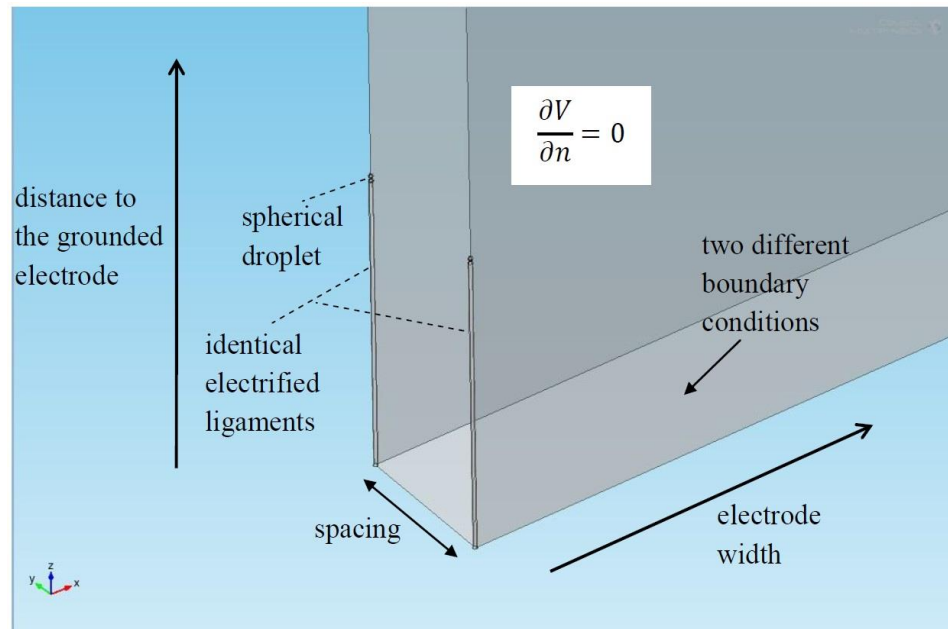
Figure 5.2: 3D model for an array of electrified ligaments with two BCs: a) applied high voltage (90 kV) and b) dV/dn=0 for mirror plane

5.3 Numerical results and discussion

5.3.1 Droplet charge for a single ligament

Osman et al. [10] previously estimated the electric charge on the surface of a spherical droplet, which is attached to a single ligament connected to a planar high voltage electrode in the 2D axisymmetric model. The simulation results were calculated for different droplet radii (r= 15, 30 and 45 μm) and ligament lengths (from 0 to 4 mm), and it was initially assumed that in all cases the droplet and ligament radii are equal. Their results demonstrated that the charging level increases with the droplet size and increases monotonically, as the ligament length increases. When a single spherical droplet is in direct contact with the surface of the planar electrode, it was confirmed that the charge magnitude coefficient and the radius exponent agree well with Félici's [12] predicted value, confirming the validity of the model.

In this section, the planar high voltage electrode was removed so that this case represents a single ligament-droplet system directly energized with high voltage. The results in this case reveal that the droplet charge also increases with radius, but in the order of 55 to 60 times higher than reported earlier [10] for the case, where the ligament was connected to a planar electrode. Also, the results show an opposite trend, where the charge slightly decreases, as the ligament length increases (Figure 5.3). These results are somewhat surprising as they show such large differences in the level of charge and the influence of ligament length. However, it appears that the effect of the planar electrode is to partially screen the electric field at the end of the ligament, and this influence decreases as the ligament gets longer. On the other hand, for the case where the ligament stands alone, the field strength is much stronger at the end of the ligament and it decreases slightly with length, as more electric flux is attracted to the surface of the ligament.
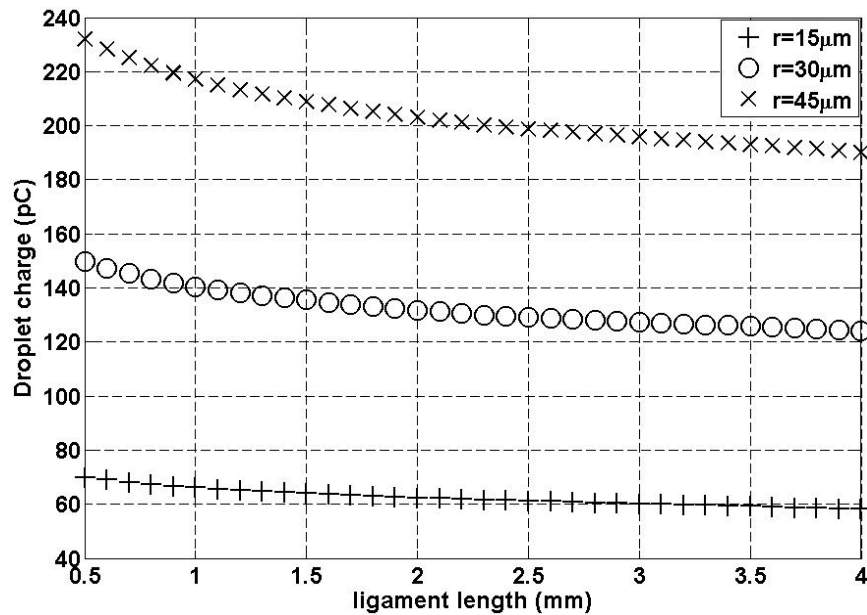
Figure 5.3: The droplet charge for a single ligament in absence of the planar electrode assuming three different droplet sizes

5.3.2   Linear array of electrified ligaments

This section presents a study to examine the effect of a linear array of ligaments on the level of charging over the surface of a spherical droplet of radius equal to 15 μm in absence

of the planar electrode. A 3D model described in [10] was modified such that a condition of zero normal partial derivative was applied to the lower electrode and walls of the computational domain, which is equivalent to the symmetry boundary conditions. This assumption creates a model, where a single ligament is accompanied on both sides by an infinite row of identical electrified ligaments. The droplet and ligament radii are assumed to be equal. The charge magnitudes over the droplet surface have been calculated for different values of the spacing between adjacent ligaments and for different ligament lengths (Figure 5.4).
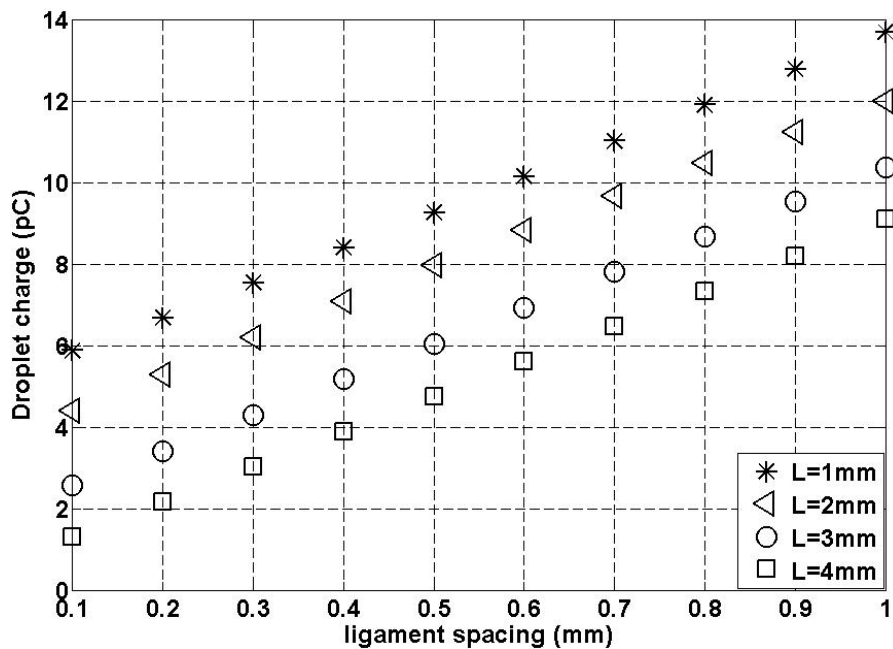
Figure 5.4: The charge for a 15 μm droplet formed from an array of ligaments of different lengths in absence of the planar electrode

Similarly to the previous results presented in [10], it was found that the charging level increases, as the spacing between ligaments of fixed length increases, but for the longer ligaments, the droplet charge decreases compared with the shorter ones at a given spacing (Figure 5.4).

A linear array of ligaments of fixed length of 1 mm and spacing of 0.5 mm was then assumed for ten values of droplet radius and the effect of the electrode width on the droplet charging level determined. The electrode width was varied from one extreme condition

that of a planar electrode, approximated as a 100 mm strip, to the case of no electrode. These results are shown in Figure 5.5. For the case of a planar electrode, the results show that the estimated droplet charge increases monotonically with the droplet radius. As the electrode width shrinks to 0.5 mm, the charge magnitude increases by about a factor of 30 and for an even narrower width of 20 μm, where the electrode width is in the same order of the droplet radius, charge is approximately 40 times larger. Finally in the extreme case when the electrode is absent and the ligaments become isolated, the charge magnitude was found to increase up to 50 times the case of planar electrode. These results also enable the value of the dependency of charge on radius to be estimated and show an exponent value of about 1.1 which agrees well with the value reported in [10].
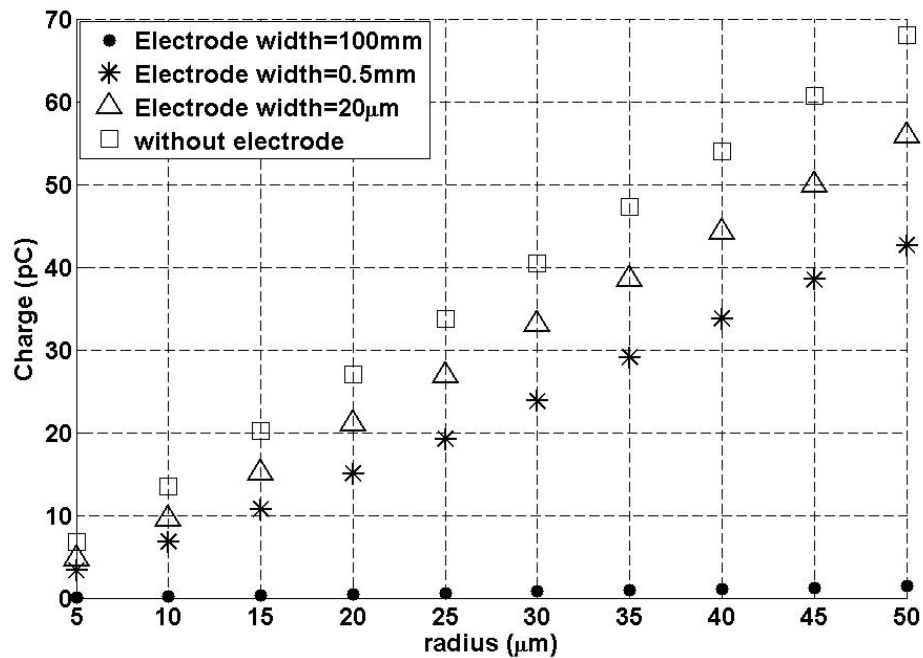
Figure 5.5: The droplet charge levels for an array of ligaments of 1 mm length, spaced 0.5 mm apart assuming variable electrode widths

5.4 Conclusions

This study sheds some light on the design parameters that allow the charge level to be predicted for different droplet sizes and ligament lengths. A 2D axisymmetric model was generated for predicting the charge magnitude by assuming different boundary conditions.

When the electrode is removed and the ligament itself forms the high voltage electrode, it was found that the droplet charge greatly increases in magnitude by a factor of up to 60 times. Also, a 3D model has been created to examine the effect of the spacing between a linear array of identical ligaments on the droplet charge in the absence of the planar electrode. It was found that the droplet charge increases, as the spacing between adjacent ligaments increases. Also it was demonstrated that the electrode width strongly affects the droplet charge. In particular, as the width of the electrode decreases, the charges on the droplets in the linear array may increase by a factor of up to 50. This large influence of the boundary conditions suggests that the next stage of the modelling is to include the cylindrical geometry of the sprayer as well as the other important parameters particularly the space charge due to previously formed droplets. An extended work of this Chapter is presented in the Appendix A to investigate the effect of a linear and circular array of ligament on the charging level.

References

[1] H. Osman, G.S.P. Castle, K. Adamiak, H.-T. Fan and J. Simmer, "Estimation of droplet charge forming out of an electrified ligament in the presence of a uniform electric field," IOP Conference on Electrostatics 2015, Southampton, UK, p.46, April 2015.

[2] J.M. Schneider, N.R. Lindblad, C.D. Hendricks, Jr., J.M. Crowley, "Stability of an electrified liquid jet," J. Appl. Phys., vol.38, No.6, pp.2599-2605, 1967.

[3] W.A. Macky, "Some investigation on the deformation and breaking of water drops in strong electric fields," Proc. R. Soc.Lond., vol.133, No.822, pp.565-587, 1931.

[4] J.M. Lopez-Herrera, A.M. Ganan-Calvo, "A note on charged capillary jet breakup of conducting liquids: experimental validation of a viscous one-dimensional model," J. Fluid Mech., vol.501, pp.303-326, 2004.

[5] M.C.Y. Wong and J.S. Shrimpton, "Drop-charge correlations for polydisperse electrostatistically atomized liquid sprays," IEEE Trans. Dielectr. Electr. Insul., vol.11, No.2, pp.362-368, 2004.

[6] A.I. Zhakin, P.A. Belov, "Experimental study of the outflow of charged drops and jets," Surface Engineering and Applied Electrochemistry, pp.205-214, vol.49, No.3, 2013.

[7] R.J. Pfeifer, C.D. Hendricks, "Charge to mass relationship for electrohydrodynamically sprayed liquid droplets," Phys. Fluids, pp.2149-2154, 1967.

[8] J.W. Schweizer, D.N. Hanson, "Stability limit of charged drops," J. Colloid Interface Sci., pp.417-423, 1971.

[9] N. Toljic, G.S.P. Castle, K. Adamiak, "Charge to radius dependency for conductive particles charged by induction," J. Electrostatics, pp.57-63, 2010.

[10] H. Osman, O. Ghazian, K. Adamiak, G.S.P. Castle, H.-T. Fan and J. Simmer, "The charging level of a ligament-droplet system atomized in a uniform electric field," Proc. IEEE/IAS Annual Meeting, Vancouver, BC, pp.1-7, Oct. 2014 (under review to be published in IEEE Trans. Ind. Appl.).

[11] K. Adamiak and J.M. Floryan, "Dynamics of water droplet distortion and breakup in a uniform electric field," IEEE Trans. Ind. Appl., vol.47, No.6, pp.2374-2383, 2011.

[12] N.J. Félici, "Forces et charges de petits objets en contact avec une électrode affectée d'un champ électrique," Revue générale de l'électricité, 75, pp.1145-1160, 1966.

Chapter 6

Comparison between the Numerical and Experimental Deposition Patterns for an Electrostatic Rotary Bell Sprayer[†]

6.1   Introduction

Numerical analysis of the electrostatic painting system as used in the automotive industry can provide a valuable design tool for optimization as the process involves many coupled phenomena [2-7]. One of the criteria for validating the numerical models is to achieve a satisfactory agreement between the numerical and the experimental results for the same set of the input parameters. The aim of this work was to build a realistic model by gradual incorporation of the all relevant mechanical and electrical phenomena. Mechanical effects included the shaping and downdraft air patterns, the motion of the poly-dispersed particles and the motion of the coated target. Electrical effects included the electric field distribution due to the applied voltage as well as particle and ionic space charge, corona discharge current and the electrohydrodynamic flow.

Toljic et al. [8,9] developed a 3D numerical model using FLUENT commercial software to solve the mechanical part of the spraying process and the User Defined Functions (UDFs) were used to solve the Poisson equation, which governs the electric field distribution, and the charge continuity equation, to predict the ionic space charge, generated by the corona discharge. The developed numerical model proved its capability to handle different configurations with arbitrary shape of the target and with relatively complex motion patterns. The effects of several critical parameters on the deposition uniformity, which included the total number of injected particles, the charge-to-mass ratio, the particle size distribution and the air velocity, have been discussed in many different cases. It was apparent that the developed numerical models, although they were able to provide some insights into the effects of different parameters on the painting quality and efficiency, took excessive computational time and provided only qualitative agreement with the

---

[†] This work has been accepted for publication [1].

experimental data. One problem was an insufficient coverage inside the cone of the spray at the central part of the spray pattern. This was believed to be due to the inadequacy of the model in representing the atomization process. Therefore, it was necessary to modify the sprayer injection pattern by introducing a series of injections at different angles. The numerical results from the modified numerical model showed better agreement when they were compared with the experimental data. However, a full understanding of the effect of the injection angle and fractional mass flow on the particle injection was not complete. An alternative approach has been proposed, where the charged particles were injected from three virtual rings placed at a certain distance *h* from the bell. The effects of variation of the total number of injections, the mass flow rate and the radius of each injection ring on the deposition thickness and the uniformity have been examined for a number of different cases of stationary and moving flat targets.

6.2   Numerical model

The 3D numerical model of the painting system encompasses a simplified geometry of the electrostatic bell atomizer, which is kept stationary, and a thin target plate, situated 25 cm away from the atomizer, as depicted in Figure 6.1. The computational domain is a cube of 2.5 m in width, 2.5 m in height and 1.2 m in length. The entrained air flows out of the atomizer through a ring-shaped slit of 1mm width. The airflow rate is 700 slpm and the downdraft velocity is neglected. The target is a square plate of side length equal to 90 cm. The atomizer is connected directly to a high voltage power supply of -90 kV and the corona current is -10 μA.

The computational domain was created by using the ICEM [10] software package and was meshed in an unstructured manner. The mesh is refined densely in the cone-shaped area between the atomizer and the target and is much coarser elsewhere, as shown in Figure 6.2. The total number of cells used for meshing is around 600,000. All the volume cells are tetrahedral and all the surface cells (faces) are triangular. The turbulent air flow was calculated using the Realizable k-ε model. The equations of particle motion were tracked by the discrete random walk model. The particle size and charge-to-mass ratio distributions are illustrated in Table 6.1 [11].

Coupling between the air flow and the particle discrete phase is included via source terms of mass and momentum. The electric field, generated by the applied voltage between the bell atomizer and the grounded target, and the space charge formed by the charged particles and ions, is governed by Poisson's equation.
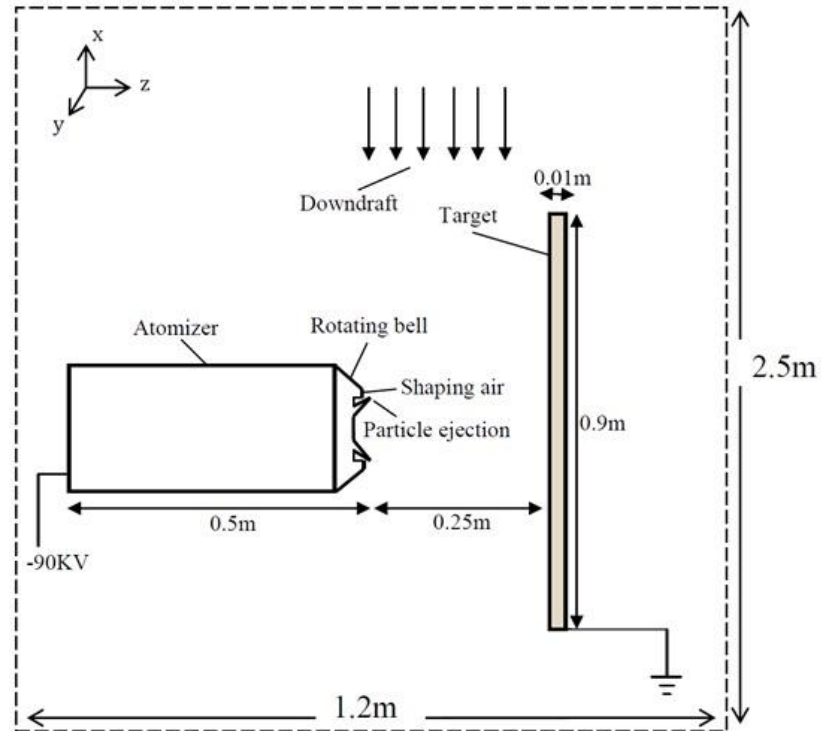
Figure 6.1: Schematic diagram of the computational domain
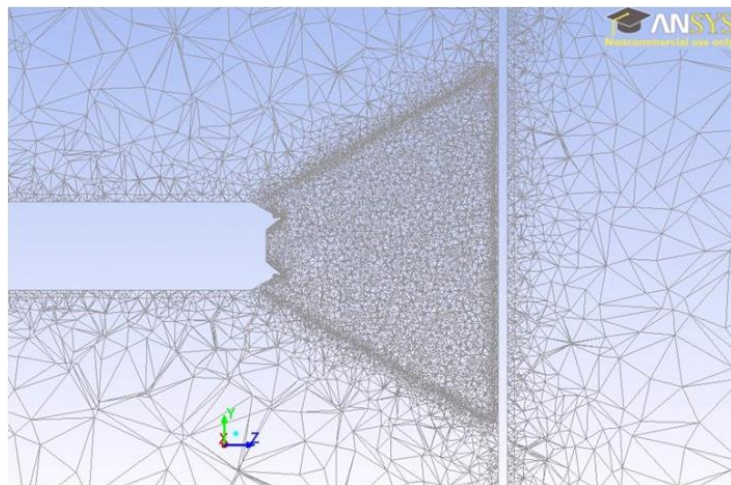
Figure 6.2: Cross-section of the mesh between the atomizer and the target

Table 6.1: Particle size and charge-to-mass ratio distribution [11]

Size band	Particle diameter (µm)	Mass flow rate (g/s)	Charge-to-mass ratio (mC/kg)[†]
1	10	0.03	-3.5
2	15	0.15	-2.33
3	20	0.36	-1.75
4	25	0.6	-1.4
5	30	0.84	-1.17
6	35	0.9	-1
7	40	0.81	-0.875
8	45	0.588	-0.778
9	50	0.45	-0.7
10	55	0.39	-0.636
11	60	0.24	-0.583
12	65	0.186	-0.538
13	70	0.168	-0.5
14	75	0.15	-0.467
15	80	0.138	-0.438

[†]$\frac{q}{m} \propto \frac{1}{r}$

$$\nabla^2 \phi = -\frac{\rho}{\varepsilon} \tag{6.1}$$

where ϕ is the electrical potential, ρ is the total space charge density and ε is the electrical permittivity. Then, the electric field intensity can be calculated as

$$\boldsymbol{E} = -\nabla \phi \tag{6.2}$$

The User Defined Scalar transport equations (UDS) were used to solve Poisson's equation. The total space charge density is given by

$$\rho = \rho_P + \rho_i \tag{6.3}$$

where ρ_P is the space charge density of the charged particles and ρ_i is the space charge density due to the ions. The total space charge density of the charged particles can be calculated as

$$\rho_P = \sum_{i=1}^{N} \left(\frac{q_i}{m_i} \right) C_i \tag{6.4}$$

where q_i/m_i is the total charge-to-mass ratio of the particles of the given size in the cell, C_i is the concentration of the particles and N is the total number of particle sizes. The total space charge density due to the ions can be expressed as

$$\rho_i = \frac{J}{\mu_i E} \tag{6.5}$$

where $\pmb{J}$ is the total corona current density and μ_i is the ion mobility. It has been assumed that the corona current density is fixed and known at the edge of the atomizer.

6.3 Results and discussion

6.3.1 Stationary target

The target is positioned such that its center lies directly on the sprayer centerline. The beginning stage of our simulation considered a simple injection pattern by using a single stream of injected particles. There was a discrepancy between the numerical and experimental results of the deposition thickness at the central part of the target surface. The numerical results showed asymmetric ring shape of deposition pattern, where the deposition thickness decreases sharply from the ring to have no deposition at the center of the target. In order to simulate the actual spray cloud of injected droplets, the injection pattern was modified by introducing a series of injection points with different angles θ. These angles were determined by the spacing between the atomizer and the target, and the position at which the injected particles will hit the target, as can be shown in Figure 6.3. Different injection angles were selected to cover the range of distances from the center of the target and close to 30 cm away. Also, each injected particle was assigned to a certain fraction of the total mass flow. The total number of injection angles affects the total number of super-particles present in the model. The total number of super-particles can be calculated as

$$\text{No. of super-particles} = N_1 \times N_2 \times N_3 \tag{6.6}$$

where N_1 is the total number of injection points, N_2 is the number of size bands and N_3 is the number of different particle velocities. In addition, the values of these injection angles as well as the percentages of the mass flow for each group of injected particles will affect

the film thickness distribution. Therefore, appropriate selection for a suitable injection pattern will help to match the numerical and the experimental results for the deposition thickness. Three different cases were performed by using injection angles for poly-dispersed charged particles. The total number of super-particles was relatively high, which includes 15 different size bands, as shown in Table 6.1, and they were injected from 256 points. For each band, a different number of injection angles and multiple fractions of mass flow were assumed.
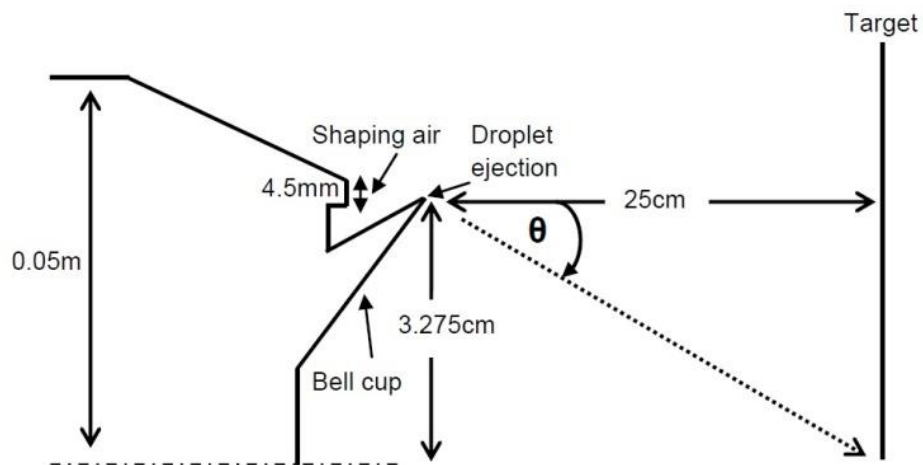
Figure 6.3: Schematic diagram of the injection angle

Three different injection patterns were investigated and they are illustrated in Table 6.2. A comparison between the numerical and the experimental results has been obtained. For the first case the injections were increased at the smaller angles (-7.5, 0, 5, 10 and 15 degrees) and decreased at higher angles of 25 and 30 degrees. The injections for the second and third cases were very similar, however, more injections were included at larger angles of 25, 35 and 45 degrees for the second case, and 20, 25, 30, 35 and 45 degrees for the third case. As a result, higher deposition thickness at the central part of the target for the first case can be realized than the last two cases due to the increased mass injections at the lower angles. On the other hand, the numerical results for the last two cases show a wider distribution of paint rather than the distribution of the first case due to the increased mass injections at higher angles. Also, the numerical results of the last two cases show a good agreement with the experimental results, as shown in Figure 6.4.
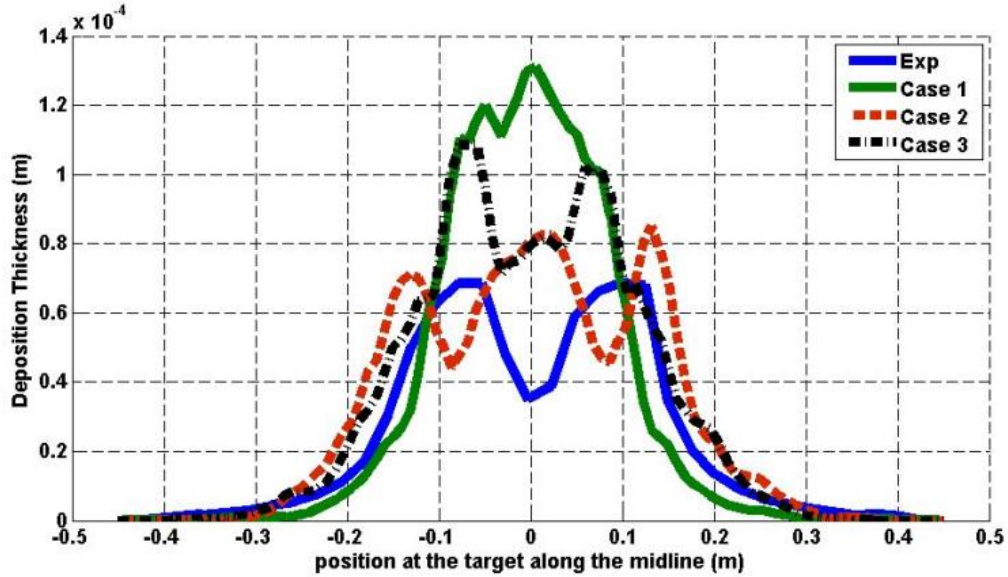
Figure 6.4: Comparison between the experimental and the numerical results for three cases with averaging and de-rating factor=0.35

The raw accumulation data as produced by the ANSYS software needed to be processed in order to get more realistic representation of the accumulation profile, because the particle trajectories that are simulated in ANSYS exhibit artificially induced random behavior which in turn introduces some irregularities to the profile. Also, ANSYS stops tracking the particles the moment they hit the target, whereas the experimental set up the deposited paint spreads under the influence of the gravitational and mechanical forces. The number of neighboring cells was used in the averaging and filtering procedure in order to get the smoothed output. The de-rating factor for evaporation of the liquid paint solvent was assumed to equal 0.35. Figure 6.5 demonstrates the contours of the accumulation rate for the three cases. The contours show different levels of deposition thicknesses at the central part of the spray pattern, based on the assumed percentages of mass injection for each injection angle.
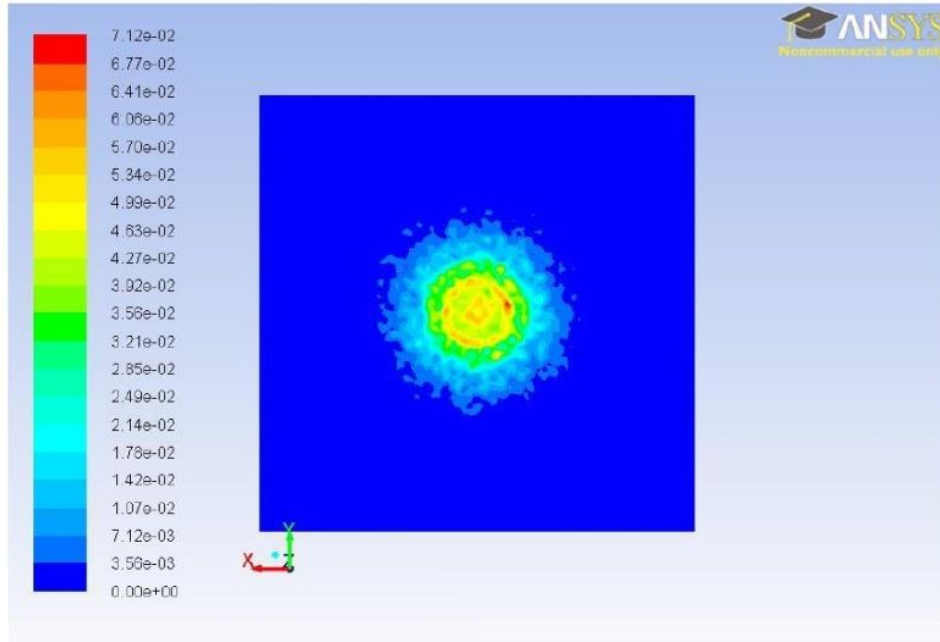
(a) Case#1
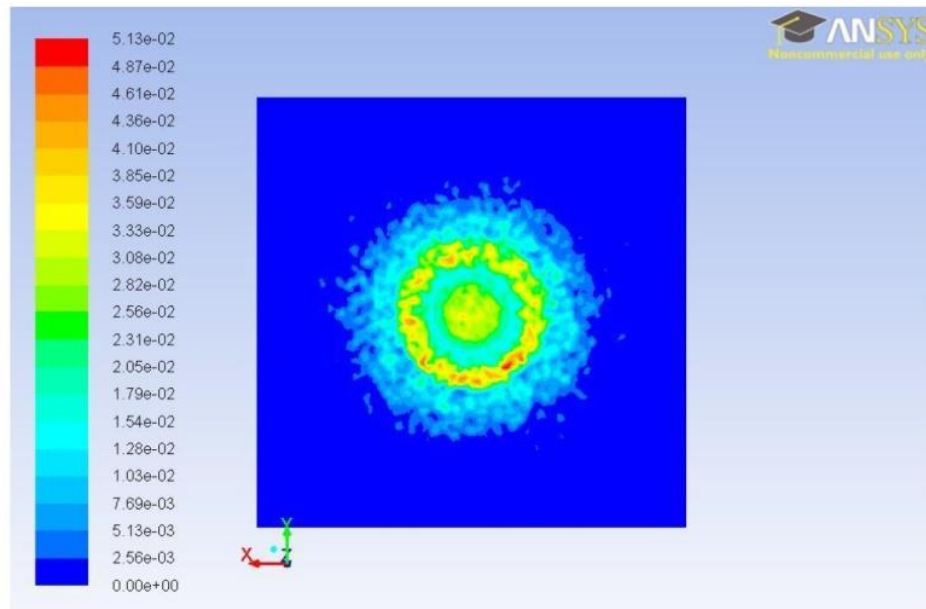
(b) Case#2
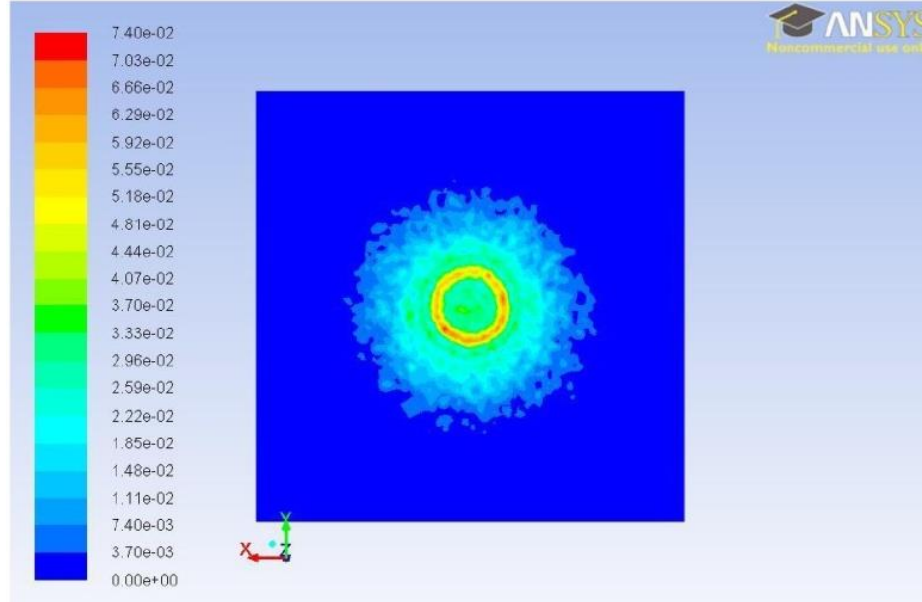
(c) Case#3

Figure 6.5: Contours of the accumulation rate

Table 6.2: Injection pattern for three cases of poly-dispersed particles

Injection angles (deg.)	Mass flow (%)		
	Case#1	Case#2	Case#3
-7.5	10%	4%	4%
0	10%	4%	4%
5	20%	4%	4%
10	25%	4%	4%
15	20%	4%	4%
20	0%	0%	10%
25	10%	30%	15%
30	0%	0%	15%
35	5%	30%	25%
45	0%	20%	15%

6.3.2   Multiple injections along virtual rings

In order to obtain further agreement of the deposition thickness and the uniformity of paint, further modifications of the paint injection were undertaken to better represent the actual paint distribution. The alternative approach was to assume the charged particles were injected from three virtual rings placed at a certain distance h from the bell, as shown in

Figure 6.6. Many different cases have been examined, in which it has been assumed that h=7 mm. The results of the deposition thickness were determined for each case.

Table 6.3 summarizes the parameters used in this model. The variations of the number of injection points, mass fractions and the radii of the injection rings have been considered. In some cases, the total number of injection points was varied, and the number of mass fractions was equal in each injection ring. It is aimed to test the effects of variation of these parameters, as well as the radii of the injection rings, on the deposition thickness and uniformity. Then, the total number of the injection points in each ring has been changed in the subsequent cases such that the distribution of the injection points is uniform along their circumferences. From Figure 6.7, it has been found that the numerical results of the deposition profile in the base case are the most acceptable results when compared with the experimental profile.

(a) Top view

(b) Side view
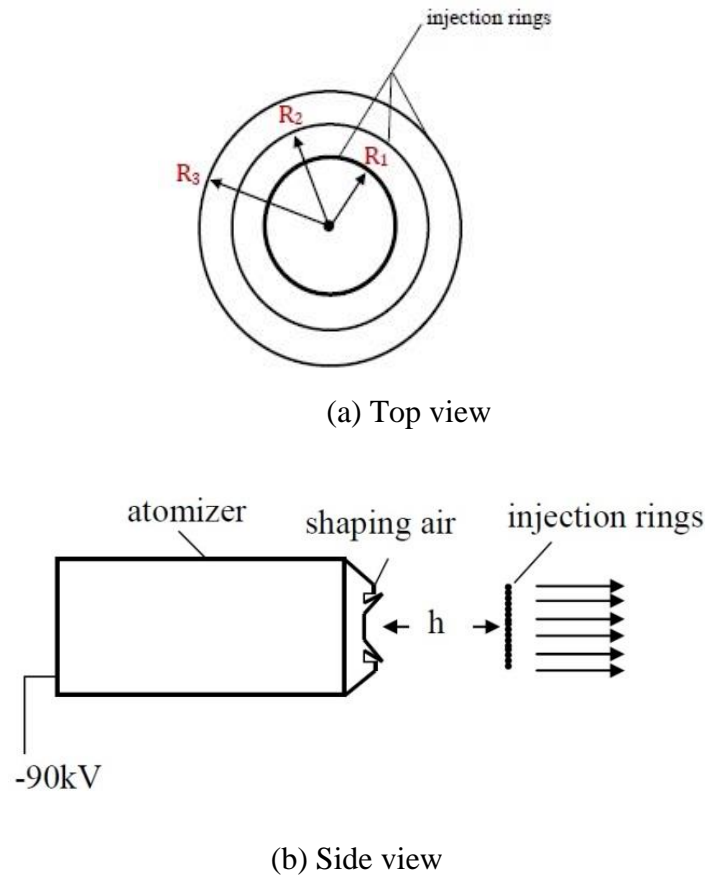
Figure 6.6: Schematic diagram of three virtual injection rings of radii R_1, R_2 and R_3 at distance h

Table 6.3: Model parameters for many cases by injections along three rings

Parameters	Cases of study			
	Base case	Case#1	Case#2	Case#3
No. of injection points (inner, middle, outer)	32 64 256	32 64 256	114 118 121	114 118 121
Fractions of mass flow rate in each ring	1/3 1/3 1/3	1/2 1/4 1/4	1/2 1/4 1/4	1/4 1/2 1/4
Radius of each injection ring (cm)	3.2 3.3 3.4	3.2 3.3 3.4	3.2 3.3 3.4	3.2 3.3 3.4
	Case#4	Case#5	Case#6	Case#7
No. of injection points (inner, middle, outer)	114 118 121	114 118 121	114 118 121	114 118 121
Fractions of mass flow rate in each ring	1/6 2/3 1/6	1/6 2/3 1/6	1/3 1/3 1/3	1/3 1/3 1/3
Radius of each injection ring (cm)	3.2 3.3 3.4	2.8 3.2 3.6	2.8 3.2 3.6	3 4 5

Figure 6.7: Comparison between the experimental and the numerical results with averaging and de-rating factor=0.35

6.3.3   Strip painting of a moving target

In this section, a moving mesh is incorporated and the target moved in the x-direction. Its speed is 15 cm/s and it needs 6 seconds to complete one strip of paint, as shown in Figure 6.8. Based upon our previous study in the Sections A and B, multiple injections along three virtual rings with different injection angles for each ring were assumed. Two cases have been examined by combining the base case from Table 6.3 with each of the case#2 and the case#3 from Table 6.2, respectively. The injection pattern for the first case included greater increase of mass injections at larger angles than the injection pattern of the second case. Table 6.4 illustrates the injection pattern and the model parameters which have been used for the two cases. The calculations of the film thickness across the yz-plane were plotted and compared with the experimental results at three different distances from the edge of the target, as shown in Figure 6.9.
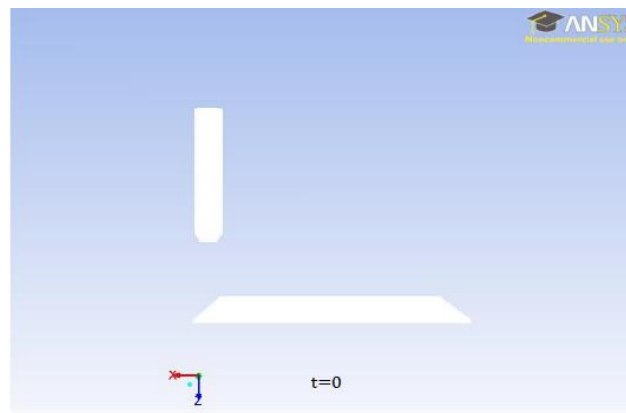
(a) Initial state ($t=0$)
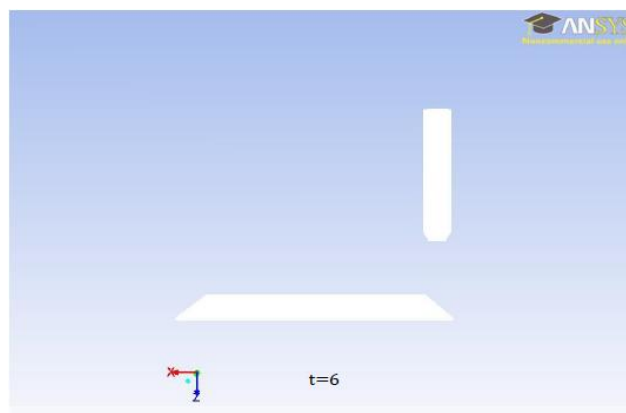
(b) Terminal state ($t=6$ s)

Figure 6.8: Positions of the target
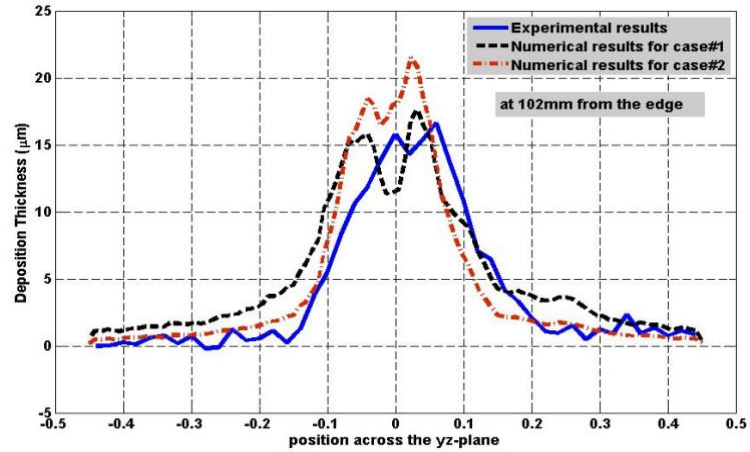
(a) 102 mm from the edge
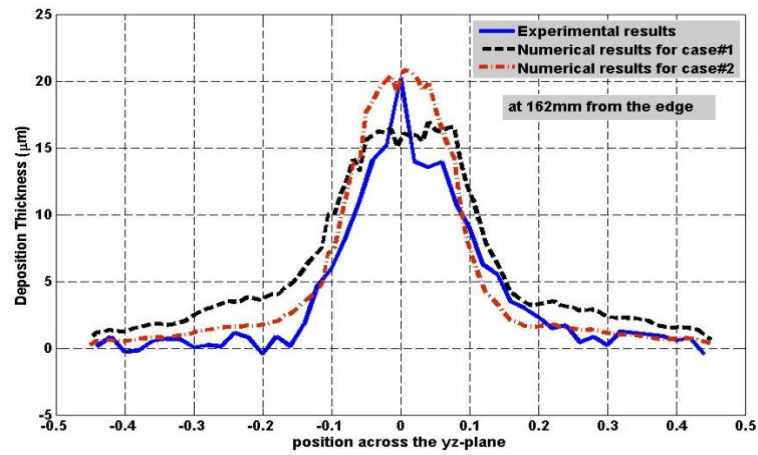
(b) 162 mm from the edge
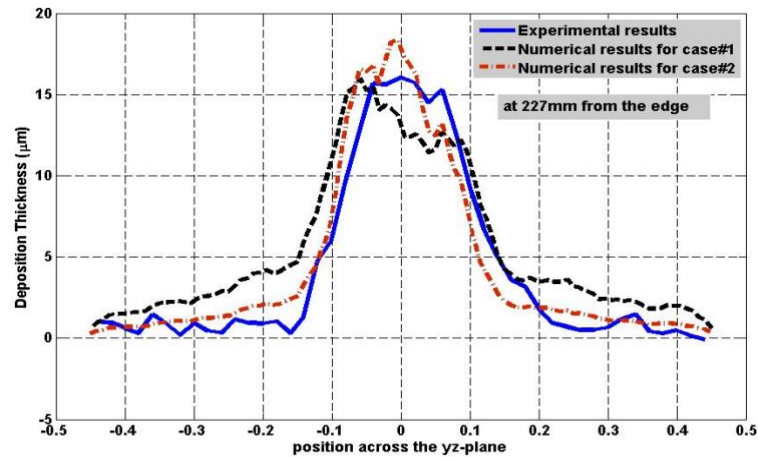
(c) 227 mm from the edge

Figure 6.9: Comparison between the numerical and the experimental results of the deposition thickness across the *yz*-plane for two cases

Table 6.4: Injection pattern for two cases of strip painting

Injection angles (deg.)	Mass flow (%)					
	Case#1			Case#2		
-7.5	4%			4%		
0	4%			4%		
5	4%			4%		
10	4%			4%		
15	4%			4%		
20	0%			10%		
25	30%			15%		
30	0%			15%		
35	30%			25%		
45	20%			15%		
No. of injection points (inner, middle, outer)	32	64	256	32	64	256
Fractions of mass flow rate in each ring	1/3	1/3	1/3	1/3	1/3	1/3
Radius of each injection ring (cm)	3.2	3.3	3.4	3.2	3.3	3.4

6.3.4   Painting of a moving target in a zig-zag pattern

As in many practical applications, the target has also been considered to move in two directions following a zig-zag pattern, as depicted in Figure 6.10. The initial position of the target plate is located such that the center of the atomizer is displaced at a distance of 15.2 cm from the edge of the target. The ANSYS program was used as a framework in the simulation and proved to be a very powerful tool for generating the data. However, ANSYS only has very rudimentary features for data post-processing, which makes any attempt to visualize the data a very cumbersome task. To overcome this limitation, the raw output data from ANSYS were exported and the data post-processing was performed in MATLAB, which offers a richer set of utilities for graphics handling, such as the contour and surface plots, three-dimensional plotting and volumetric data slicing. The raw output data from ANSYS in many cases exhibit stochastic behavior which is a consequence of using the random walk model in particle trajectories treatment and turbulence modeling in flow simulations. MATLAB offers ways of smoothing and filtering the data. Therefore, a MATLAB code was generated to determine the average deposition thickness on the surface of the moving target. The accretion files, which provide data for the deposition thicknesses, are produced by ANSYS every 0.1 s and then are processed by the MATLAB code. Figure 6.11 shows the deposition pattern for the entire target plate after six complete strokes.

Figure 6.10: 2D pattern of a moving target following a zig-zag pattern

Figure 6.11: 2D deposition thickness in μm after six complete strokes

A comparison between the numerical and the experimental results is presented in Fig.12 across a parallel plane to the y-axis placed at 162cm from the edge. It has been found that

the numerical results show higher peak and valley deposition thickness than the experimental results but generally follow the pattern. This may be due to value of de-rating factor that was assumed.
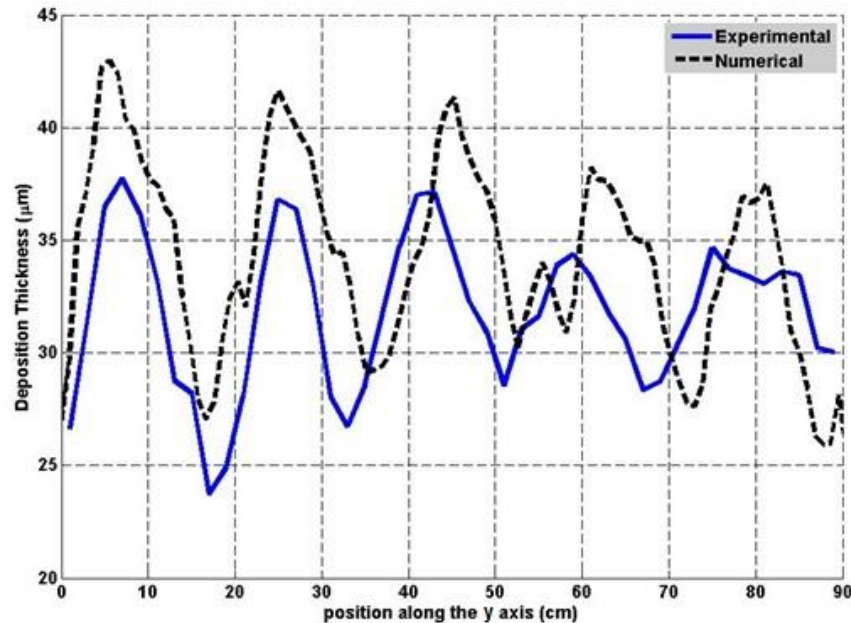
Figure 6.12: Comparison between the numerical and the experimental results of the deposition thickness across a plane at 162 mm from edge

6.4   Conclusions

In this chapter, the numerical results of the particle deposition pattern in the case of a stationary and moving target have been presented. ANSYS, a commercial Finite Volume Method software, was employed for the numerical modeling in 3D. Two injection techniques have been proposed and the model assuming that the charged poly-dispersed particles were injected along three virtual rings placed at a distance of 7 mm from the tip of the atomizer proved to give the best agreement. Different injection angles as well as a variation of the mass fractions were assumed for each ring. It has been found that the injection angles and the percentages of the mass flow strongly affect the deposition profile. The numerical and the experimental results were matched by appropriate selection for a suitable injection pattern. A comparison between the numerical and the experimental results has been presented for two different cases of a moving target in one direction and a

zig-zag pattern. The numerical results showed a reasonable agreement with the experimental results. A supplementary material for the numerical modeling of the electrostatic painting process is presented in Appendix B.

References

[1] H. Osman, K. Adamiak, G.S.P. Castle, H.-T. Fan and J. Simmer, "Comparison between the numerical and experimental deposition patterns for an electrostatic rotary bell sprayer," 2015 IMECE Conference, ASME, accepted for publication, 2015.

[2] J. Domnick, A. Scheibe, Q. Ye, "The simulation of the electrostatic spray painting process with high-speed rotary bell atomizers, Part I: Direct charging," Part.Part.Syst.Charact., vol.22, pp.141-150, 2005.

[3] K. Adamiak, "Numerical investigation of powder trajectories and deposition in tribocharge powder coating," IEEE Trans. Ind. Appl., vol.37, pp.1603-1609, 2001.

[4] K. Adamiak, G.S.P. Castle, I.I. Inculet, and E. Pierz, "Numerical simulation of the electric field distribution in tribo-powder coating of conducting cylindrical objects," IEEE Trans. Ind. Appl., vol.30, pp.215-221, 1994.

[5] Q. Ye, J. Domnick, and A. Scheibe, "Numerical simulation of spray painting in the automotive industry," 1st European Automotive CFD Conference, EACC, pp.195-207, 2003.

[6] D.C. Conner, A. Greenfield, P.N. Atkar, A.A. Rizzi, and H. Choset, "Paint Deposition modeling for trajectory planning on automotive surfaces," IEEE Trans. Autom. Sci. Eng., vol.2, No.4, pp.381-392, 2005.

[7] Q. Ye, "Using dynamic mesh models to simulate electrostatic spray-painting," High Perfom. Comp. Sci. Eng. 5, pp.173-183, 2006.

[8] N. Toljic, K. Adamiak, G.S.P. Castle, H.H. Kuo and C.T. Fan, "3D numerical model of the electrostatic coating process with moving objects using a moving mesh," J. Electrostatics, vol.70, pp.499-504, 2012.

[9] N. Toljic, K. Adamiak, G.S.P. Castle, H.H. Kuo and C.T. Fan, "Incorporating of the corona current into a numerical 3D model of the electrostatic coating process," J. Part. Sci. Techn., vol.30, pp.451-460, 2012.

[10] ANSYS FLUENT User's guide, www.ansys.com

[11] N. Toljic, K. Adamiak, G.S.P. Castle, H.H. Kuo and C.T. Fan, "3D numerical model of the electrostatic coating process with moving objects using a moving mesh," J. Electrostatics, vol.70, pp.499-504, 2012.

Chapter 7

Numerical Study of Particle Deposition in Electrostatic Painting Near a Protrusion or Indentation on a Planar Surface[†]

7.1 Introduction

In electrostatic painting it is desirable to improve the uniformity and finish quality of the coating. Perturbations in the shape of the target to be coated can significantly affect the electric field distribution along its surface and deteriorate coating quality. When the target surface contains some sharp edges and recessed areas, two major problems may occur: the edge effect and the Faraday cage effect. The electric field in close vicinity to the target surface is composed of two components: one created by the high voltage supplied to the atomizer and another, generated by the space charge of the charged paint droplets. As the electric field concentrates at the edges and sharp corners, the deposition of particles will be greatly enhanced in these areas, which may result in uneven distribution and lack of uniformity of paint. In the paint industry this is known as the window-paning or edge effect [2]. However, in powder coating the back corona effect can also occur near the sharp edges leading to reduced deposition thickness.

The Faraday cage effect is a result of the fact that the electric field lines are shielded and restricted from penetration into indentations. Because the charged particle trajectories tend to follow the electric field lines, fewer particles may enter the area of indentation and this leads to the possibility of less coating. Numerical modeling of the electrostatic spraying process has been used by a number of researchers, but few have investigated these particular phenomena and suggested some approaches to minimize them.

Adamiak et al. [3] studied numerically the electrical conditions in tribo-powder coating of 2D cylindrical objects using the Charge Simulation Method. They investigated the problem of quick corrosion of car wheel edges and confirmed that pin holes in the paint

---

[†] This work has been accepted for publication [1].

coating resulting from back corona discharge was responsible for this. It has been suggested that the charge-to-mass ratio of the powder should be reduced, as the space charge is the only source of the electric field in this configuration. Chen et al. [4] studied the transfer efficiency models for the electrostatic powder coating process. They considered air with a relatively high velocity containing coarser paint particles to provide a better Faraday cage penetration, if the particle charge and electric field are well-controlled. Adamiak [5,6] investigated uniformity of the powder deposition in the tribo-charging powder coating system along different targets assuming mono- and poly-dispersed powder particles, and tracing their trajectories. He found that for large particle diameters and small charge-to-mass ratio, more particles penetrated and were deposited inside the cavity, whereas smaller particles were attracted to the corners, as the charge-to-mass ratio increased. Biris et al. [7] developed a novel charger to charge two kinds of powder particles bipolarly such that the net charge-to-mass ratio is close to zero. They concluded that to overcome the Faraday cage effect and to have a uniform deposition thickness, the charge-to-mass ratio must be reduced. Also, Biris et al. discussed in [8] how the Faraday cage shielding affects the uniformity and hence the corrosion resistance of the powder coating using a corona gun. Takeuchi [9] investigated the charging characteristics of an electrostatic powder coating system. His measurements showed that the charge-to-mass ratio of coating powders deposited on the target was larger than that of undeposited particles for both corona and tribocharging spray guns. The charge-to-mass ratio of the coating powders was increased by adding a pair of auxiliary electrodes in the space between the corona spray gun and the Faraday cage. Free ions from the corona charging spray gun, which caused the back ionization and spoil the coating quality, were decreased by applying a magnetic field in the spraying space.

Considering an industrial electrostatic liquid painting system, Toljic et al. [10] succeeded in creating a full 3D numerical model of the electrostatic coating process for a moving target using the commercial CFD program FLUENT. They assumed a conduction mechanism for particle charging and the simulated target plate took the shape of a car door, assuming a specified hole on the surface of the plate for the handle. They considered motion of the target in two directions following a zig-zag pattern. Their numerical results showed some improvements in the thickness uniformity compared with the stationary target, but

the deposition around the door handle was at higher level due to the edge effect. Domnick et al. [11] also presented a numerical model of the electrostatic spray painting system using a rotary bell atomizer with six external corona needles, which were arranged symmetrically around the atomizer body. They chose the target geometry as a rear part of a car body. They compared their numerical and experimental results of the deposition thickness at the edges of the target and above the inclined panel. Their simulation results were in a good agreement with the measured ones except at the positions very close to the edges, where the simulated deposition thickness was overestimated.

Although the commercial programs to solve the mechanical and electrical parts of the electrostatic coating process have been developed, the understanding of the phenomena of the edge effect and the Faraday cage effect for complicated target geometries has not been modeled extensively and warrants more investigation. In the first part of this chapter, we discuss a numerical model using COMSOL commercial software to simulate the electric field distribution on a grounded target plate, which includes either a small protrusion or indentation at the center. The electric field for different values of the radius and the height of the protrusion (or the depth of the indentation), the radius of the corner and the space charge existing between the high voltage and ground electrodes was calculated. The second part of the chapter presents another numerical model using ANSYS commercial software to investigate the effect of the particle size and the charge-to-mass ratio on the uniformity of the coating buildup rate on a flat target and a target with an indentation or a protrusion. Several different model parameters, such as the size of the particles, the charge-to-mass ratio, the size of the surface perturbation and the radius of the corner, were considered in this study and the relationship between the electric field patterns and coating thickness are discussed.

7.2   Mathematical model

The electric field, generated by the applied voltage and the space charge formed by the charged particles and ions, is governed by Poisson's equation

$$\nabla^2 \phi = -\frac{\rho}{\varepsilon} \tag{7.1}$$

where ϕ is the scalar electric potential, ρ is the total space charge density and ε is the electric permittivity. The Finite Element Method is used to solve the Poisson's equation to obtain the electric potential in the whole computational domain, and then the vectors of the electric field can be determined as the gradient of the electric potential

$$E = -\nabla \phi \tag{7.2}$$

The target is assumed to be a conductive grounded electrode so that its surface remains equipotential. The total current density J in the steady state must satisfy the continuity equation

$$\nabla \cdot J = 0 \tag{7.3}$$

The injected particles move with an initial velocity, which is equal to the velocity of the assisting air. They begin to diverge after leaving the gun due to the different forces, which will affect their trajectories, including the electrical, drag, gravitational and inertial forces. The particle trajectories can be found by solving the equations of motion, which results from a balance of all considered forces

$$m\frac{dv}{dt} + F_d + F_g + F_e = 0 \tag{7.4}$$

where v is the particle velocity, F_d is the drag force, F_g is the gravitational force and F_e is the electrostatic force defined as

$$F_e = qE \tag{7.5}$$

For the particle sizes of interest the gravitational force may be neglected. Hence, the drag force as well as both the particle charge and local electric field strength are the important factors that control and determine the particle trajectory and the resulting deposition thickness.

7.3 Numerical model

COMSOL, a Finite Element commercial software [12], was employed to determine the electric field in a 2D model of the problem. The stationary model, as depicted in Figure

7.1a, consists of a grounded electrode having a circular disc shape located 25 cm from a circular high voltage electrode, supplied with a voltage equal to 90 kV. Both electrodes were assumed to have equal radii of 50 cm. A small circular perturbation of radius r_p and height h exists at the center. A positive value of h represents a protrusion and a negative value an indentation. A very fine mesh was generated near the corners of radius r_c. The electric field over the entire grounded electrode was simulated for different sizes of the perturbations and corner radii. The space charge between the two electrodes was also considered in the simulation by assuming three different charge densities of 0, 1 and 10 $\mu C/m^3$.

For the deposition study, ANSYS, a Computational Fluid Dynamic (CFD) commercial software [13], was employed to simulate the particle trajectories and estimate the coating buildup rate on a stationary flat target and a target with a surface perturbation. The model was also used to investigate the effect of the particle size as well as the charge-to-mass ratio on the deposited paint thickness. The computational domain was created and meshed in an unstructured manner using the mesh generation tool within the ICEM package. The mesh consisted of about 500,000 elements and was very fine near the area of perturbation using tetrahedral elements of 120 μm side length, which was graded to much coarser elsewhere. User Defined Functions (UDFs) were used to solve Poisson's equation and the charge continuity equation. Coupling between the continuous phase (shaping air) and the discrete phase (charged particles) was included via source terms of mass and momentum. A schematic diagram of the model in the 2D domain is shown in Figure 7.1b, which includes a circular grounded target plate of radius 50 cm placed at a distance of 25 cm from a cylindrical atomizer of radius 5 cm, which was 20 cm long.

The applied voltage at the tip of the atomizer was set to 90 kV and the injected particles were assumed charged by the conduction mechanism, since that the conductivity of the injected particles were assumed to be high. The entrained air velocity magnitude was 5 m/s in a direction perpendicular to the target surface and it is operated in the laminar mode. The corner radius, depth of the indentation as well as the height of the protrusion were varied. A uniformly distributed particle injection pattern was introduced from 5000 injection points at the outlet of the atomizer. The injection pattern was designed to inject either

mono- or poly-dispersed particles under two separate conditions of charged and uncharged cases.
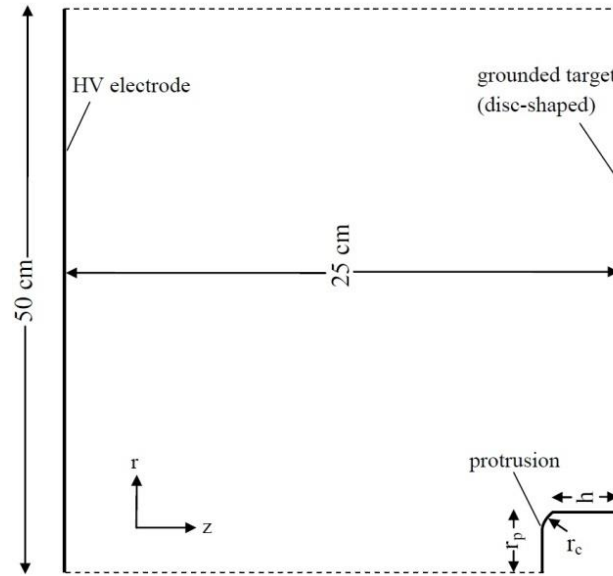
(a) Electrostatic field model, COMSOL
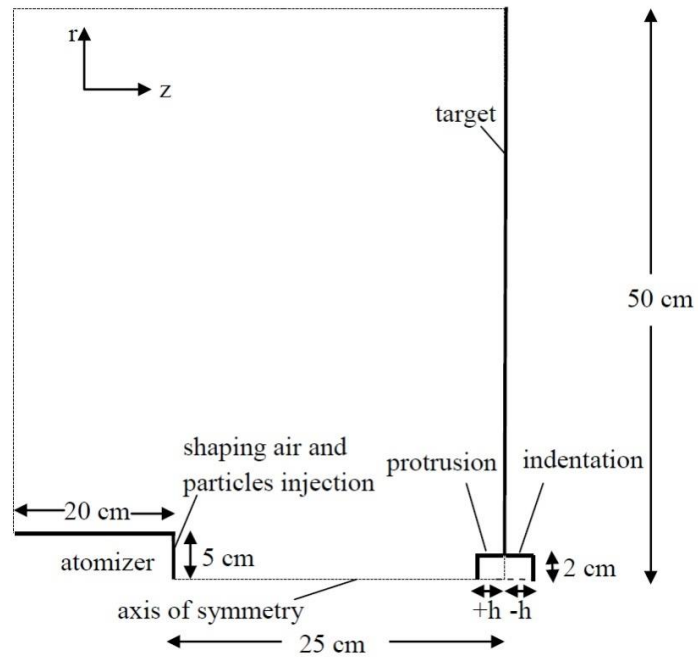
(b) Fluid dynamic model, ANSYS

Figure 7.1: Schematic diagram of 2D axisymmetric model

7.4   Results and discussion

7.4.1   Electric field distribution on the target with surface perturbation

The simulation results of the electric field distribution for a target with a protrusion at the center, assuming different heights and radii have been obtained using COMSOL. The radius of the protrusion corner and the space charge density were also varied. Table 7.1 gives the numerical values of the model parameters used in the simulations. Figure 7.2 shows the calculated electric field distribution for three different protrusion radii. In this and subsequent figures the electric field and the coating buildup rate are defined along a line tracing the entire surface of the target described as "arc length". As shown in the figures the arc length is identified in terms of "regions" to differentiate the perturbation from the flat surface. The normalized field distribution, which is the calculated field values divided by the ambient uniform field, was obtained along the arc length for different parameters of the system.

It was noticed that the maximum electric field occurs at the corner (Region II), where the radius of the corner and the protrusion height were kept fixed to 1 mm and 2 cm, respectively. Figure 7.2 shows that the electric field at the corner was found to approach a value of more than five times greater than the ambient value and slightly decreases, as the radius of the protrusion increases. Also, the value of the electric field at the center decreases to approach the value of the ambient field with increasing the radius of the protrusion, but it increases rapidly along the flat-top surface (Region I) for smaller values of r_p, as the arc length approaches the corner. As a result, varying the protrusion radius affects the field values at the corner (Region II) and increasing the area of the top surface of the protrusion (Region I) reduces the calculated field value to be very close to the ambient field in this region. However, the shielding of the field due to the protrusion (Region III) is similar every time the protrusion radius changes. The field value decreases along the arc length from the maximum at the upper corner to approach the minimum value at the lower corner (zero in this case) and then increases rapidly to equal the ambient field value (Region IV), as shown in Figure 7.2. Figure 7.3 shows the normalized field distribution, where the height of the protrusion was set to three different values and the other model parameters were kept

fixed. The simulation results show that the maximum electric field still occurs at the corner (Region II) and it is four times greater than the ambient field value, as the height increases to reach 2 cm. The results also show that the difference between the field at the protrusion top (Region I) and the ambient field slightly increases with increasing the protrusion height. Therefore, the field at the top surface and the corner are both influenced by the protrusion height.

Table 7.1: Numerical values of the model parameters used in COMSOL simulation

Model parameter	Numerical value
distance between electrodes	25 cm
radius of the electrode (R)	50 cm
applied voltage	-90 kV
Height of protrusion (h)	0.5, 1 and 2 cm
radius of protrusion (r_p)	2, 10 and 20 cm
radius of the protrusion corner (r_c)	0.1, 0.5, 1 and 5 mm
space charge (ρ)	0, 1 and 10 $\mu C/m^3$
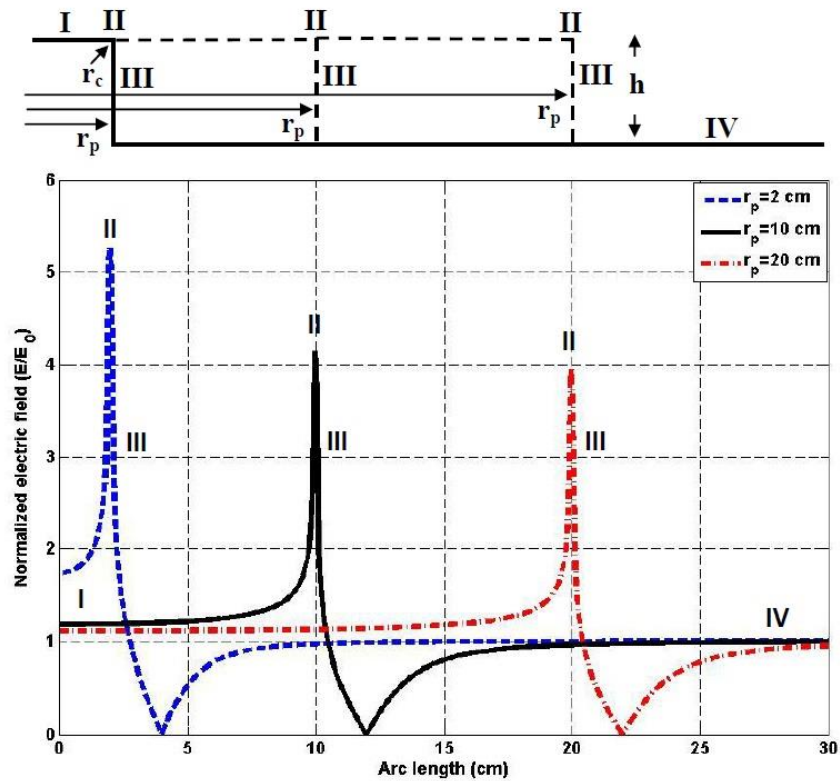
Figure 7.2: Normalized electric field distribution for three different protrusion radii (r_c=1 mm and h=2 cm)

Also, the shielding effect due to protrusion in this case (Region III) can be reduced with decreasing the height and in Region IV the field values are equal the ambient field value, as shown in Figure 7.3.

The electric field has also been calculated for different values of the corner radius, while the other parameters were kept fixed. Figure 7.4 shows that the value of the electric field near the corner (Region II) increases significantly, as the corner radius decreases, but the field values away from the protrusion (Region IV) remain unchanged and equal to the ambient field. Also, it was noticed that all the electric field levels at the top surface (Region I) are slightly higher than the ambient field level and the shielding effect (Region III) does not change with the corner radius. Therefore, the degree of curvature of the corner is a very important parameter as it significantly affects the electric field at the corner and that may cause the edge effect, as shown in Figure 7.4.
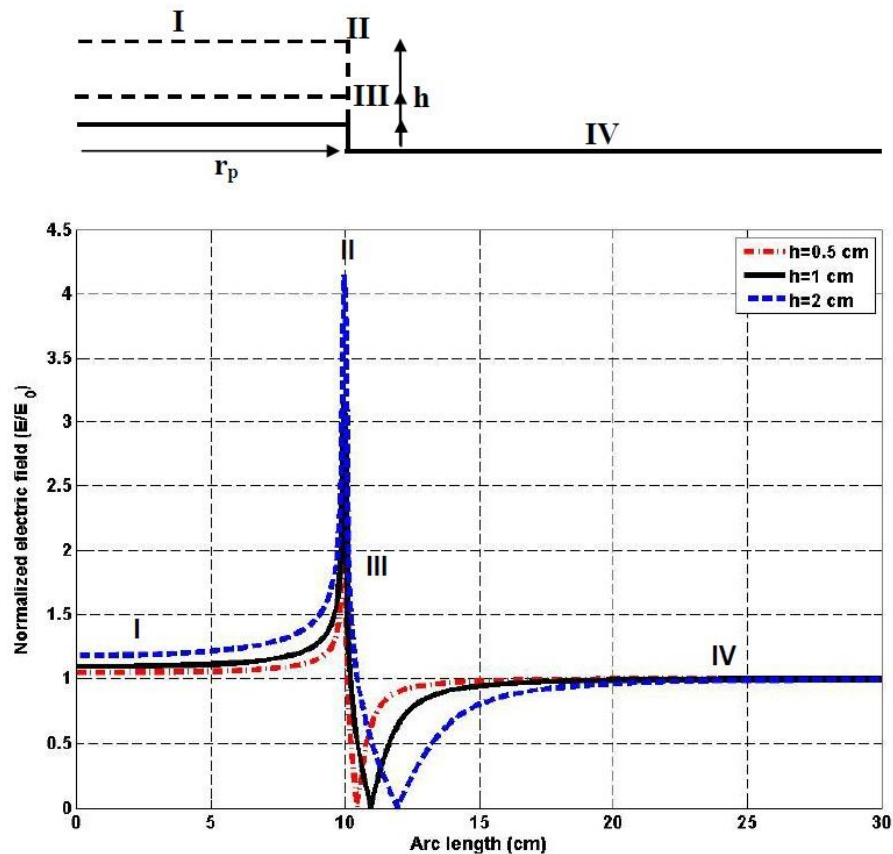
Figure 7.3: Normalized electric field distribution for three different protrusion heights (r_c=1 mm and r_p=10 cm)
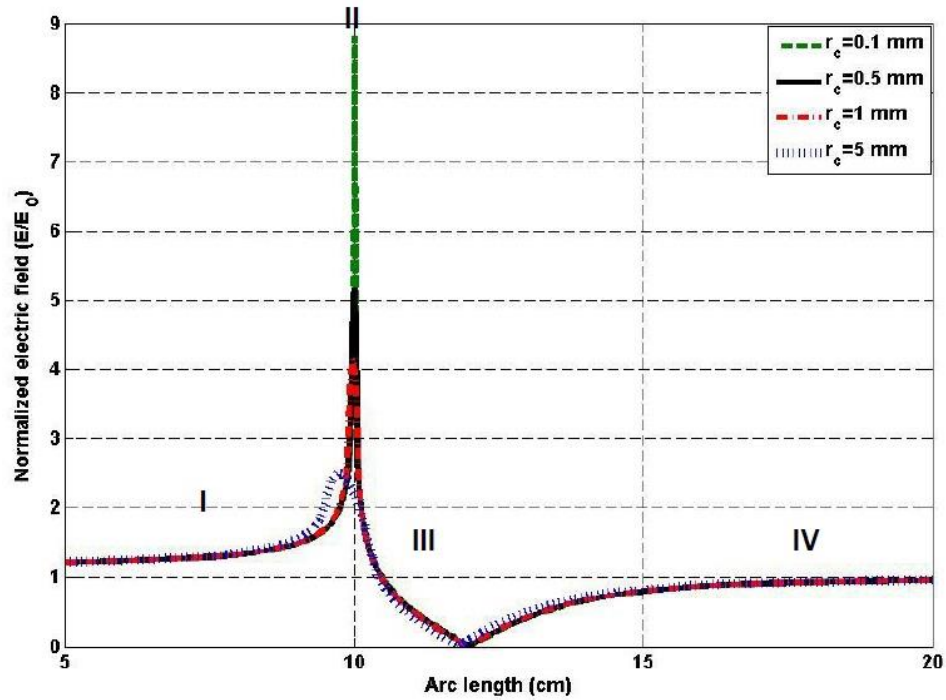
Figure 7.4: Normalized electric field distribution for different corner radii (r_p=10 cm and h=2 cm)

The effect of the space charge on the field distribution is illustrated in Figure 7.5, where three different charge levels were assumed with 90 kV applied voltage. It was noticed that the electric field over the target surface is proportional to the space charge density. So, the total space charge density must be low in order to reduce the electric field at the corner for better uniformity of coating thickness.

As a conclusion, the simulation results show that the electric field distribution along the surface of the target with a single protrusion at the center is non-uniform and its distribution depends on the model parameters. The edge effect, which shows an increased electric field at the corner, is influenced by the radius and height of the protrusion, and more strongly by the radius of the corner. Also, the shielding of the field lines due to the protrusion can be reduced by decreasing its height. The radius of the protrusion has less significant effect on either the field values at the bottom surface of the protrusion or the electric shielding effect, but it affects the electric field value at the top.
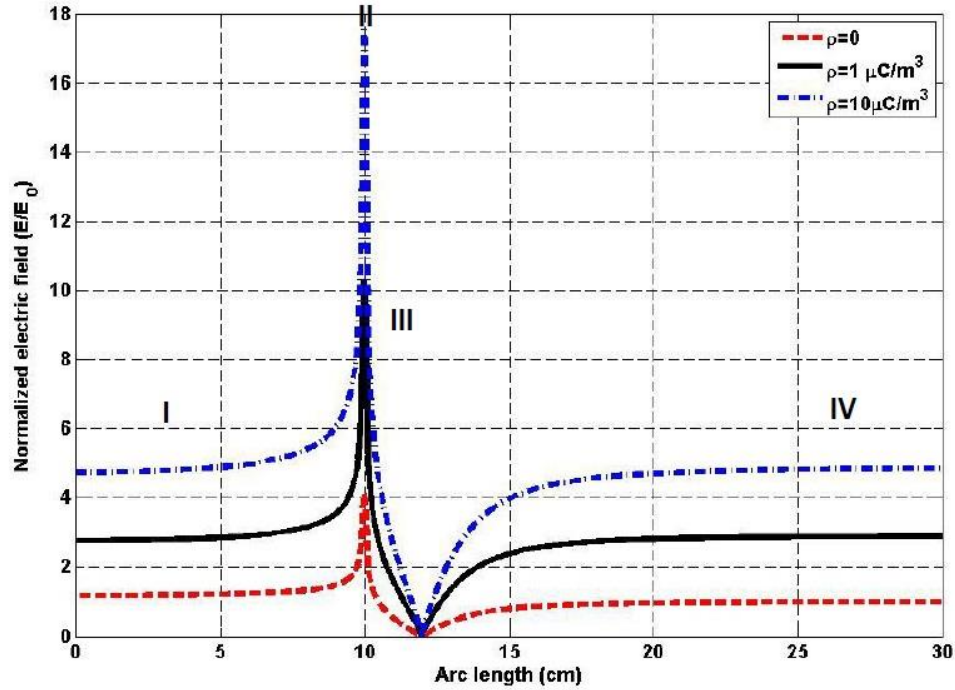
Figure 7.5: Normalized electric field distribution for different space charge density levels

(r_c=1 mm, r_p=10 cm and h=2 cm)

Similarly, when the target geometry was modified by replacing the protrusion with an indentation of the same size, the numerical results were very consistent with the previous results except that the value of the electric field at the corner (Region III) slightly increases with increasing the radius of the indentation (Figure 7.6). It has also been found that the electric field strength significantly increases inside the indentation, Region I, (i.e. reducing the Faraday cage effect), as the area of the bottom is increased. In region II, the electric field value for different radii increases dramatically from zero at the lower corner to the maximum, as the arc length approaches the upper corner and then decreases to equal the ambient field value at the top surface of the indentation (Region IV), as shown in Figure 7.6. By comparing the electric field value at the corner of the protrusion and indentation, where the corner radius, the protrusion and indentation area are equal (i.e. $r_p = r_i$ and $h = -h$), it was noticed that the edge effect in the case of the indentation is less significant than in the case of the protrusion due to circular symmetry, as shown in Figures 7.2 and 7.6.
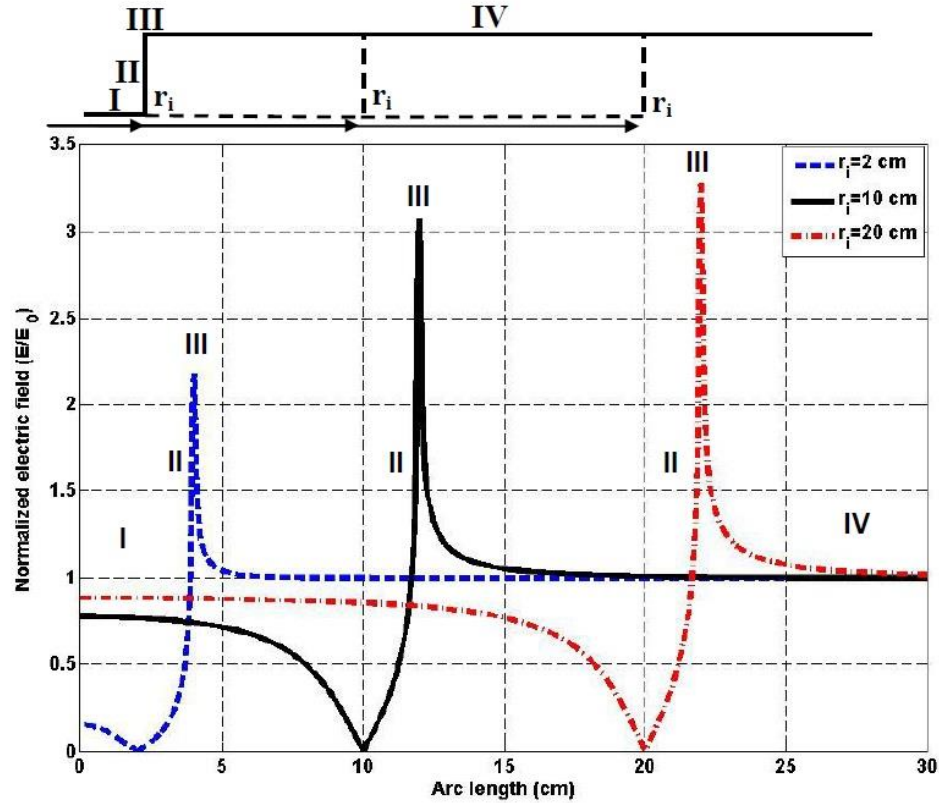
Figure 7.6: Normalized electric field distribution for different indentation radii (r_c=1 mm and h=-2 cm)

In addition, the depth of the indentation has a significant impact on the Faraday cage penetration problem. Increasing the indentation depth will significantly decrease the field values inside the indented area (Region I) and this increases the electric shielding of the field, as shown in Figure 7.7. Therefore, it is expected that fewer particles have the chance to be deposited inside the indentation due to electrostatic forces, which are less dominant than the aerodynamic force. Also, the concentration of the electric field at the corner (Region III) decreases for smaller values of h, but the field value increases more quickly in Region II from the zero level at the lower corner to the maximum as the arc length approaches the corner. In Region IV the values of the electric field do not change and are equal to the ambient field. Therefore, the electric field value at the corner depends on the radius of the corner as well as the indentation radius and depth. The Faraday cage effect can be controlled by either the radius or the depth of the indentation. In general, the uniformity of the electric field distribution over the perturbed target surface is directly

affected by the level of the space charge density presented in the model. Table 7.2 summarizes the effects of each model parameter of the surface perturbation on the electric field distribution.
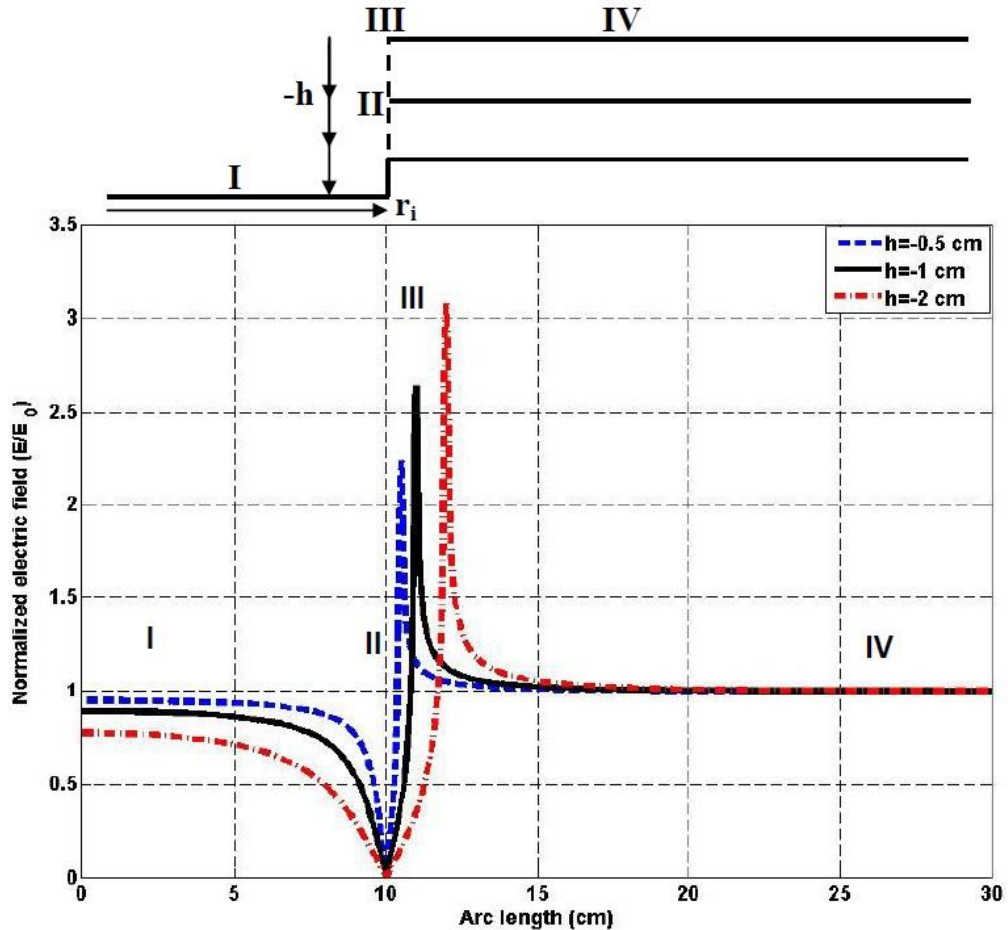
Figure 7.7: Normalized electric field distribution for different indentation depths ($r_c=1$ mm and $r_i=10$ cm)

The next sections present simulation results for the particle deposition thickness on a surface with perturbation, where the model of a protrusion and an indentation are also considered separately, in order to examine the correlation between the distribution of the electric field and the deposition pattern in each configuration so that the coating thickness for a complicated surface geometry can be predicted via calculating the field values. The goal is to determine if it is possible to speed up the computation process and minimize the

complexity of the numerical model for simulation.

Table 7.2: Summary for the effects of the model parameters on the electric field distribution

Configuration	Model parameter	Observations
protrusion	radius (r_p)	• affects the electric field at the corner and at the top surface
	height (h)	• affects the electric field at the corner and at the top surface • affects the electric shielding of the field
	radius of the corner (r_c)	• strongly affects the electric field at the corner
	space charge	• proportional to the electric field and affects the uniformity of the electric field
indentation	radius (r_i)	• affects the electric field at the corner and inside the indentation
	depth $(-h)$	• affects the electric field at the corner and inside the indentation
	radius of the corner (r_c)	• strongly affects the electric field at the corner
	space charge	• proportional to the electric field and affects the uniformity of the electric field

7.4.2   The coating buildup rate of monodispersed particles

A 2D axisymmetric model was created using ANSYS to investigate the effect of the particle size and the charge-to-mass ratio on the coating buildup rate of a perturbed grounded target surface. It was assumed that mono-sized particles with four different diameters of 10, 20, 35 and 70 μm were injected from the outlet of a cylindrical atomizer, which is placed 25 cm away from a circular target plate, as previously shown in Figure 7.1b. Table 7.3 illustrates the numerical values of the model parameters used in the simulation of this part.

Assuming that the air velocity magnitude at the outlet is 5 m/s, the distribution of air flow for the three target configurations is different, especially at the center. The direction of the air flow is perpendicular to the target surface and it then changes to a parallel direction

when approaching the target surface. For a flat target plate the results of the air flow pattern in Figure 7.8a show that the central part of the target surface has the lowest air velocity magnitude, i.e. a "dead zone", and increases in the radial direction to approach a steady state value of around 2 m/s.

Table 7.3: Numerical values of the model parameters used for ANSYS painting model

Model parameter	Numerical value
radius of the target plate	50 cm
radius of the atomizer	5 cm
indentation or protrusion radius	2 cm
depth of indentation or height of protrusion	0.5, 1 and 2 cm
total number of injection points	5000
distance between gun and target	25 cm
initial axial particle velocity	10 m/s
airflow velocity magnitude at the gun outlet	5 m/s
applied voltage	-90 kV

When the protrusion is introduced, the air velocity becomes very low in the shadow of the protrusion height, as shown in Figure 7.8b, and an air vortex can be created, which, in turn, will strongly affect the particle deposition in this area. Also, Figure 7.8c shows that a stationary air vortex is formed inside the indentation "dead zone", seen as the closed streamlines of the air flow, which will force most of the injected small particles to be deflected and deposited outside. In order to study the surface deposition pattern, a uniform spatial mass injection of particles was assumed. To achieve this in the axisymmetrical computational model, the mass flow at radius r was assumed to be a linear function of the radial distance.

$$\dot{M} = \dot{m}_0 \left(\frac{r}{R} \right) \tag{7.6}$$

where $\dot{m}_0$ is a constant related to the overall flow rate of each particle size in g/s and R is the radius of the atomizer. The charge-to-mass ratio was calculated approximately such that it is inversely proportional to the square of the particle diameter [14]

$$\frac{q}{m} = \frac{4k_0}{D^2} \tag{7.7}$$

where D is the particle diameter in μm and k_0 is a constant determined such that the absolute charge-to-mass ratio for a 35 μm particle diameter is 1 mC/kg. Table 7.4 shows the particle size distribution, which was based upon measured values from a typical practical process that was performed in a previous GM research project [15].
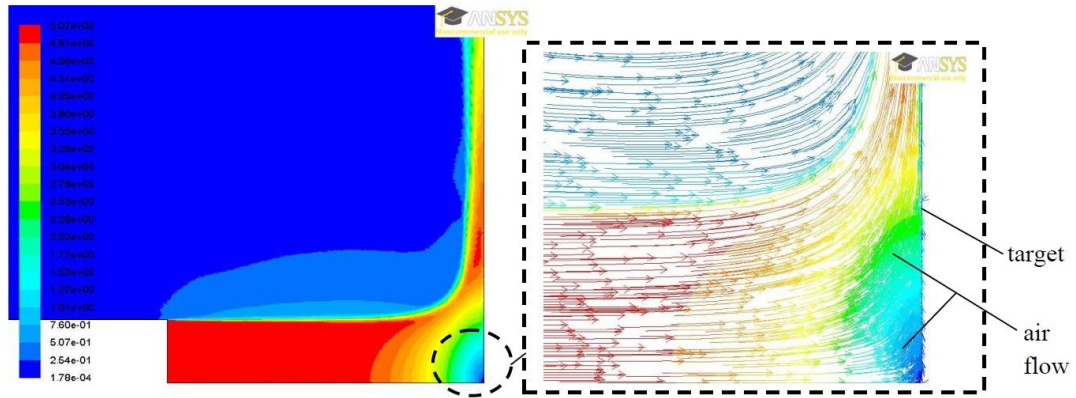
(a) Flat target
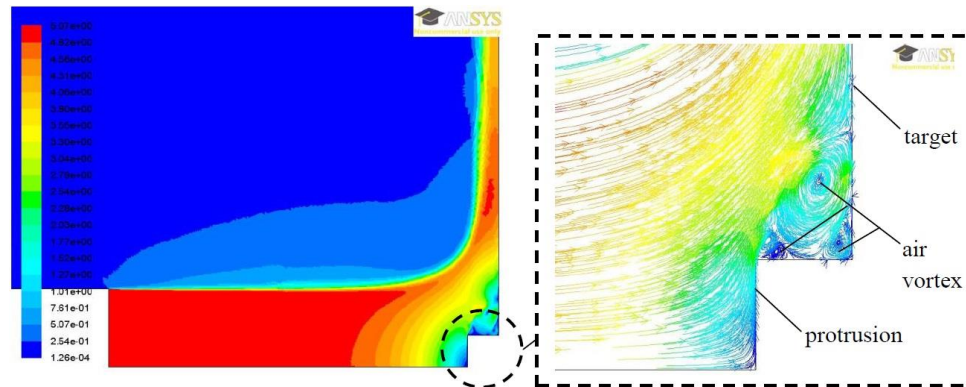
(b) Target with a protrusion
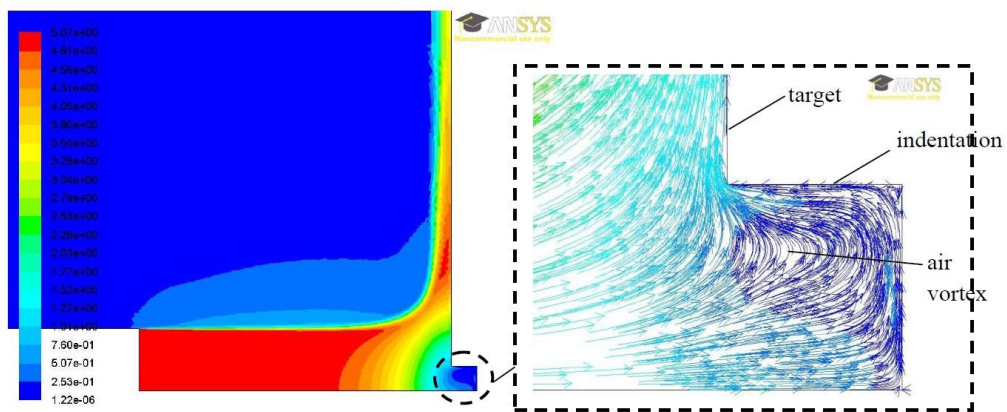
(c) Target with an indentation

Figure 7.8: Streamlines of air flow pattern

Table 7.4: Distribution of particle size and charge-to-mass ratio

Band	Particle diameter D (μm)	Mass flow rate (g/s)	Charge-to-mass ratio q/m (mC/kg)
1	10	0.0165	-12.25
2	15	0.0825	-5.44
3	20	0.198	-3.0625
4	25	0.33	-1.96
5	30	0.462	-1.36
6	35	0.495	-1
7	40	0.4455	-0.766
8	45	0.3234	-0.6
9	50	0.2475	-0.49
10	55	0.2145	-0.4
11	60	0.132	-0.34
12	65	0.1023	-0.29
13	70	0.0924	-0.25
14	75	0.0825	-0.22
15	80	0.0759	-0.19

The mass distribution has been modified to have a total mass flow rate of 3.3 g/s and the charge-to-mass ratio was calculated from Eq.(7.7).

First, the simulation results of the coating buildup rate on a flat target have been obtained for the cases of the uncharged and charged monodispersed particles. In order to see the relative differences between particle sizes, the coating buildup rate corresponding to a selected particle size P has been normalized with respect to the coating buildup rate of 35 μm diameter particles such that

$$\text{(Normalized coating buildup rate)}_P = \text{Calculated buildup rate} \times \frac{\dot{M}_{35\mu m}}{\dot{M}_P} \qquad (7.8)$$

where $\dot{M}_{35\mu m}$ and $\dot{M}_P$ are the mass flow rate for particle of 35 μm diameter and a selected particle diameter P, respectively.

When the uncharged particles are injected, smaller particles are more sensitive to the air drag force, which deflects them in the radial direction. Half of these particles are eventually deposited and usually it happens at greater distances from the center, while the other half escape and are not deposited. Larger particles of 35 and 70 μm diameter are mostly deposited close to the center and less dispersed in the radial direction with transfer efficiency equal to 100%. The transfer efficiency for the monodispersed particles is calculated as a ratio of the total number of deposited particles to the total number of particles injected from the atomizer. Figure 7.9 shows that the normalized buildup rate for injecting the smaller charged particles is more uniform at the central part of a planar target (i.e. inside the spray cone distance from 0 to 5 cm) and then decreases to reach zero thickness at very large distance (> 25 cm). Also, an increased dispersion in the radial direction for the smallest particles is noticed.

Since the electric force for small particles has been increased, an increased number of deposited particles at the center and 100% transfer efficiency is obtained.
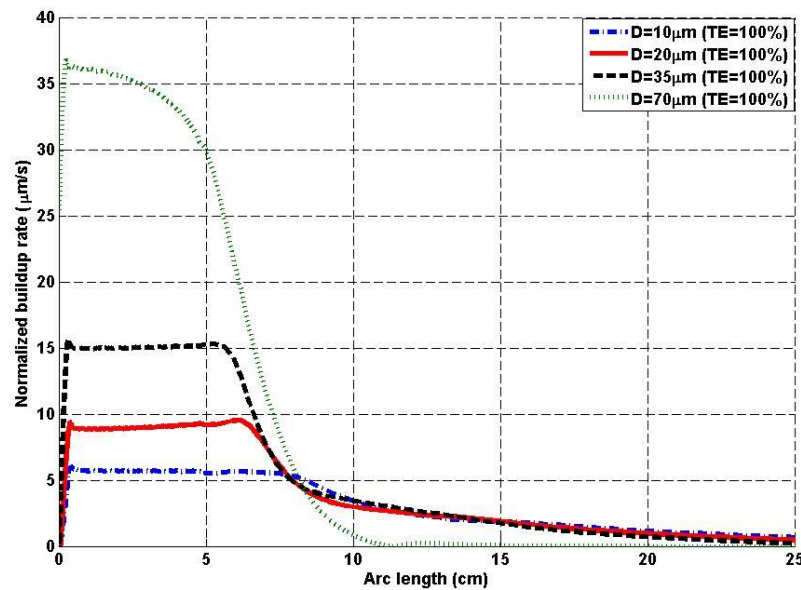
Figure 7.9: Normalized buildup rate on a flat target for different charged particle diameters

A small circular protrusion is introduced at the center of the target, such that its radius is equal to 2 cm, three values of the protrusion height are: 2, 1 and 0.5 cm, and the radius of the corner is 100 μm. For the case of the uncharged particles different buildup rates for the different particle sizes at the top surface of the protrusion was observed and no deposition on the side wall of the protrusion for particles of 10 and 20 μm diameter, because all these particles were strongly deflected by the air vortices in this area. However, larger particles of 35 and 70 μm diameter have some deposition in this region. Figure 7.10 shows the effect of injecting charged particles and the results demonstrate more uniform distribution of the coating buildup rate on the top surface of the protrusion (Region I) than the side wall of the protrusion (Region III), which displays poor deposition of particles due to the shielding of the field. Because the electric field in Region I is relatively higher than in the case of a flat target, it is expected to see more particle deposition in this region (Figures 7.9 and 7.10).
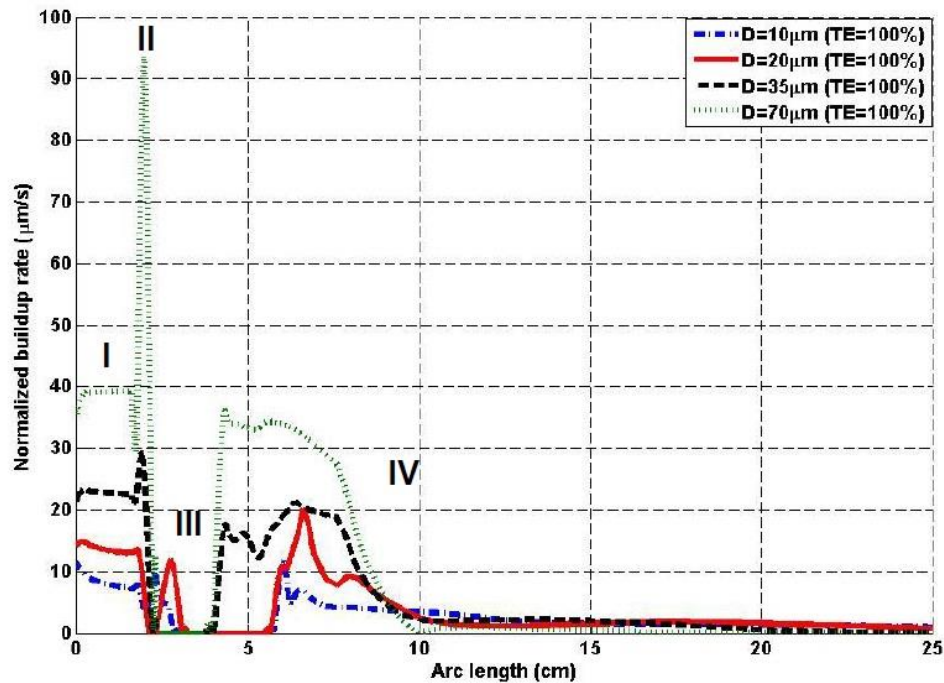
Figure 7.10: Normalized buildup rate along a target surface with a protrusion of 2 cm height at the center for different charged particle diameters

Also, the results reveal a very high buildup rate at the corner (Region II) for larger particles (35 and 70 μm), where the concentration of the electric field is highest, as previously

described in Section 7.4.1. Although the highest charge-to-mass ratios were assumed for the small particles, the aerodynamic force acting on these particles was greater than the electric force of attraction towards the corner. If the protrusion height decreases to 1 and then 0.5 cm, the concentration of the electric field at the corner decreases, as previously shown in Figure 7.3. This leads to a reduction of the total number of the charged particles deposited at the corner (Region II) and the coating buildup rate in Regions I and IV becomes more uniform.

Also, it was found that the buildup rate decreases in Region I in the case of 0.5 cm height than in the cases of 2 and 1 cm height, since in this region the electric field value slightly decreases with decreasing the protrusion height, as shown in Figure 7.11. The simulation results of this case also show more deposition of 10 μm particle diameter in Region III than in the case if 2 cm height, as the electric shielding of the field is reduced. Therefore, decreasing the protrusion height will reduce the edge effect at the corner and slightly increase the penetration of small particles to reach the side wall of the protrusion. The coating buildup rate at the center can be also improved to become more uniform.
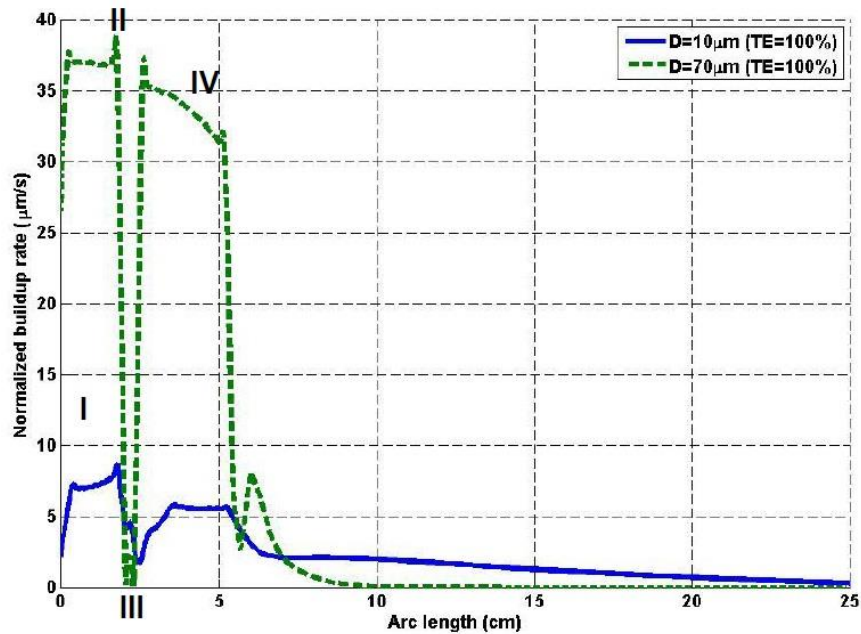
Figure 7.11: Normalized buildup rate along a target surface with a protrusion of 0.5 cm height at the center for two charged particle diameters

The normalized buildup rate has also been examined for a target with an indentation at the center of the same size as in the case of a target with a protrusion, such that its radius is equal to 2 cm and three values of the indentation depth are: 2, 1 and 0.5 cm. The simulation results for the case of the uncharged small particles show no deposition at the bottom of the indentation and on the side wall. Most of these particles will be strongly influenced by the air vortex (Figure 7.8c) and are entrained away from the indentation area. Figure 7.12 shows the thickness uniformity of paint and the transfer efficiency for charged particles. In this case, some deposition at the bottom of the indentation (Region I), which faces the atomizer, can be observed for all particle sizes. If the injected particles are relatively large (35 and 70 µm), the normalized buildup rate in this region is very similar to the results of a flat target configuration. Also, small particles are strongly entrained by the air vortices from inside the indentation and it is expected to have a thinner coating layer at this region. Figure 7.12 also shows that more small particles have the chance to be deposited at the side wall of the indentation (Region II), as the charge-to-mass ratio increases. The high concentration of the charged particles at the edge (Region III) in this case is less pronounced than in the case of the protrusion, as previously described in Section 7.4.1.
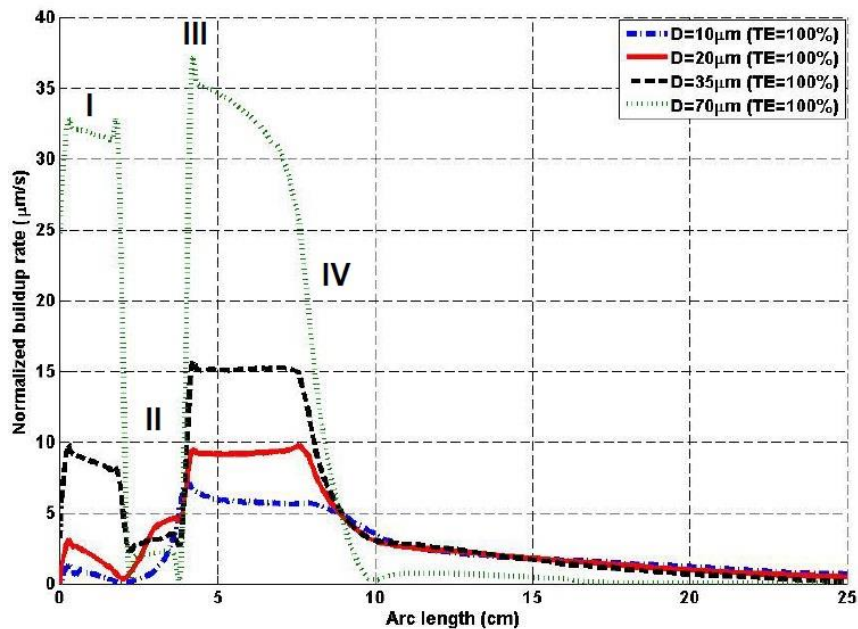
Figure 7.12: Normalized buildup rate along a target surface with an indentation of 2 cm depth at the center for different charged particle diameters

Shrinking the indentation depth reduces the effect of air vortices and increases the possibility of all particles, small particles in particular, to be deposited inside the indentation. Two cases of 10 and 70 µm particle diameters were tested for two indentation depths of 1 and 0.5 cm. The results in the case of 0.5 cm depth show that the coating buildup rate increases slightly at the center (Region I) for both particle sizes compared with the cases of 2 and 1 cm depth, as shown in Figure 7.13, since the shielding of the field will be reduced and more particles can penetrate inside the indentation. Therefore, decreasing the indentation depth can improve the deposition at the center and it becomes more uniform. In Region IV, the normalized buildup rates for all particle sizes are similar to the case of a flat target. These results confirm that the depth of the indentation, the size of injected particles and the charge-to-mass ratio are all important factors, which can control the degree of deposition uniformity and reduce the Faraday cage effect.
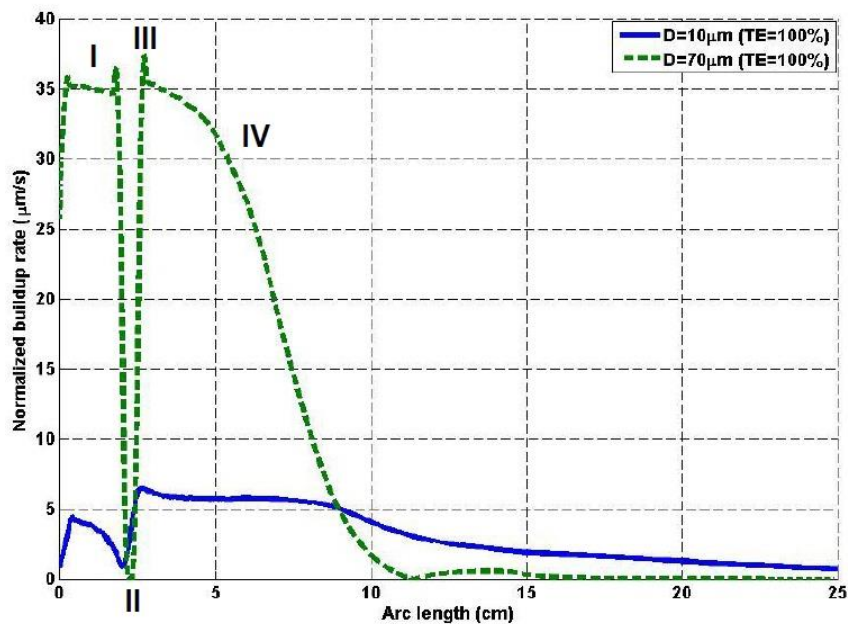
Figure 7.13: Normalized buildup rate along a target surface with an indentation of 0.5 cm depth at the center for two charged particle diameters

7.4.3   The coating buildup rate of polydispersed particles

For polydispersed particles, the particle size distribution was approximated by 15 size-bands, in which the band of 35 µm particle diameter has the maximum mass flow rate and

a charge-to-mass ratio of -1 mC/kg, as shown earlier in Table 7.4. A spatially uniform mass injection of polydispersed particles was assumed (Eq.(4.6)), where the total mass flow rate was equal to 3.3 g/s. The charge-to-mass ratio is inversely proportional to the square of the particle diameter (Eq.(4.7)), where $k_0=0.3\times10^{-12}$ m^{2}C/kg.

Similarly to the previous discussion of the monodispersed particles, three target configurations were investigated: a flat target, a target with a protrusion and target with an indentation. The trajectories of the charged particles were obtained for three target configurations and the results show that the larger particles are more concentrated at the central part of the target than the smaller ones, which are more susceptible to spread over a large area outside the spray cone, as shown in Figure 7.14. The injection of a large number of very fine particles increases the total number of particles, which escape from the computational domain, and this, in turn, will decrease the transfer efficiency. The coating buildup rate on a flat target for charged and uncharged polydispersed particles have been compared. For the charged particles a more uniform distribution was noticed at the central part of the target surface with higher transfer efficiency compared with the uncharged particles. The distribution of the charged particles on the surface is also wider than the distribution of the uncharged ones. As the small particles spread more widely over the target surface, the charged large particles are influenced strongly by the electric force of attraction to be distributed uniformly around the center of the target.

As shown in Figure 7.15, if the target includes a protrusion of 2 cm at the center, an increased thickness of charged particles at the upper corner (Region II) of the protrusion was observed, as expected due to the high concentration of the electric field in this region. Since the electric field at the flat-top (Region I) is larger than the ambient field, as previously shown in Section 7.4.1, it is expected to have higher coating buildup rate than in the case of a flat target. The results also show no particle deposition on the side wall (Region III) and the distribution of the buildup rate at the bottom surface (Region IV) is less uniform.
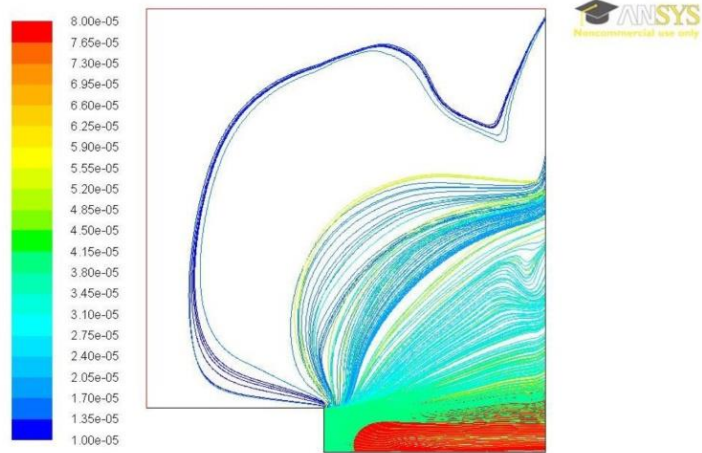
(a) Flat target
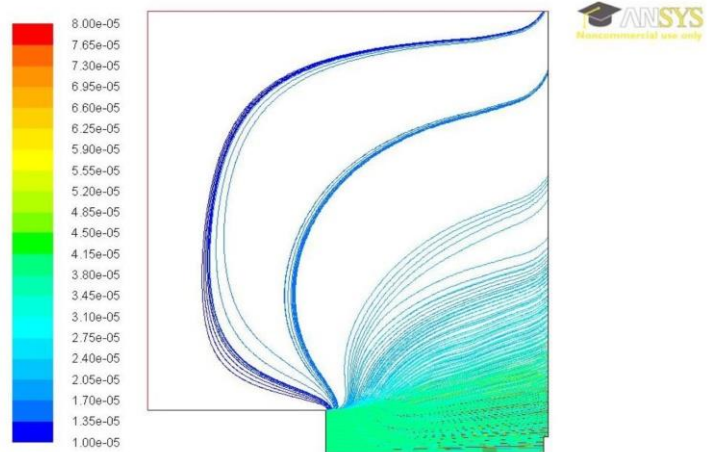
(b) Target with a small protrusion
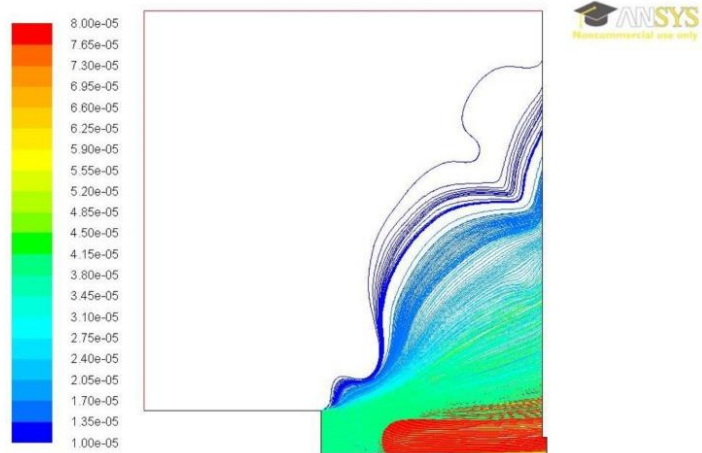
(c) Target with a small indentation

Figure 7.14: Trajectories of charged polydispersed particles
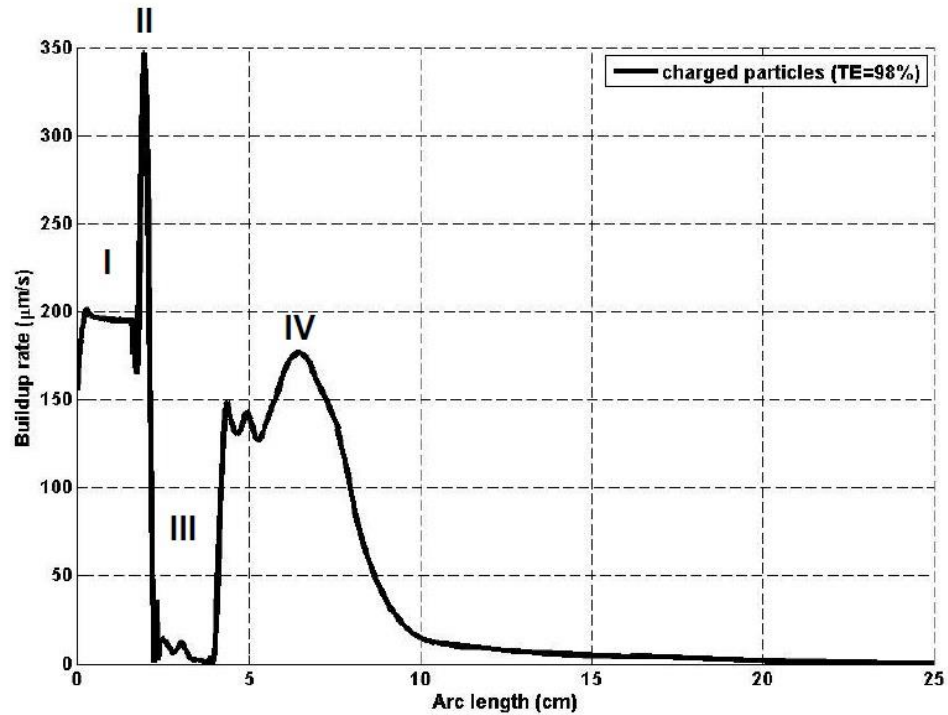
Figure 7.15: Buildup rate of polydispersed particles on a target with a protrusion of height=2 cm

As shown in Figure 7.16, when the protrusion height is reduced, the edge effect becomes less significant since the electric field value is decreased at the corner. Also, because for small protrusion heights the field value decreases on the flat top surface (Region I in Figure 7.3), the coating buildup rate is then decreased, as compared to the previous case of 2 cm height. For 0.5 cm height, the buildup rate of the deposited particles in Region I was found to be lower and a more uniform distribution of the deposited particles on the target surface in Region IV can be observed.

On the other hand, if the target plate includes an indentation at the center of the same size, it was found that the coating buildup rate at the bottom (Region I) becomes more uniform for charged particles, as compared with the case of the uncharged particles, and the deposition profile is closer to the case of a flat target. The coating layer at the bottom surface (Region I) was also found to be thicker than the layer built on the side wall of the indentation (Region II). Because most of the injected fine particles are repelled by the air vortices inside the indentation, only few larger particles are confined in this region and

have the chance to be deposited on the side wall. The depth of the indentation was found to significantly affect the number of air vortices formed. Decreasing the indentation depth makes the coating buildup rate more uniform at the bottom surface. A reduction of the shielding of the field due to minimizing the indentation depth was realized and the edge effect at the upper corner was also less significant in the deposition pattern of this configuration than the previous one.
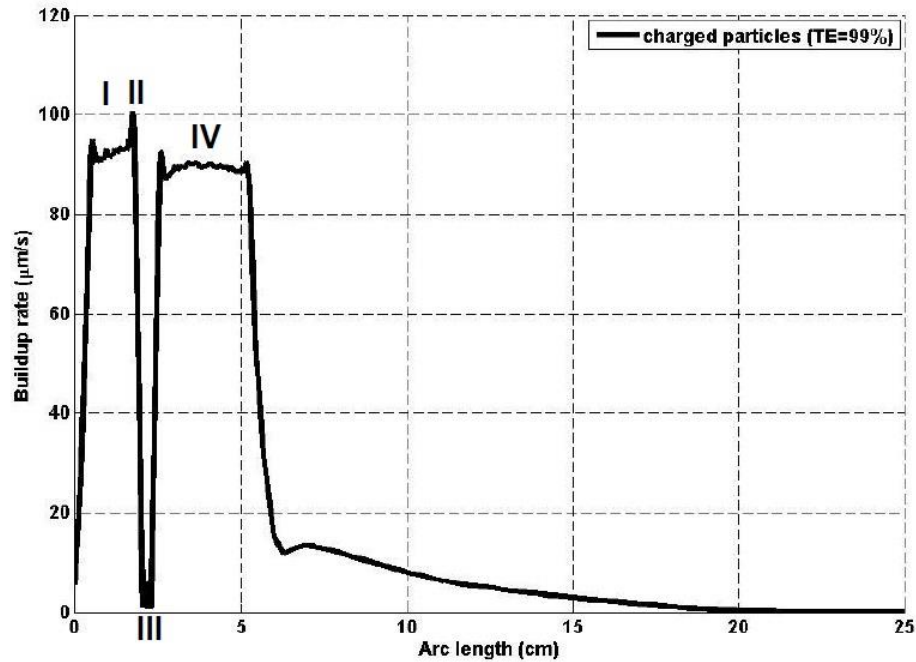
Figure 7.16: Buildup rate of charged polydispersed particles on a target with a protrusion of 0.5 cm height

7.4.4   The effect of the radius of the corner

A few cases were considered to examine the effect of the corner radius on the coating buildup rate, assuming that the radius of the upper corner of a protrusion is varied between 100 μm (the value in all the previous results), 500 μm and 1 mm. Both charged mono- and poly-dispersed particles were tested and all the results were very similar near the area of the corner. For example, Figure 7.17 shows the simulation results of the normalized coating buildup rate at the corner for 70 μm charged particles. The results confirm that there is a strong and direct relation between the degree of curvature of the corner and the particle

deposition rate as predicted from the results reported in Section 7.4.1 that confirmed the electric field increases significantly at the corners of smaller radii. This leads to an expected increase of the particle deposition at these points.

The cases for injecting polydispersed particles were also very consistent and the results show a similar trend, as in the cases of mono-sized particle injection so that the particle deposition at the corner decreases with increasing the radius of the corner.
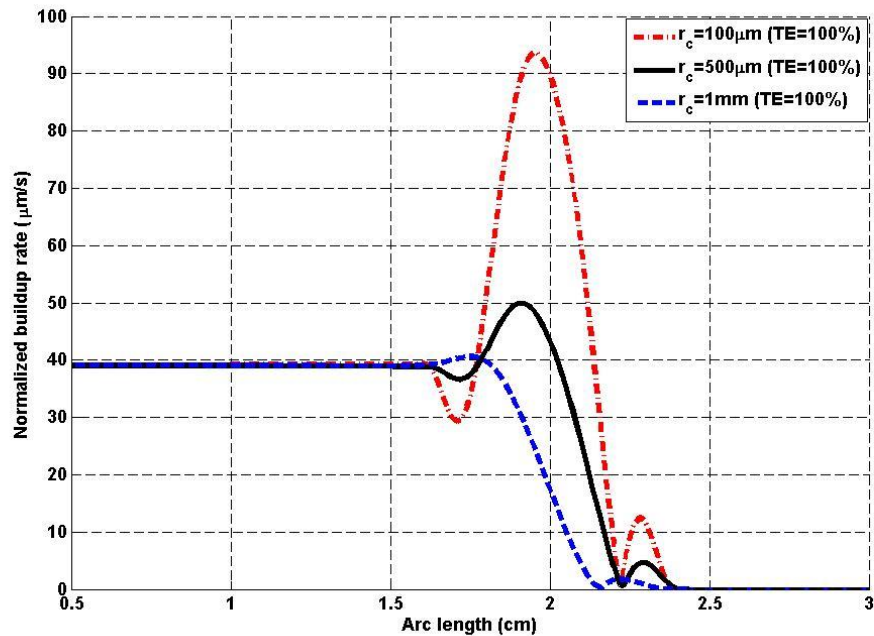
Figure 7.17: Normalized buildup rate along a target surface with a protrusion of 2 cm height at the center for different corner radii and charged particles of 70 μm diameter

7.5 Conclusions

The investigation of the electric field distribution on a perturbed surface, assuming a circular perturbation at the center, has been performed using COMSOL. The numerical results reveal that the electric field is non-uniform in the region of the perturbation. The field value is high at the corners and depends on different parameters, such as the radius of the corner, the radius and height of the protrusion or the depth of the indentation. A direct influence from these parameters on the Faraday cage effect has also been observed. Also, the simulation results show that the field values are significantly affected by the existence

of space charge in the area between the electrodes.

On the other hand, the coating buildup rate, which depends upon the electric field distribution as well as the air flow, has been examined using ANSYS, assuming an injection of different particle sizes and charge-to-mass ratios. Three surface configurations have been investigated: a flat target and a target with a protrusion or an indentation. The numerical results show a non-uniform distribution of paint for perturbed surfaces, as compared with the deposition profile of a flat surface. It was noticed that more of the smaller particles drift from the center than the larger particles. Also, it was found that the concentrations of the larger charged particles at the corner and at the flat-top surface of the protrusion, or the bottom side of the indentation, are strongly affected by the protrusion height or the indentation depth. The shielding of the field, which controls the deposition of charged particles in the shadow of the protrusion height or inside the indentation area, is affected by the radius of the perturbation and its height or depth. The edge effect can be reduced by increasing the radius of the corner, which shows a dramatic decrease in the localized buildup of the larger charged particles. This effect was also less significant in the case of the indentation and this is due to the shielding of the field due to circular symmetry. As a result, it was found that injecting particles of size 35 μm diameter achieves a good compromise between reducing the effect of streamlines of air flow and minimizing the Faraday cage penetration problem as well as the edge effect.

However, although the phenomena of the edge effect and the Faraday cage effect in the electrostatic coating process may occur separately in different geometries, they are also interrelated.

Consequently, the electric field predictions from the analysis model of the electrostatic field using COMSOL showed a very good correlation with the determination of the particle deposition patterns on different surface perturbations. This allows the geometric design of complicated surfaces to be examined for parametric variations such as the size of the perturbation and the corner radii prior to conducting a full study of the deposition pattern, a process that requires much more demanding computations.

References

[1] H. Osman, G.S.P. Castle, K. Adamiak, "Numerical study of particle deposition in electrostatic painting of a perturbed surface," J. Electrostatics, vol.77, pp.58-68, 2015.

[2] J.A. Cross, Electrostatic: Principles, Problems, and Applications, Adam-Hilger: Bristol, UK, 1987.

[3] K. Adamiak, G.S.P. Castle, I.I. Inculet, and E. Pierz, "Numerical simulation of the electric field distribution in tribo-powder coating of conducting cylindrical objects," IEEE Trans. Ind. Appl., vol.30, pp.215-221, 1994.

[4] H. Chen, B. Gatlin, G. Burnside, R.N. Reddy, V.K. Kandarpa, and M.K. Mazumder, "A transfer efficiency model for powder coating process," Proc. of the 13th IEEE/IAS Annual Meeting, Orlando, FL, vol.2, pp.1280-1283, 1995.

[5] K. Adamiak, "Numerical investigation of powder trajectories and deposition in tribocharge powder coating," IEEE Trans. Ind. Appl., vol.37, pp.1603-1609, 2001.

[6] K. Adamiak, "Numerical modeling of tribo-charge powder coating systems," J. Electrostatics, vol.40&41, pp.395-400, 1997.

[7] A.S. Biris, S. De, C.U. Yurteri, M.K. Mazumder and R.A. Sims, "Parametric study of the Faraday cage effect of chaged particles and its implications in the powder coating process," Proc. of the 37th IEEE/IAS Annual Meeting, Pittsburg, PA, vol.2, pp.995-1000, 2002.

[8] A.S. Biris, S. De, C.U. Yurteri, M.K. Mazumder and R.A. Sims, "Surface defects and corrosion in electrostatically deposited powder films," Proc. of the 37th IEEE/IAS Annual Meeting, Pittsburg, PA, vol.4, pp.2460-2465, 2002.

[9] M. Takeuchi, "Improvement of charging characteristics of coating powders in electrostatic powder coating system," J. of Phys.: Conference Series, 142, 2008.

[10] N. Toljic, K. Adamiak, G.S.P. Castle, H.H. Kuo and C.T. Fan, "A full 3D numerical model of the industrial electrostatic coating process for moving targets," J. Electrostatics, vol.71, pp.299-304, 2013.

[11] J. Domnick, A. Scheibe, Q. Ye, "The simulation of the electrostatic spray painting process with high-speed rotary bell atomizers, Part II: External charging," Part.Part.Syst.Charact., vol.23, pp.408-416, 2006.

[12] www.comsol.com

[13] ANSYS FLUENT User's guide, www.ansys.com

[14] H. Osman, O. Ghazian, K. Adamiak, G.S.P. Castle, H.-T. Fan and J. Simmer, "The charging level of a ligament-droplet system atomized in a uniform electric field," Proc. IEEE/IAS Annual Meeting, Vancouver, BC, pp.1-7, Oct. 2014 (under review to be published in IEEE Trans. Ind. Appl.).

[15] N. Toljic, K. Adamiak, G.S.P. Castle, H.H. Kuo and C.T. Fan, "A full 3D numerical model of the industrial electrostatic coating process for moving targets," J. Electrostatics, vol.71, pp.299-304, 2013.

Chapter 8

Conclusions

8.1 Summary

In this thesis three main topics have been addressed:

8.1.1 Estimation of droplet charge level

The charging level on a liquid droplet is a very important parameter that affects the spraying characteristics and needs to be determined accurately to predict the behavior of the droplet in the electrostatic coating process. The droplet liquid was assumed to be ideally conducting so the transfer of the electric charge between the bulk fluid and the droplets happens instantaneously. Therefore, a static approach was used for modeling the charge process in a ligament-droplet system. The effect of various factors on the droplet charge levels have been investigated, such as the droplet and ligament radii, the droplet shape, the presence of adjacent ligaments, the previously formed droplets, the space charge, the width and length of the electrode. A series of numerical simulations was also performed to find out which parameters affect the radius exponent of the droplet.

In addition, a comparison between the linear and circular array of ligaments was attempted for the same operating conditions. In order to have more realistic droplet and ligament shapes, the dynamics of atomization was also investigated by simulating the motion and breakup of a ligament with a free surface and imposing the effects of surface tension. COMSOL, a Finite Element commercial software, was employed for the numerical modeling of the different system configurations.

8.1.2 Numerical modeling of electrostatic coating process

The electrostatic painting system was analyzed numerically with the aid of a CFD commercial software ANSYS. This package is capable of predicting the dynamic motion of particles under the influence of different kind of forces. In this study, a 3D numerical model was created, where the air flow was simulated using the Realizable k-ε model. The computational domain and meshing parameters were carefully selected such that a high

accuracy was attained while saving computational time. The discrete phase and continuous phase were involved in the numerical modeling. It was assumed that the discrete phase consists of spherical particles dispersed and superimposed on the continuous phase. The dispersion of particles due to turbulence was predicted by stochastic tracking model. The electric force was estimated by calculating the electric field formed by the voltage applied to the bell cup and the space charge of the charged particles. This was incorporated into the ANSYS solver as a user-defined particle body force.

The injection spray pattern was modified in this model for mono- and then poly-dispersed particles in order to achieve a closer agreement with the experimental data. Many cases have been considered with a series of injection angles and different mass fractions. Also, three injection "virtual" rings with different radii were introduced at a certain distance from the atomizer's tip. It was shown that the deposition thickness at the center of the target can be increased to a reasonable level. The numerical results were validated with the experimental data. In addition, the numerical model was developed to examine the deposition pattern for a target moving in one and two directions. The simulation results showed a very good agreement with the experimental data.

8.1.3   Investigation of the deposition pattern on surface with perturbations

The correlation between the electric field and the particle deposition thickness on a target with a surface perturbation was investigated. Different target configurations, including an indentation or a protrusion at the center, were created and the simulations were performed using COMSOL to calculate the electric field in different regions along that target surface. Various model parameters were assumed to vary, such as the size of the perturbed area, the corner radius and the space charge density. In addition, the particle deposition thickness and the particle trajectories were predicted for the same model using ANSYS, where the injections of mono- and poly-dispersed charged and uncharged particles were considered. It was shown that the electric field is non-uniform in the region of perturbation and the degree of non-uniformity depends on the model parameters. Also, a very good correlation with the particle deposition pattern was obtained.

8.2 Conclusions

A number of important conclusions can be derived from the investigations of this thesis:

1. A mathematical approximation of the charge magnitude was obtained with acceptable accuracy and expressed as a function of the ligament length. It has been found that the droplet charge is a function of particle radius to some exponent, which is equal to 2 when the droplet is in direct contact with a planar electrode and decreases dramatically to 1.6 and then approaches 1.1, as the ligament length increases. The effect of the ligament diameter is also significant and the droplet charge increases with the ligament length. The effect of the adjacent ligaments on the charging level was investigated and it has been found that the charge magnitude of a spherical droplet increases monotonically, as the spacing between the ligament increases. Also, the presence of previously injected droplets reduces the charge on the surface of a new injected droplet (primary droplet), which eventually saturates at a value of 30% lower than that of a single droplet.

2. The droplet shape is formed by interaction between the surface tension and the inertial force. It was assumed that the jet is moving at a given initial speed. If the initial speed increases, a longer ligament would be expected. The Finite Element solver, COMSOL, was used to simulate the dynamic formation of the droplet-ligament system and it was found that the final shape of the droplet is a prolate ellipsoid. A comparison with the charging level of spherical droplet having the same volume showed that the predicted charging level of the spherical droplet is lower than the one of the actual shape in a range of 15-26%.

3. Direct prediction of droplet charge for different spray configurations and conditions was performed by 2D and 3D numerical models in COMSOL. It has been found that the charge magnitude for a given droplet size and electric field varies depending upon the spray geometry. It was shown that the electrode width and length are critical parameters that can affect the droplet charging level. The electrode width was tested from zero (no electrode) to 100 mm (planar electrode)

in the case of a single ligament, and for a linear and circular array of ligaments. It has been found that the droplet charge decreases with increasing the electrode width in all cases with fixed droplet and ligament radii, ligament length and spacing. Also, the effect of the electrode length was studied in the case of a linear array of ligaments and a decrease of the droplet charge was noticed with increasing the electrode width.

4. The droplet-ligament configuration (a single ligament and linear or circular arrays) was investigated and it has been found that the system configuration is another critical parameter that can affect the droplet charging level. A comparison between these configurations was made and the results revealed that the droplet charge in the case of a linear array of ligaments is about 3 times larger than the case of a single ligament and it is about 10-20 times larger than the case of a circular array.

5. The radius exponent of the droplet charge was estimated for the cases of a linear and circular array of ligaments. The effect of the electrode width on the radius exponent in the case of a linear array of ligaments was also examined and it has been found that the radius exponent value is approximately equal to 1 in the case of no electrode and increases slightly, as the electrode width increases to approach 1.14 in the case of a planar electrode. Also, the results showed a significant effect of the ligament length on the radius exponent in a system of linear array of ligaments. The exponent value was found to approach 2 in the case of no ligament (i.e. ligament length is equal zero) and decreases to approach 1.1 for the case of 4 mm length. The effect of the space charge on the radius exponent in the case of a circular array of ligaments was also investigated and was found to be insignificant with the exponent value approaching 1.6. As the ligament length increases, it was found that the radius exponent decreases and approaches 1.15.

6. The accurate prediction of an optimum injection pattern, which agrees well with the experimental spray pattern, is complicated. The reason may be due to many different factors, such as the impossibility of having a good numerical model to

simulate the actual spray injection pattern and the effect of the turbulent flow. However, different cases have been studied and presented in this thesis using ANSYS to have a reasonable agreement with the experimental results. In these cases, the injection pattern of the sprayer was modified by introducing a number of injection angles and fractions of mass flow rate. Also, three virtual injection rings with different radii were assumed in the numerical model to create a cloud of injection of charged particles. The cases of injecting polydispersed particles showed a good agreement with the experimental results. Also, it was found that the mass of the deposited particles in the cases of injecting charged polydispersed particles is larger than that in the cases of mondispersed particles. The total number of injected super-particles in the cases of polydispersed particles is 15 times larger than the injected particles in the cases of monodispersed particles.

7. The 3D numerical model was developed in ANSYS using the moving mesh capability to predict the deposition thickness profile for the cases of a moving target in one and two directions. The numerical and experimental results were in good agreement in both cases.

8. There are a number of limitations in the accuracy and visualization of numerical results, such as the exact time domain flow prediction that is needed for realistic particle trajectories calculations and the transient particle motion with a continuous particle injection. Also, the accuracy of the numerical results can be affected by parameters of the computational domain, for example, mesh size, convergence limit, number of super-particles, etc. Considerable care must be taken in the selection of appropriate values of these parameters in order to obtain satisfactory results.

9. For a flat target surface, the air flow from a rotating bell sprayer forms a conical shape as it moves towards the target. When the air hits the target surface, it spreads evenly in all directions. The maximum air velocity is at the tip of the sprayer and it gradually reduces as the axial position is increased, but the central part of the target

surface has the lowest air velocity magnitude. When the protrusion is introduced at the center, the air velocity becomes very low in the shadow of the protrusion height and air vortices can be formed. Similarly, the air velocity inside the indentation area is low and the possibility to create air vortices is high. Therefore, the air velocity distribution on a perturbed surface is non-uniform.

10. The electric field was analyzed on a flat target and a target with a small perturbation at the center in 2D axisymmetric model using COMSOL. The numerical results showed a non-uniform distribution of the electric field in the region of the perturbation. Also, it has been found that the electric field is high at the corners and depends on different model parameters, such as the corner radius, the size of the perturbation and the space charge.

11. The deposition thickness was predicted in a 2D numerical model using ANSYS for a flat target and a target with surface perturbation at the center. A direct influence of the corner radius and the size of the perturbation on the Faraday cage effect and the edge effect were observed. The injection of different particle sizes and charge-to-mass ratios was examined and it has been found that smaller particles drift from the central part of the target surface because they are very sensitive to the air drag force. The edge effect can be reduced by increasing the corner radius and the simulation results showed a dramatic decrease in the buildup rate of the larger charged particles at the corner of a protrusion, but it was less significant in the case of an indentation due to the field shielding as a result of the circular symmetry. Also, the shielding of the field, which controls the deposition of charged particles in the shadow of the protrusion height or inside the indentation area, is affected by the radius of the perturbation and its height or depth.

12. The calculated electric field distribution on a target with surface perturbation using COMSOL showed a very good correlation with the predicted particle deposition pattern from ANSYS. Therefore, complicated surfaces can be analyzed by

calculating the electric field distribution prior to conducting a full study of the deposition pattern, which requires significantly more computational time.

8.3   Recommendations for future work

There are some suggestions for future studies in the area of the numerical modeling of the electrostatic painting process:

1. The Finite Element Method was used in this research to calculate the charging level of the droplet-ligament system and it could be interesting to examine other methods of computation that can reduce time and improve accuracy (e.g. Boundary Element Method). Also, the investigation on the droplet charge level and the radius exponent is not complete and requires more experimental data for verification.

2. A future numerical study is recommended to find out more accurate prediction of an optimal injection spray pattern to be matched with the experimental deposition thickness. Also, an inspection of more model parameters is still required to have a fuller description of the atomization and injection process.

3. It is believed that the 3D numerical model of the electrostatic coating process presented in this thesis is capable to better study the effect of various parameters on specific aspects of the process (e.g. charge-to-mass ratio, particle size, etc), but meshing capabilities and visualization techniques need to be improved. Also, the measured values of the charge-to-mass ratio of individual droplets would be very useful.

4. The Faraday cage effect and the edge effect need more investigation (for example, the cases of target moving in one and two directions). The correlation between the electric field and the particle deposition pattern is recommended for a further study considering more complicated target configurations in 3D.

Appendix A

Charging of Droplets Formed from 3D Linear and Circular Array of Ligaments

This Appendix is supplementary material to the work presented in Chapter 5 and was carried out after the paper was accepted.

A.1   3D circular array of ligaments

A 3D circular array of ligaments was created using COMSOL, such that the ligament spacing, the droplet size and the space charge were assumed to vary. To enable the investigation of the effect of a circular array of adjacent ligaments on the droplet charge levels, the symmetric boundary conditions along the walls of the computational domain was applied, as shown in Figure A.1a, where two cutting planes were assumed to define the spacing between ligaments to equal 0.5 mm. The ligaments were directly connected to a 90 kV electrode of 0.5 mm width and 25 cm length, as shown in Figure A.1b. The effect of different values of the space charge density on the droplet charge levels were examined in this model, such that a uniform space charge density between the high voltage and grounded electrodes was assumed and calculated as

$$\rho = \dot{M} \times \frac{\text{distance between electrodes}}{\text{droplet velocity}} \times \frac{q}{m} \times \frac{1}{\text{Volume of computational domain}} \tag{A.1}$$

where ρ is the charge density, $\dot{M}$ is the total mass flow rate and $\frac{q}{m}$ is the charge-to-mass ratio.

Figure A.2 shows that the calculated charge-to-mass ratio decreases with increasing the droplet size. A comparison between these results and the theoretical predicted values[†] was made. When the nominal value of the space charge density, as calculated from Eq.(A.1), was equal to 20.6 nC/m³, the calculated charge-to-mass ratio and the theoretical predicted

---

[†] These values were predicted theoretically as the distribution of $q/m \propto r^{-2}$. If it is assumed that all the droplets have the same surface charge density such that the 35 μm droplet has a q/m of 1 mC/kg, the distribution of $q/m \propto r^{-1}$.

values were very close for smaller droplets. Two more values of the space charge density were also suggested, such that the first and the second values are twice and one half the nominal value, respectively.
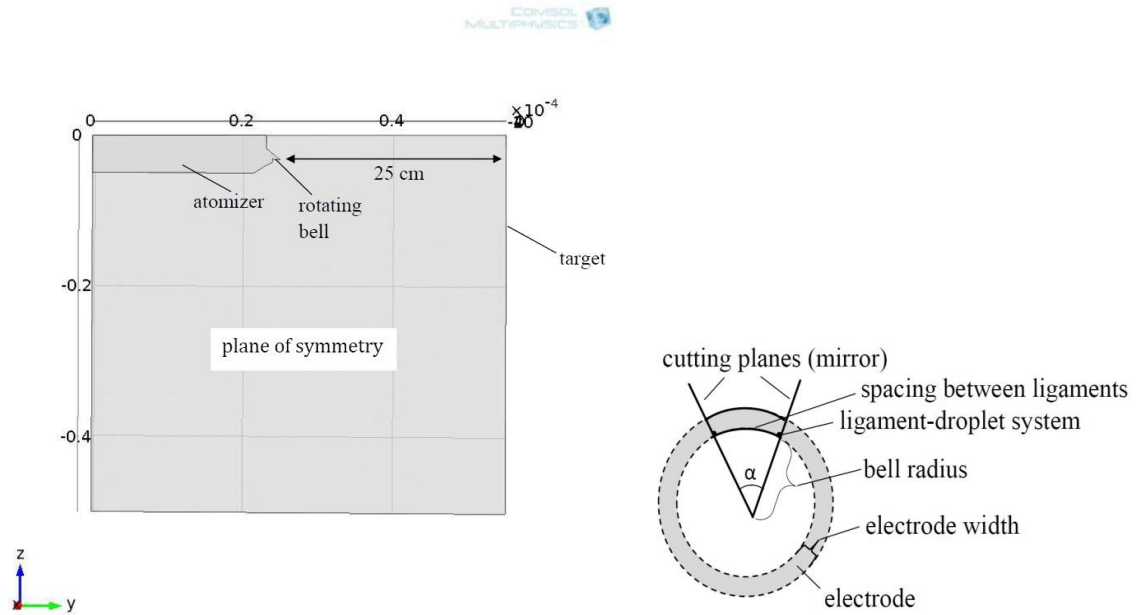
(a) Side view

(b) Top view
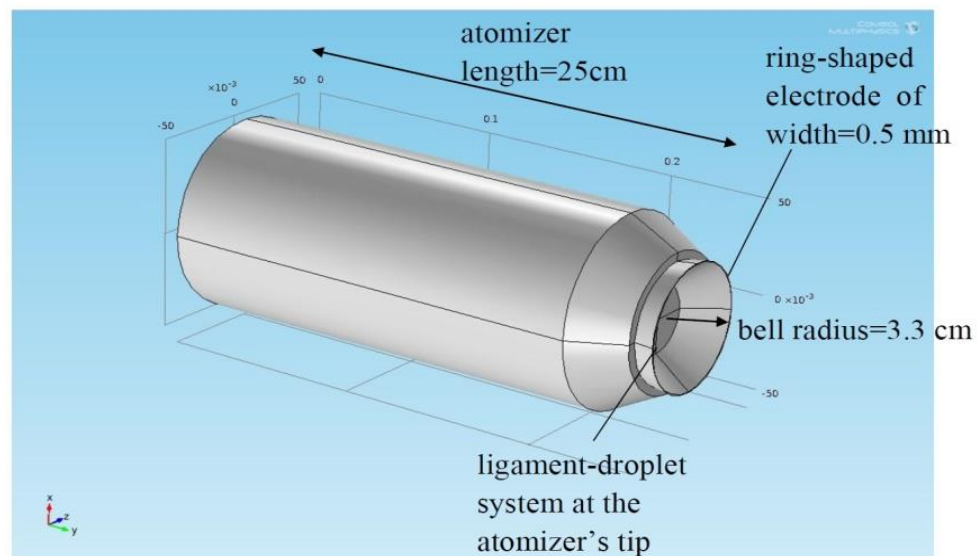
(c) 3D view

Figure A.1: 3D model of the sprayer

Figure A.2 shows that the second suggested value of the space charge reduces the difference between the calculated charge-to-mass ratio and the theoretical predicted values for larger droplets, but this difference increases with applying the first suggested value of the space charge as well as the case of no space charge.

Therefore, this study confirms that the effect of the space charge density on the droplet charge levels is very important to be considered in creating more realistic numerical model.
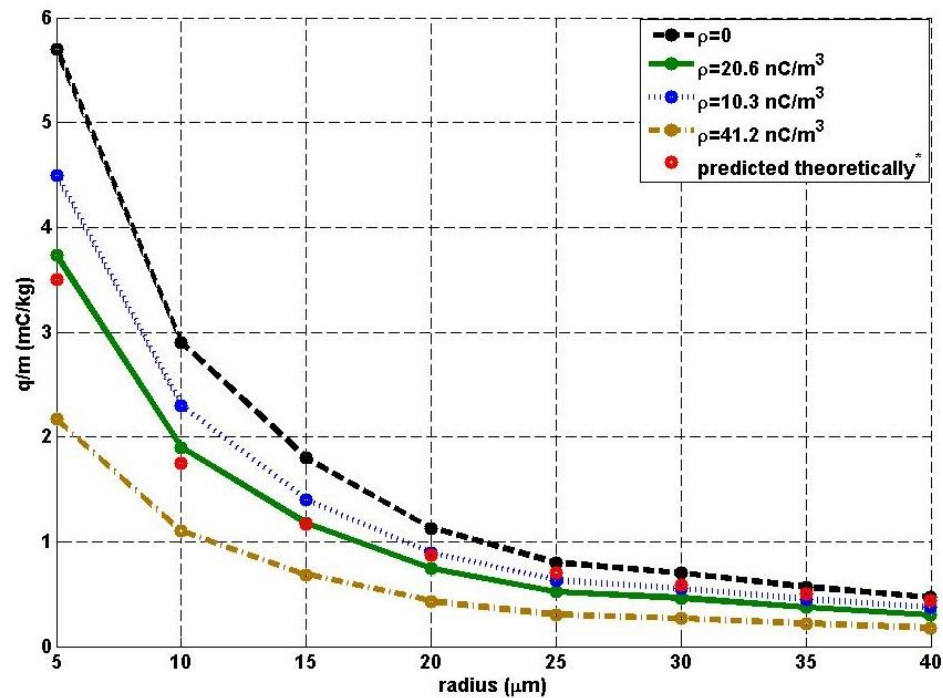
Figure A.2: Calculated charge-to-mass ratio for different values of space charge density (L=1 mm, d=0.5 mm, electrode length= 25 cm and electrode width =0.5 mm)

A.2 Comparison between linear and circular array of ligaments

The effect of the electrode length was also examined for a linear array of ligaments, such that two values of zero and 25 cm were assumed. The symmetric boundary conditions were applied to the walls of the computational domain, as shown in Figure A.3.
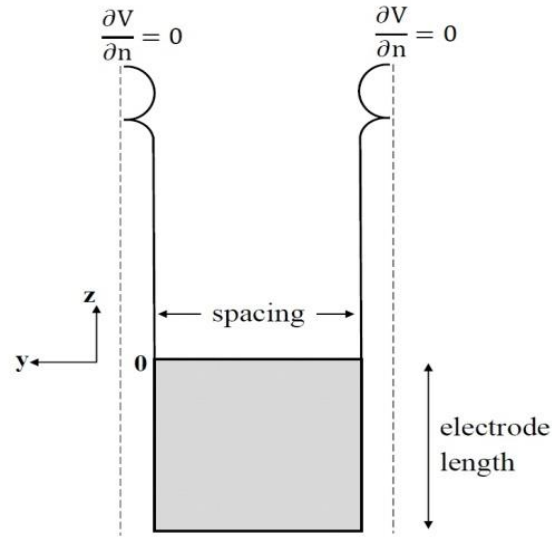
(a) Side view
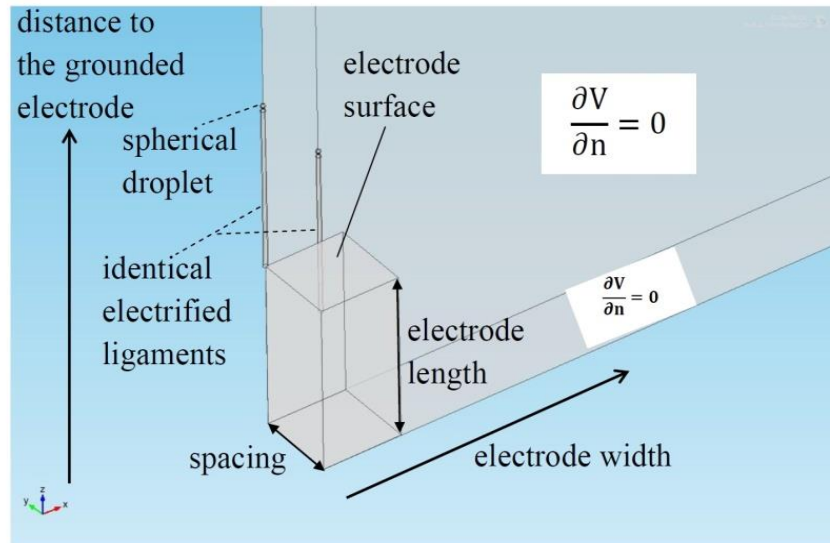
(c) 3D view

Figure A.3: 3D numerical model for different configurations and conditions of the sprayer

This simulation results reveal that the droplet charge levels decreases significantly with increasing the electrode length and the results were compared with the previous results of a circular array of ligaments, as illustrated in Table A.1. It was found that the charging level of the linear array is about 10-20 times larger than the circular array for the same model parameters.

Therefore, the simulation results of this work show that the droplet charge for a given size depends on the assumed boundary conditions, sprayer geometry (linear or circular) and width and length of the electrode.

Table A.1: Comparison between Linear and Circular Array of Ligaments
(L=1 mm, r/r_{lig}=10, d=0.5 mm and electrode width=0.5 mm)

droplet radius (μm)	calculated charge (pC)		
	linear array		circular array 25 cm electrode length
	zero electrode length	25 cm electrode length	
5	3.3	0.25	0.003
10	6.8	0.7	0.01
15	10.7	1	0.025
20	15	1.3	0.038
25	19.2	1.7	0.05
30	23.8	2.3	0.079
35	29	2.7	0.1
40	33.8	3	0.13

A.3   Estimation of radius exponent

The q-r characteristics on a logarithmic scale were obtained for a linear and circular array of ligaments. The results show a group of straight lines, where their slopes can be used to determine the radius exponent (n), as previously discussed in Chapter 4. Different electrode widths were assumed in the case of a linear array of ligaments, as shown in Figure A.4a: 100 mm (planar surface), 0.5 mm, 20 μm and 0. The results show that the radius exponent is approximately equal to 1 in the case of no electrode and increases slightly, as the electrode width increases to approach 1.14 in the case of a planar electrode.

Figure A.4b shows the estimated values of the exponent in the case of a planar electrode width at two different ligament lengths: L=0 and L=4 mm. The results reveal that the

exponent is equal to 2 in the case of a linear array of droplets for L=0 and 1.1 in the case of 4 mm ligament length.
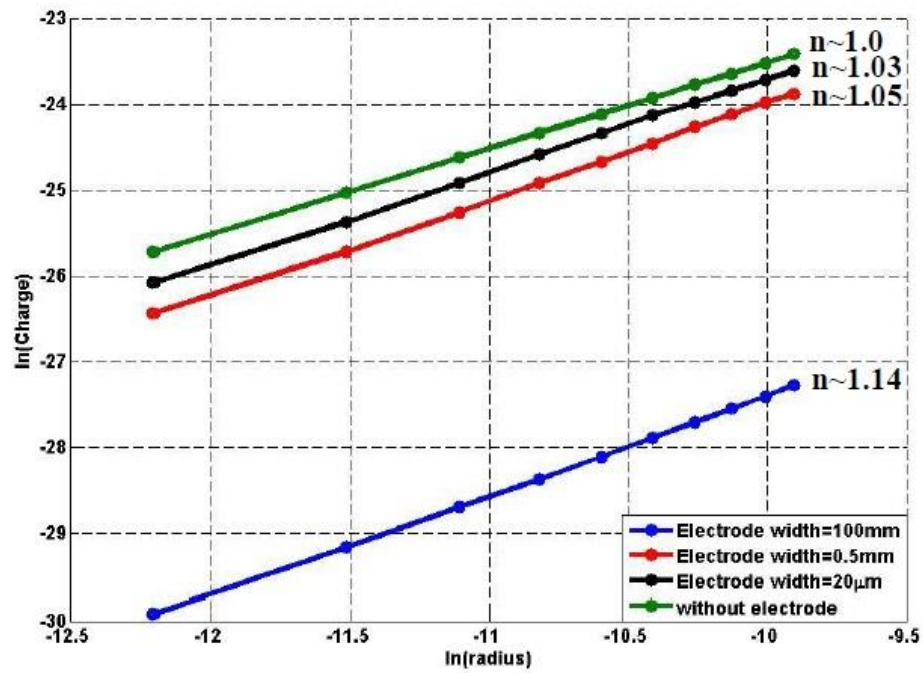
(a) Different electrode widths (L=1 mm, d=0.5 mm and r/r_{lig}=10)
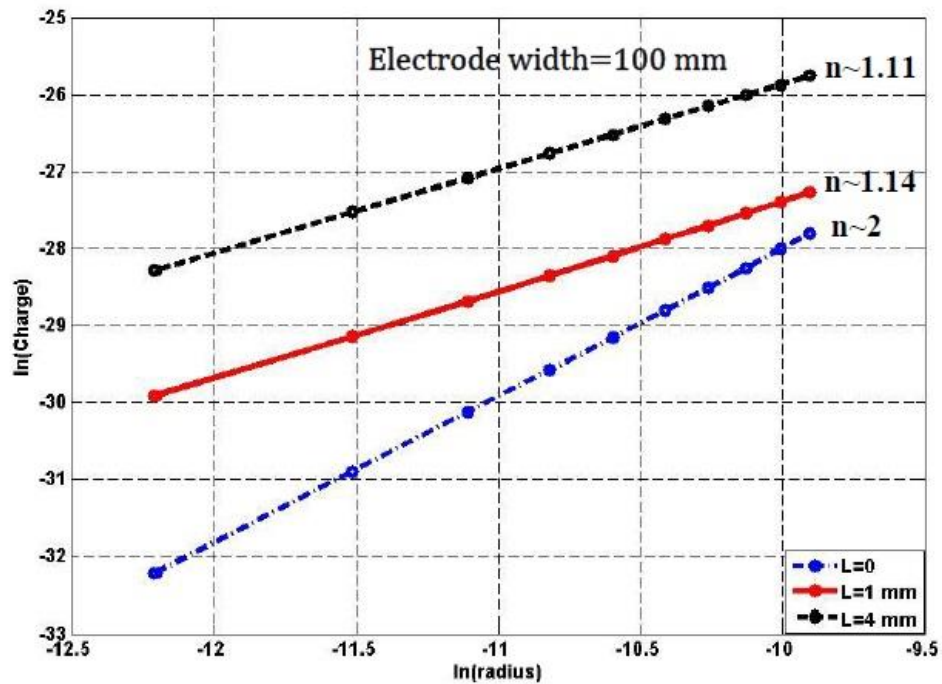
(b) Different ligament lengths (width=100 mm, d=0.5 mm and r/r_{lig}=10)

Figure A.4: The charge level versus the droplet radius in a logarithmic scale in the case of a linear array of ligaments
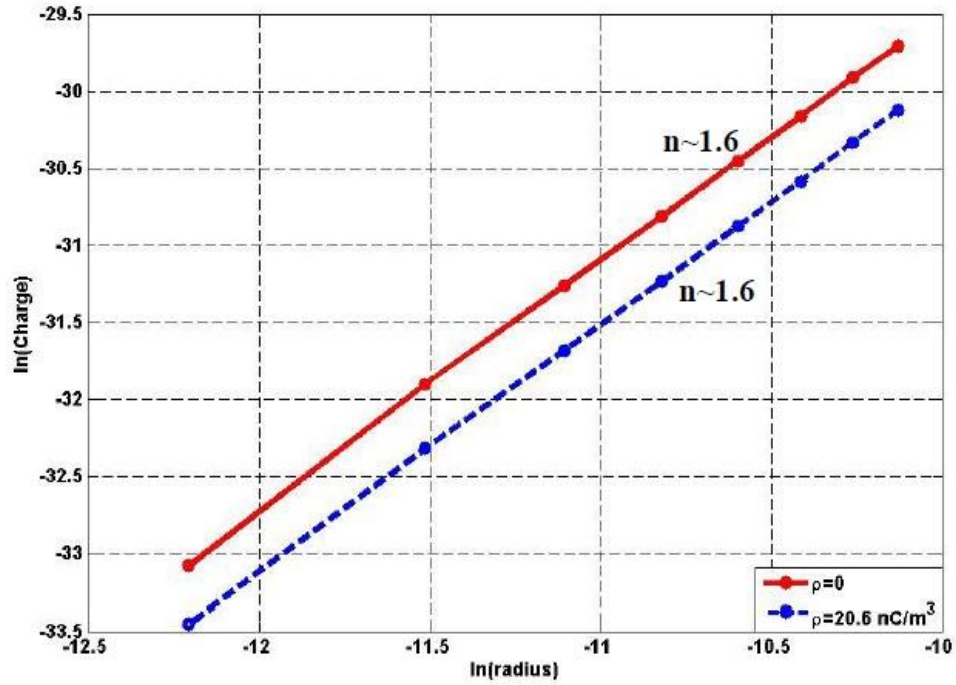
(a) With and without space charge (L=1 mm, width=0.5 mm, d=0.5 mm and r/r_{lig}=10)
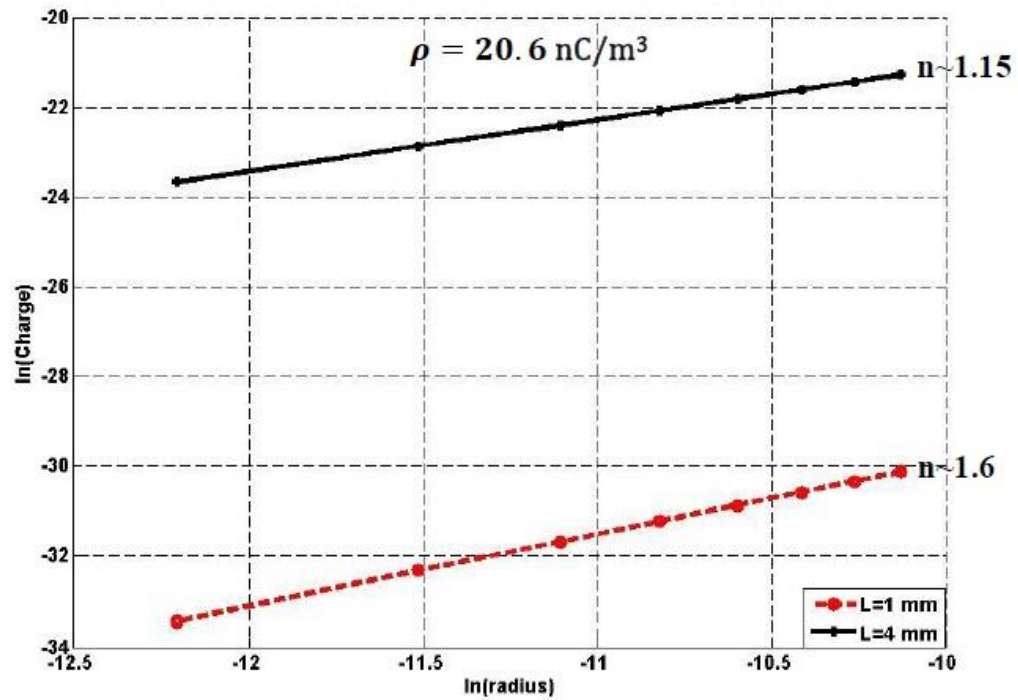
(b) Different ligament lengths (ρ=20.6 nC/m^3, width=0.5 mm, d=0.5 mm and r/r_{lig}=10)

Figure A.5: The charge level versus the droplet radius in a logarithmic scale in the case of a circular array of ligaments

On the other hand, the estimated value of n in the case of a circular array of ligaments is approximately equal to 1.6 and the effect of a space charge is insignificant, as shown in Figure A.5a. Also, the value of n was estimated for two different ligament lengths (L=1 and 4 mm), where the space charge was assumed to be 20.6 nC/m^3. The exponent is found to approach 1.15 in the case of 4 mm ligament length, as can be shown in Figure A.5b.

Appendix B

Numerical Modeling of the Electrostatic Painting Process

This Appendix provides supplementary material to the work presented in Chapter 6. The physical processes in electrostatic painting can be divided into the gas flow of the shaping air, the discrete motion of the paint droplets and the electrostatic field due to the applied voltage and charged droplets. For the mechanical spraying process, ANSYS-FLUENT software can be directly used to model the gas phase, the discrete phase and the interaction between them, thus giving the droplet trajectories. However, for electrostatic spraying, ANSYS-FLUENT does not provide a direct solution for the electrostatic field. Fortunately, the Poisson's equation for the electrostatic field can be included using a User-Defined Scalar (UDS) as an extension of the software and can be solved within ANYSY-FLUENT by incorporating it into the scalar transport equations. The coupling between the gas phase of the shaping air, the discrete phase of the paint droplets and the electrostatic field gives the trajectories of the charged paint droplets. Therefore, modeling of the electrostatic liquid spraying process can be performed completely by this software without communicating with a separate computer program to solve the Poisson field which needs a vast amount of data exchange.

B.1   Discretization and Defining the Boundary Conditions

In the numerical modeling it is necessary to define the computational domain boundaries at a certain distance away from the atomizer. If these distances are too small, they may affect the accuracy; if they are too large, a large amount of computational time may be required. Also, the mesh density has a similar effect. In order to accurately model the air flow between the atomizer and the target, the mesh density needs to be high. The mesh density away from this region can be sparser in order to minimize the computational time. Discretization of the computational domain was performed such that the problem was split into a finite number of subdomains, with relatively simple shapes. Then, a finite number of elements were constructed to fill the entire space of each domain. The mesh between the atomizer and the target is dense and almost uniform, as shown in Figure 6.2. The mesh near the boundary and at the back of the target is much sparser. Figure B.1 shows the geometry

of the computational domain with different subdomains and Table B.1 illustrates the mesh density on each domain. Also, Figure B.2 shows the geometry of the computational domain and the atomizer's tip with defined boundary conditions.
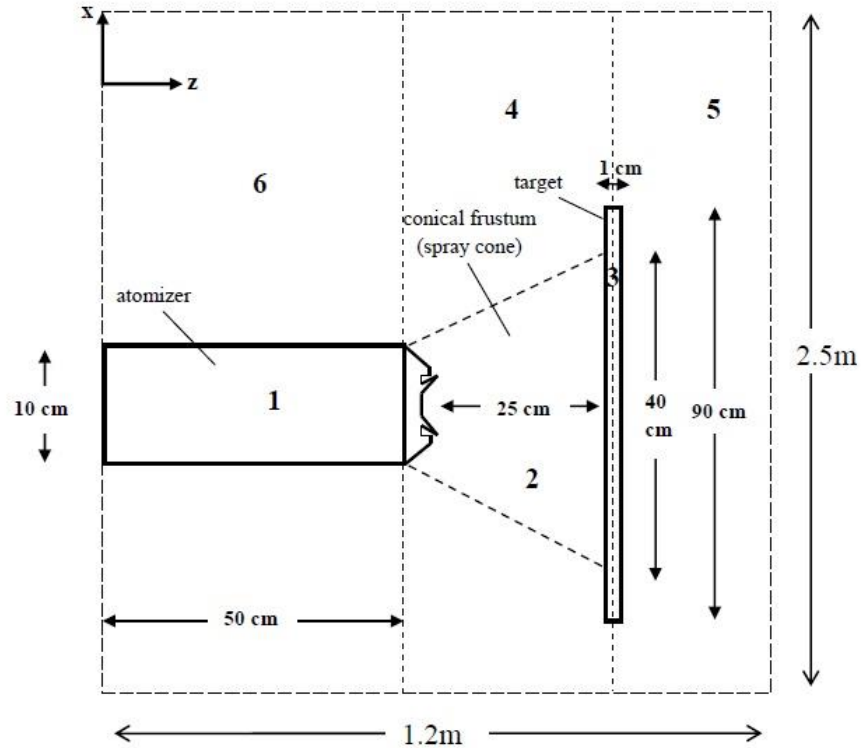
Figure B.1: Geometry of the computational domain with different subdomains

Table B.1: Mesh density on each subdomain for the case of a stationary target

Region	Mesh density
1	The surface of the atomizer has a uniform mesh interval of 1 mm.
2	The spray cone (conical frustum) has a uniform mesh interval of 0.25 mm.
3	The surface of the target has a uniform mesh interval of 0.5 mm.
4	The space between the atomizer and the target and outside the spray cone has an exponential mesh interval[†] of 3 mm on average.
5	The space between the target and the right boundary has a uniform mesh interval of 5 mm.
6	The space outside the surface of the atomizer has a uniform mesh interval of 7 mm.

[†]Mesh interval increases or decreases exponentially along the edges
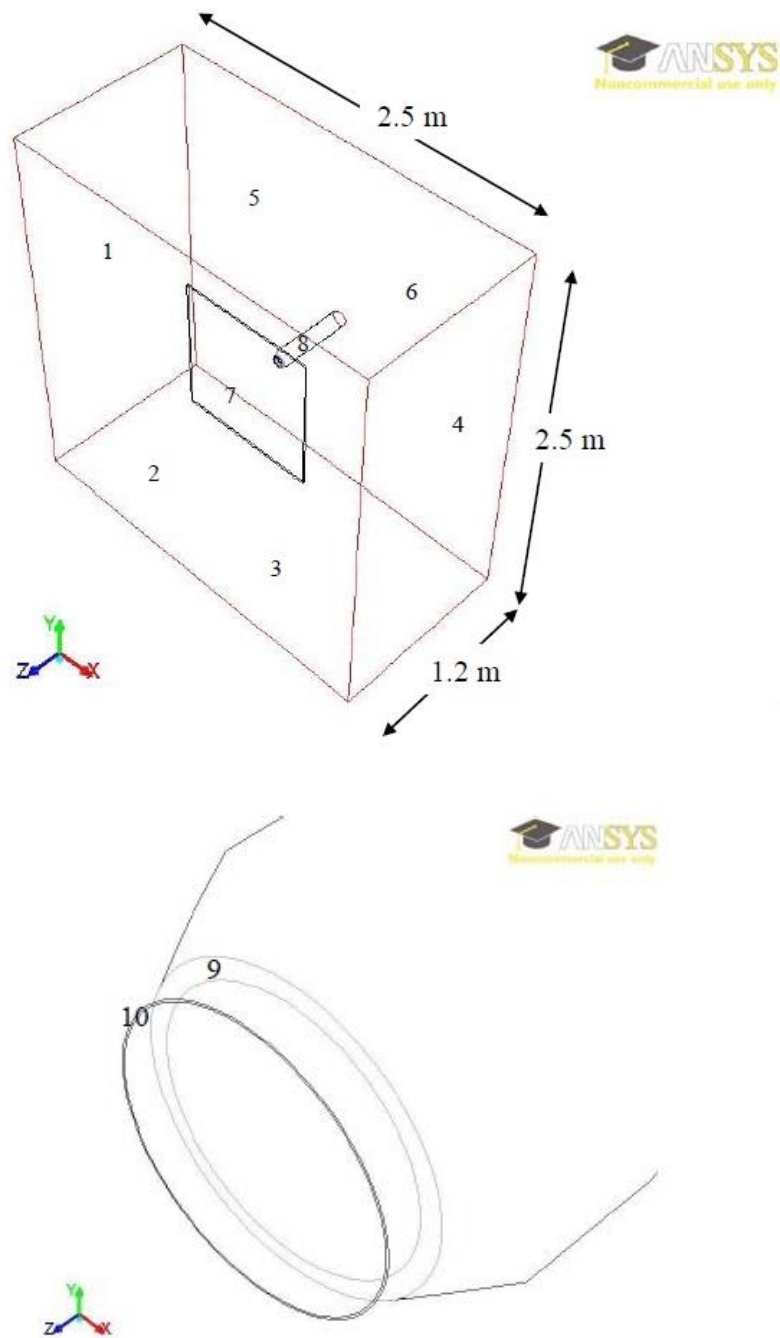
Figure B.2: Boundary conditions of the gas flow problem
(1-6: six faces of the computational domain defined as pressure outlet, 7: target surface
defined as wall, 8: body of the atomizer defined as wall, 9: shaping air defined as mass
flow inlet, and 10: particle ejection defined as wall)

The total number of cells, faces, grids, iterations and computational time for the cases of stationary and moving targets, as previously described in Chapter 6, are summarized in Table B.2.

Table B.2: Modeling data for different cases

Case		Cells	Faces	Grids	Number of iterations	Total computational time (approx.)
stationary		620,000	1,277,244	121,244	10,000	36 hrs.
moving target	strip pattern	950,000	3,112,750	200,100	30,000	170 hrs.
	zig-zag pattern	1,000,000	3,750,100	255,300	30,000	500 hrs.

B.2   Modeling of the Shaping Air Flow

The shaping air flow was considered as incompressible, steady and viscous turbulent. The Realizable k-ε turbulent model was used in the modeling. The Realizable k-ε model is a more recent development of the standard k-ε model and differs from it in that it contains a new formulation for the turbulent viscosity, as well as a new transport equation for the dissipation rate, ε, derived from an exact equation for the transport of the mean square vorticity fluctuation [1].

Coupling between the air flow and the droplet discrete phase is included via source terms of mass and momentum in order to account the influence of discrete phase on the continuous phase. Also, there is a set of semi-empirical formulas and functions that may affect the solution variables at the near-wall cells and the corresponding quantities on the wall called wall functions [1]. The standard wall functions in ANSYS-FLUENT have been widely used in industrial flows and they were provided as a default option in all numerical simulations presented in this work.

B.3   Modeling of the Droplet Trajectories

The method used for simulation the droplet discrete phase in ANSYS-FLUENT is the Discrete Phase Model (DPM) and is solved by the Lagrangian approach in which the

droplets are tracked in a frame using the random walk model in turbulent flow. The droplet trajectories are computed by solving the equations of motion of the droplets in the Lagrangian reference frame [1], as described in Eq.(3.4). The electrostatic force is calculated by calculating the electric field formed by the voltage applied to the bell cup and the space charge of the charged droplets. This term is incorporated into the ANSYS-FLUENT solver as a user-defined droplet body force and is coupled with the air flow to yield the gas flow field and the droplet trajectories, as described in Eq.(3.3). The initial conditions for the DPM model are parameters of the injected droplets including the initial position, velocity, flow rate, droplet size and distribution. Also, the number of injected droplets used in the simulation is important for the accuracy of the final results. Increasing the droplet number improves the accuracy at the same time increases dramatically the computational time and computer storage required.

B.4   Modeling of the Electric Field

The electric field generated by the voltage applied to the bell cup and the space charge formed by the charged droplets is governed by Poisson's equation (Eq.(3.11)). Then, the electric field can be determined by taking the gradient of the potential (Eq.(3.12)) and also the electric force per unit droplet mass can be obtained, as described in Eq.(3.13), as a function of the charge-to-mass ratio. For a single-phase flow and an arbitrary scalar Φ_k, ANSYS-FLUENT solves the following equation [1]:

$$\frac{\partial \rho_f \Phi_k}{\partial t} + \frac{\partial}{\partial x_i}\left(\rho_f \mathrm{u}_k \Phi_k - \Gamma_k \frac{\partial \Phi_k}{\partial x_i}\right) = S_{\Phi_k}, \quad k = 1, \dots, N \tag{B.1}$$

where Γ_k and S_{Φ_k} are the diffusion coefficient and source term for each of the N scalar equations, ρ_f is the physical density and u_k is the velocity. When in the steady state and convective flux is not to be computed, Eq.(B.1) becomes

$$-\frac{\partial}{\partial x_i}\left(\Gamma_k \frac{\partial \Phi_k}{\partial x_i}\right) = S_{\Phi_k}, \quad k = 1, \dots, N \tag{B.2}$$

Eq.(B.2) has the same form as Eq.(3.11), with Γ_k substituted by ε and S_{Φ_k} by ρ. As long as the boundary conditions are defined, Poisson's equation can be solved by ANSYS-FLUENT solver as user-defined scalar transport equations in the same computational

domain. However, some difficulties arise for the calculation of space charge density, because the sizes of the particles as well as the charge-to-mass ratios are not uniform. The position of every particle is required in the source term of the user defined scalar transport equations in order to calculate the space charge density.

B.5 Incorporation of the EHD Flow Effects

For corona charged coating, there exists one additional phenomenon called the electrohydrodynamic (EHD) air flow. When a high voltage is applied between the rotary bell and the grounded target, corona discharge takes place at the bell tip. Ions with the same polarity of the applied voltage are repelled by the electric field and drift to the grounded target. In the process, ions collide with the ambient air molecules and transfer some of their momentum to the air, forming the electrohydrodynamic (EHD) air flow. In ANSYS-FLUENT, conservation of momentum in an inertial (non-accelerating) reference frame is described by Eq.(3.3) with external body force per unit droplet mass. So, it is convenient to include the EHD air flow in ANSYS-FLUENT based on the existing model.

References

[1] ANSYS FLUENT User's guide, www.ansys.com

Curriculum Vitae

Name: Husam Eldin Ahmed Osman

Date and Place of   18 October 1978, Riyadh, Saudi Arabia
Birth:

Post-secondary   Arab Academy for Science, Technology and Maritime Transport
Education and   Alexandria, Egypt
Degrees: 1997-2002 B.Sc.

                       Arab Academy for Science, Technology and Maritime Transport
                       Cairo, Egypt
                       2002-2008 M.Sc.

                       Western University
                       London, Ontario, Canada
                       2011-2015 Ph.D.

Related Work   Teaching Assistant
Experience: Arab Academy for Science, Technology and Maritime Transport
                       2002-2011

                       Teaching and Research Assistant
                       Western University
                       2011-2015

Related Publications:

[1] H. Osman, G.S.P. Castle, K. Adamiak, C.-T. Fan, J. Simmer, "Comparison between the experimental and numerical results for the deposition thickness using full 3D numerical in electrostatic painting process," UWO internal report#10 to GM, April 10, 2013.

[2] H. Osman, G.S.P. Castle, K. Adamiak, C.-T. Fan, J. Simmer, "Charging level and deposition profile of droplets in electrostatic painting using rotary bell sprayer," UWO internal report#11 to GM, July 25, 2013.

[3] H. Osman, G.S.P. Castle, K. Adamiak, C.-T. Fan, J. Simmer, "Deposition profile for a moving target and estimate of particle charge in electrostatic painting," UWO internal report#12 to GM, November 7, 2013.

[4] H. Osman, G.S.P. Castle, K. Adamiak, C.-T. Fan, J. Simmer, "Numerical study on the charging level of a conductive ligament and the deposition profile for a moving target in electrostatic painting," UWO internal report#13 to GM, March 20, 2014.

[5] H. Osman, G.S.P. Castle, K. Adamiak, C.-T. Fan, J. Simmer, "A review on the charging level and deposition thickness of charged droplets in electrostatic painting," UWO internal report#14 to GM, July 9, 2014.

[6] H. Osman, O. Ghazian, K. Adamiak, G.S.P. Castle, H.-T. Fan and J. Simmer, "The charging level of a ligament-droplet system atomized in a uniform electric field," Proc. IEEE/IAS Annual Meeting, Vancouver, BC, pp.1-7, Oct. 2014 (under review to be published in IEEE Trans. Ind. Appl.).

[7] H. Osman, G.S.P. Castle, K. Adamiak, H.-T. Fan and J. Simmer, "Estimation of droplet charge forming out of an electrified ligament in the presence of a uniform electric field," IOP Conference on Electrostatics 2015, Southampton, UK, p.46, April 2015.

[8] H. Osman, K. Adamiak, G.S.P. Castle, H.-T. Fan and J. Simmer, "Comparison between the numerical and experimental deposition patterns for an electrostatic rotary bell sprayer," 2015 IMECE Conference, ASME, Houston, TX, USA, accepted for publication, 2015.

[9] H. Osman, G.S.P. Castle, K. Adamiak, "Numerical study of particle deposition in electrostatic painting of a perturbed surface," J. Electrostatics, accepted for publication, 2015.